In_2Se_3-based two-dimensional photocatalysts for water-splitting

Cheuk Yin (Cherie) Wong

St Edmund Hall

Supervised by Professor Shik Chi Edman Tsang

Department of Chemistry

University of Oxford

A thesis submitted for the degree of

Master of Science by Research in Inorganic Chemistry

Trinity Term 2021

Declaration

All research works reported in this thesis has not previously been accepted in substance for any degree and is not being concurrently submitted in candidature for any degree. This thesis is conducted by the author unless stated otherwise. All materials from other sources have been properly and fully acknowledged.

Cheuk Yin (Cherie) Wong

Acknowledgements

First and foremost, I would like to express my deepest gratitude to Professor Edman Tsang for providing me with the opportunity to join this research group and pursue my research under his guidance and support.

I have received valuable assistance and countless support from the following individuals: Mr Yiyang (Bruce) Li for his persisting guidance and assistance with extreme patience for every aspect of this project from day one, as well as his advice about decisions in science and life; Mr Wentian Niu for working alongside with me on the synthesis and characterisations on the early stage of the project, all the intriguing conversations and the ups and downs we went through in labs will remain one of my most treasured pieces of memory; Dr Karen Chan for her support in numerous techniques and result discussions, her company sitting next to me in the office, as well as her kindness for advising my future career and important decisions; Dr Tugce Ayvali for her support in XPS analysis; Dr Simson Wu for teaching XAS data analysis and Mr Baron Ho for his support on TEM. I am also truly thankful for Leo Leung, Haokun Wang, Tommy Sun and Will Orbell, as well as every fellow Tsang group member for not only teaching me valuable skills and knowledge but also for their companion in this mostly delightful yet challenging year.

Throughout my studies, I received immense help from research collaborators and staff. For this, I specially expressed my sincere appreciation and acknowledged the technical support I have received in the main body of the thesis.

Last but not least, this thesis is dedicated to my beloved parents and family for their endless support and encouragement. This amazing journey would not have been possible without them.

Abstract

Photocatalytic water splitting has been a burgeoning field of study due to its potential to change the world's fossil-based energy structure; however, an ideal photocatalyst has yet to be identified despite years of research. Recent research has revealed that indium selenide (In_2Se_3) carries great potential in being a promising photocatalytic water splitting catalyst due to its unique intrinsic ferroelectricity, suitability of band structure and ability to be exfoliated into two-dimensional (2D) sheets. It is a relatively less studied material and has not been explored in literature as a water splitting photocatalyst until now.

This thesis proposed to explore the photocatalytic water splitting chemistry of 2D-In_2Se_3 experimentally for the first time. In_2Se_3 was exfoliated to 2D-In_2Se_3 by the lithium intercalation method. Transmission electron microscopy (TEM) and atomic force microscopy (AFM) confirmed the thin-sheet like morphology with around 10-50 layers of In_2Se_3. Photocatalytic testing proved its water splitting activity nearly doubled after the exfoliation. In-depth characterisations were conducted to investigate its structure-activity relationship. Time-resolved photoluminescence (TRPL) revealed that the charge migration distance to the active sites was shortened, and electron paramagnetic resonance (EPR) and X-ray photoelectron spectroscopy (XPS) proved that Se vacancies were formed after exfoliation. Together, the structural changes led to improved photocatalytic activity.

An undecorated semiconductor is e to achieve a high activity due to the harsh requirements for water splitting photocatalysts. Metal doping and heterojunction formation were used as strategies to improve the activity of 2D-In_2Se_3 in this research. 5 wt.% Fe-doped 2D-In_2Se_3 (Fe-In_2Se_3) by the hydrothermal method has shown the highest activity among the screened metal dopants; Fe-In_2Se_3 has a nearly three-fold increase of activity relative to 2D-In_2Se_3. This is believed to be attributed to improved charge separation by the doped Fe^{3+} on 2D-In_2Se_3.

Two-dimensional molybdenum disulphide (2D-MoS_2) was used to form a heterojunction with 2D-In_2Se_3 due to their similar 2D structure and suitable band structure for water splitting. The successful spontaneous self-assembly construction of MoS_2/In_2Se_3 was confirmed by TEM, energy dispersive X-ray spectroscopy (EDX) and zeta potential measurements. 1:1 MoS_2/In_2Se_3 (by weight) was the optimal experimental ratio with an improved photocatalytic activity compared to the calculated average value of the two materials. The improved activity is ascribed to the formation of type-II heterojunction as proven by experimental band structure alignment (by Tauc plot and ultraviolet photoelectron spectroscopy (UPS)), which further leads to prolonged exciton lifetime as shown in TRPL analysis.

In conclusion, this thesis has investigated experimentally that 2D-In_2Se_3 exhibits water splitting photocatalytic activity and the lithium intercalation method is effective in exfoliating the material. Fe doping and MoS_2/In_2Se_3 formation were shown to be effective strategies to further boost its photocatalytic performance. Additional work is needed to further optimise this system and explore other strategies to enhance the water splitting performance of In_2Se_3-based photocatalysts.

Table of Contents

Chapter 1: Introduction

Chapter 2: Analytical techniques

Chapter 3: Experimental methods

Chapter 4: Results and discussion

List of Abbreviations

Abbreviations	Meaning
2D-In_2Se_3	Two-dimensional indium selenide
2D-MoS_2	Two-dimensional molybdenum disulphide
A	Acceptor
AEM	Adsorbate evolution mechanism
AFM	Atomic force microscopy
BP	Black phosphorus
CB	Conduction band
CBM	Conduction band minimum
CCD	Charge-coupled device
CCDC	Cambridge crystallographic data centre
CVD	Chemical vapour deposition
CW EPR	Continuous-wave electron paramagnetic resonance
D	Donor
DEER	Double electron-electron resonance
DFT	Density functional theory
DOS	Density of states
DRS	Diffuse reflectance spectroscopy
EDX	Energy-dispersive X-ray
ELS	Electrophoretic light scattering
ENDOR	Electron-nuclear double resonance spectroscopy
EPR	Electron paramagnetic resonance
ESEEM	Electron spin echo envelope modulation
ESR	Electron spin resonance
EXAFS	Extended X-ray absorption fine structure
FWHM	Full width at half maximum
GC-TCD	Gas chromatography – thermal conductivity detector
HER	Hydrogen evolution reaction
HRTEM	High resolution transmission electron microscopy
LCF	Linear combination fitting
LEF	Local electric field
LSPR	Localised surface plasmon resonance

MBE	Molecular beam epitaxy
NEXAFS	Near edge X-ray absorption fine structure
NHE	Normal hydrogen electrode
NIR	Near-infrared
NMR	Nuclear magnetic resonance
OER	Oxygen evolution reaction
PEC	Photoelectrochemical
PMT	Photomultiplier tube
PVD	Physical vapour deposition
PVP	Polyvinylpyrrolidone
QE	Quantum efficiency
RSF	Relative sensitivity factors
S	Catalyst support
SC	Semiconductor
SPR	Surface plasmon resonance
STH	Solar to hydrogen
TCSPC	Time-correlated single-photon counting
TEM	Transmission electron microscopy
TRPL	Time-resolved photoluminescence
TS	Transition state
UPS	Ultraviolet photoelectron spectroscopy
UV	Ultraviolet
VB	Valence band
VBM	Valence band maximum
XANES	X-ray absorption near-edge structure
XAS	X-ray absorption spectroscopy
XPS	X-ray photoelectron spectroscopy
XRD	X-ray diffraction

Chapter 1: Introduction

This chapter aims to provide the motivation of the project, along with an overview of the fundamentals and challenges of photocatalytic water splitting. Then, the chapter will illustrate the unique features of 2D-In_2Se_3 as a potential highly efficient water splitting photocatalyst and present the reasons to study two-dimensional In_2Se_3 (2D- In_2Se_3) as well as strategies for further enhancing the photocatalytic activity.

1.1. Motivations

1.1.1. Background of renewable energy development

Expanding renewable energy sources and reducing the dependence on fossil fuels have become a major research goal in the scientific community since the oil crisis in 1973 when there had been insecurity in worldwide energy demand[1, 2]. Countries had been stimulated to search for alternative energy technologies. Additionally, people started to realise the serious negative impacts on the environment at that time: the use of fossil fuels dramatically increases pollution and carbon emissions, which leads to long-term environmental issues. In the 21st century, the effects of climate change such as extreme weather events and global warming are already perceptible. The energy demand is also expected to grow by 1.3% each year until 2040 due to the continuous expanding population[3, 4]. Achieving net-zero (completely negating the amount of greenhouse gases produced by human activity) by 2050 is the best solution to limit the global temperature rise to 1.5 °C, which has already been pledged by countries that account for around 70% of global emissions of carbon dioxide[5].

Immense efforts have been dedicated to developing renewable energy conversion systems, which generate electricity from renewable sources such as wind energy, hydro energy, geothermal energy, solar energy and biomass energy[6]. However, fossil fuels are still the primary power source until now[7], as renewable technologies are still hindered by stringent geographical requirements[8] and exorbitant start-up costs[9]. Also, the current electrical energy

storage systems used in grid energy storage (*i.e.* batteries) are extremely costly to be deployed at a large scale[10], have limited lifetime[11] and adverse environmental impacts[12] with safety-related concerns[13]. Therefore, these renewable alternatives have not yet been able to provide a perfect solution to the energy trilemma[*] (energy security, energy equity and environmental sustainability)[14].

1.1.2. Hydrogen and photocatalytic water splitting

In light of the current situation, one of the most promising solutions is to develop a better system to store surplus renewable energy to match the demand and supply in real-time. Hydrogen has received great attraction recently to be the future generation energy carrier and energy storage option[15].

Although green hydrogen technology is still in its nascent stage, it has great potential due to several favourable features of hydrogen. First, it can be utilised directly (in combustion in automobiles or as fuel by enriching conventional fossil fuels) or used secondarily, as in fuel cells[3]. Its versatility also leads to the potential to decarbonise hard-to-abate sectors such as heating and transportation[16]. It can also act as an energy carrier in energy storage systems[17]. It has the highest gravimetric energy density of all known substances, *i.e.* about 120 MJ kg^{-1} [18]. As chemical energy, it can be stored for months and does not have the problems associated with batteries like degradation and high initial production cost. Currently, hydrogen distribution from centralised production facilities is mostly done through pipelines, which is a low-cost transmission method for delivering renewable energy[19]. Most importantly, hydrogen serves as a promising remedy for tackling the problems associated

[*] To achieve energy sustainability, one needs to balance all these factors, as sole success in any one of them comes at the expense of the other two.

with the use of fossil fuels – the only product from hydrogen combustion is water, so there are no environmental impacts from burning hydrogen.

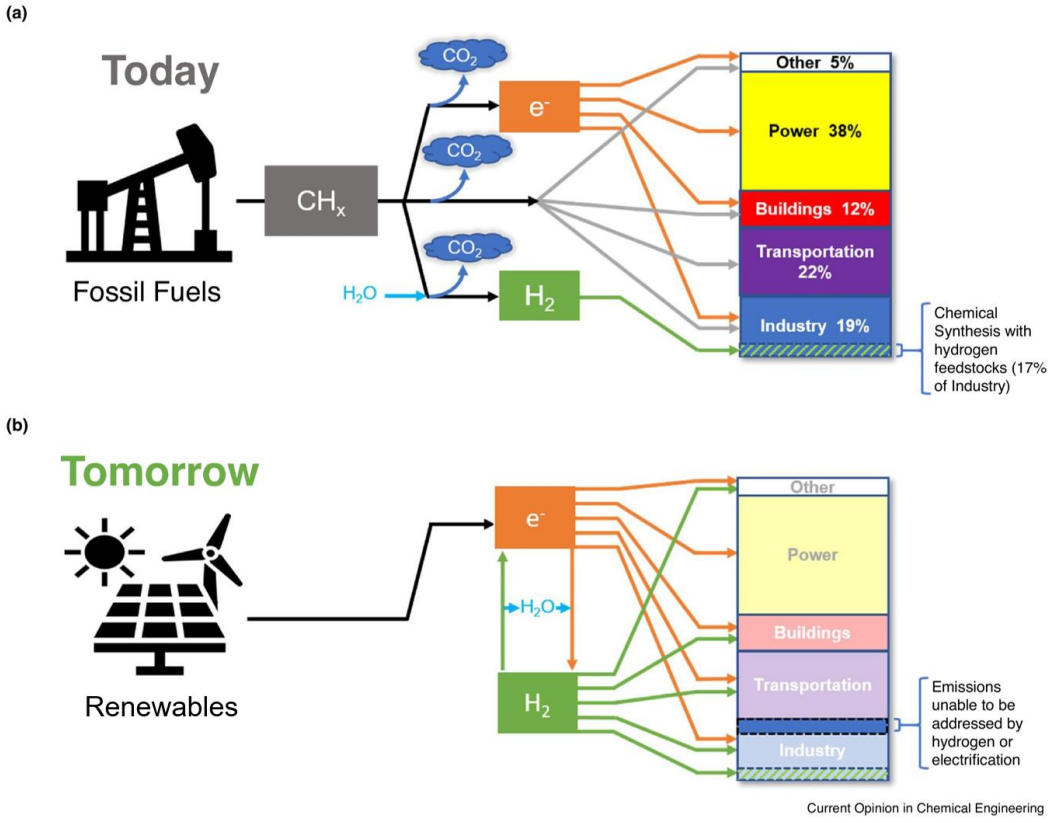

Fig. 1.1. Energy sectors (a) currently and (b) in the future. Reproduced with permission from Elsevier from reference [20].

Fig. 1.1 shows the comparison between energy sectors currently and in the future. As seen in Fig. 1.1 (a), today's energy structure is still heavily dependent on fossil fuels, which contribute to the majority of carbon dioxide emissions, especially in power and transportation. In contrast, Fig. 1.1 (b) illustrates the energy sector in the future based on a green hydrogen economy, in which hydrogen will fill a secondary role or act as an energy carrier. Electricity and hydrogen will work in parallel to power all energy-related sectors[20].

Hydrogen seems to be a fuel of the future. However, according to a report of the International Energy Agency (IEA), the current hydrogen energy production are relying primarily on

natural gas, accounting for around 75% of the annual global hydrogen production of around 70 million tonnes of hydrogen[21]. Therefore, hydrogen production is still lamentably causing a substantial amount of carbon emission.

Photocatalytic overall water splitting has emerged as one of the novel green technologies to tackle the current environmental problem in hydrogen production. The possibility of using semiconductors for photoelectrochemical (PEC) water splitting received significant attention when Fujishima and Honda published the revolutionary work in *Nature* in 1972[22]. It then marked the beginning of a sustained search for suitable semiconductors to split water efficiently by solar light. There are several unique advantages of photocatalytic water splitting. The starting material, water, and the driving force required for the reaction, solar energy, are both abundant and perpetual. Both are renewable feedstocks and have nearly no cost, so there will be virtually no fuel exhaustion[23]. Water splitting also unleashes the power of solar energy and bridges the gap between fluctuations on the supply side and reliability required by the demand side with the use of hydrogen as an energy carrier. Finally, the energy generation process is entirely carbon-free with minimal environmental impacts.

1.2. Photocatalytic water splitting

1.2.1. Definition of photocatalysis

Photocatalytic water splitting is defined as the conversion of photon energy from solar energy to hydrogen (and oxygen) in the presence of a photocatalyst and water. The word ‘photocatalyst’ is comprised of two parts: the prefix ‘photo’ means light, and a ‘catalyst’ is a material that accelerates the reaction rates but is not being consumed in a chemical reaction, and without affecting the equilibrium or thermodynamics of the reaction by the definition of Ostwald in 1895[24, 25]. Instead, a catalyst provides an alternative reaction pathway with a lower activation energy for the reaction to take place and might involve several transition

states, complexes and intermediates. As activation energy is defined as the minimum energy that is needed to be overcome for a reaction to start, lowering the activation energy barrier leads to more molecular collisions with enough energy to start the reaction, which otherwise would not be successful without a catalyst. The method of activation is the major difference between a conventional catalyst and a photocatalyst. A conventional catalyst is activated by heat, whereas a photocatalyst is driven by photons of suitable energy. Photon energy could be sourced from the freely available solar energy for photocatalysis reactions.

1.2.2. Hydrogen evolution reaction and oxygen evolution reaction

Producing green hydrogen from water is the main mission of the research project. The mechanism and the possible reaction pathways of hydrogen evolution reaction (HER) for heterogeneous catalysts will, therefore, be explained further. Additionally, oxygen evolution reaction (OER) is happening simultaneously alongside with HER in overall water splitting reaction. Therefore, it is also worthwhile to discuss the reaction mechanisms of OER.

The standard reduction potential of HER is defined as: $E^0_{H^+/H_2O} = 0\ V$ *vs.* normal hydrogen electrode (NHE) at pH 0. However, in practice, the HER is rarely initiated at the equilibrium potential. Most chemical reactions, including photocatalytic reactions, need to overcome a certain barrier or overpotential. The height of the energy barrier is largely determined by the nature of the interface on which reactions occur. For an ideal catalyst, it should have a small overpotential.

Until now, it is still challenging to understand the exact operating mechanism on different photocatalysts of water splitting. However, the HER reaction pathways under acidic conditions are widely believed to be generalised into three elementary reaction steps, which are depicted in Fig. 1.2. They are strongly catalyst-dependent and/or potential-dependent[26].

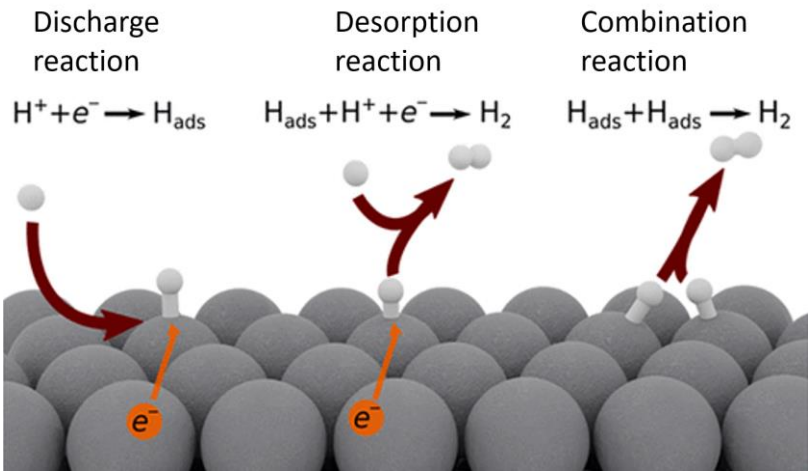

Fig. 1.2. Three elementary reaction steps involved in HER. Adapted from reference [27] with permission from ACS. Further permission related to the figure should be directed to ACS.

The first step is proton-coupled electron transfer at the catalyst surface, which yields an adsorbed hydrogen atom. This is known as discharge reaction or Volmer reaction (Eq. 1.1).

$$H^+_{(aq)} + e^- \rightarrow H_{ads} \qquad (1.1)$$

The adsorbed hydrogen could react with another proton from the solution with an electron transfer to form molecular hydrogen by Eq. 1.2. This step is known as desorption reaction or Heyrovsky reaction.

$$H_{ads} + H^+_{(aq)} + e^- \rightarrow H_2 \qquad (1.2)$$

Another possibility for the adsorbed hydrogen is to combine with another adsorbed hydrogen on the catalyst to form molecular hydrogen by Eq. 1.3. This is known as recombination reaction or Tafel reaction.

$$H_{ads} + H_{ads} \rightarrow H_2 \qquad (1.3)$$

Even though hydrogen (or proton) adsorption and desorption are two successive steps in HER water splitting reaction, they are competitive in nature[26]. When the bonding strength

between a catalyst surface and hydrogen atoms is too weak, it cannot efficiently adsorb the reactants to initiate the HER. In contrary, when a catalyst bonds too strongly with hydrogen atoms, the adsorbed hydrogen atoms would be difficult to leave the surface, thus blocking the surface-active sites. This is also referred to as self-poisoning. Therefore, an ideal photocatalyst for HER in water splitting should neither have too strong nor too weak binding energy between the catalyst and the hydrogen atoms. This is in line with the century-old Sabatier principle, which stated the optimal catalysis occurs when interactions between catalyst and substrate are of intermediary strength[28]. In other words, when Gibbs free energy of hydrogen adsorption (ΔG_H) is near zero, the binding energy of hydrogen atoms is just right to easily adsorb and desorb as hydrogen gas, promoting a high HER activity. Thus, ΔG_H is a useful descriptor in selecting a photocatalyst with potentially high HER activity[27].

Alike the mechanism of HER, the mechanism of the multi-stepped oxygen evolution reaction (OER) has not yet been fully understood[29, 30]. The transformation of H_2O to O_2 in an acidic medium is involved with intermediate oxygen species such as HO*, O*, and HOO* [†]. In the reaction, the S-O (S is denoted as the catalyst support and is usually positively charged in OER) bonding interaction has an important role in stabilising the reaction intermediates on the surface and is believed to have a pronounced effect on the water splitting efficiency[31].

The following Langmuir-Hinshelwood type adsorbate evolution mechanism (AEM), with two adjacent active sites on the catalyst, is one of the well-recognised reaction paths proposed for OER. The reaction mechanisms are expressed as Eq. 1.4 to Eq. 1.6 [32].

[†] * is denoted as the catalyst support.

$$* + H_2O \rightarrow HO^* + H^+ + e^- \qquad (1.4)$$

$$HO^* + OH^- \rightarrow O^* + H_2O + e^- \qquad (1.5)$$

$$2O^* \rightarrow O_2 \qquad (1.6)$$

Alternatively, O* formed in Eq. 1.5 can interact with a water molecule to form HOO* (Eq. 1.7). The HOO* produced is further combined with another water molecule for the subsequent OER reaction (Eq. 1.8).

$$O^* + H_2O \rightarrow HOO^* + H^+ + e^- \qquad (1.7)$$

$$HOO^* + H_2O \rightarrow O_2 + H^+ + e^- \qquad (1.8)$$

In most cases, different reaction routes will be favoured by different photocatalysts to minimise the free energy of activation. The overpotential of the OER reaction could be avoided by stabilising the intermediates such as HOO* and HO* on the catalyst surface[32]. Similar to HER, an ideal photocatalyst for OER in water splitting should neither have too strong nor too weak binding energy between the catalyst and the oxygen atoms according to Sabatier principle. The Gibbs free energy of oxygen adsorption (ΔG_O) could be a useful descriptor in predicting a photocatalyst's OER activity: ΔG_O is ideally close to zero in order to promote high OER efficiency.

1.2.3. Principles of photocatalytic water splitting

Thermodynamically, the overall water splitting reaction is an energetically uphill, endothermic reaction (Eq. 1.9)[33]. The standard Gibbs free energy change (ΔG_0) of water splitting is +237 kJ mol^{-1}. Energy is needed to drive the thermodynamically uphill reaction, and this is provided by light, or ideally solar energy, in a photocatalytic system.

$$H_2O \rightarrow H_2 + \frac{1}{2}O_2 \qquad \Delta G_0 = +237\ kJmol^{-1} \qquad (1.9)$$

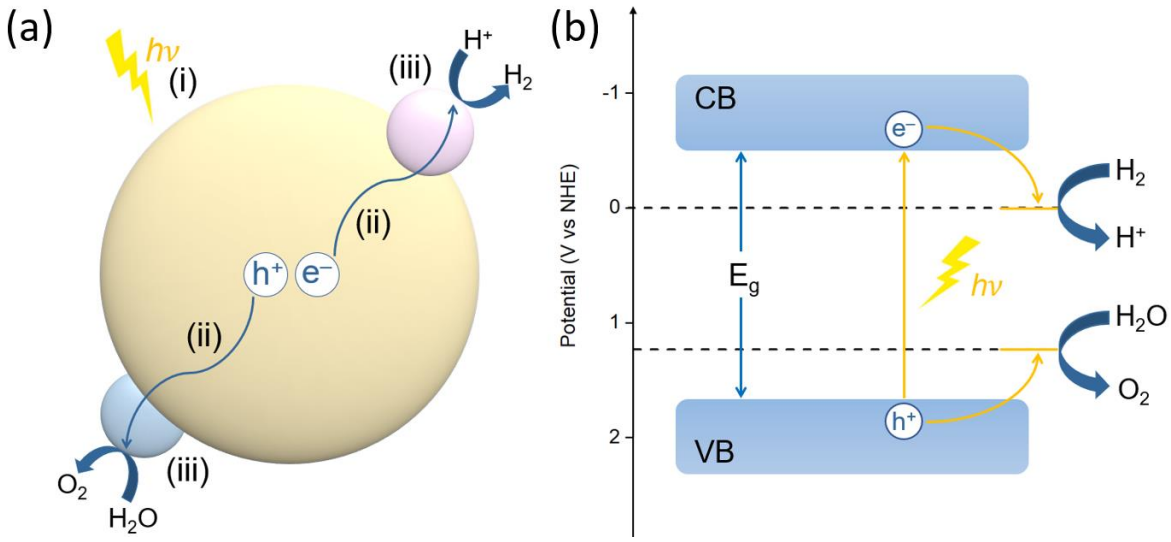

Fig. 1.3. (a) Schematic representation of the mechanism of water splitting over a semiconductor photocatalyst particle. (b) The energy diagram of photocatalytic water splitting based on one-step excitation[34]. Based on reference [34] with permission from ACS.

Fig. 1.3 (a) presents a schematic representation of a typical semiconductor particle loaded with a surface hydrogen evolution cocatalyst and an oxygen evolution cocatalyst for overall water splitting. The photocatalytic water splitting comprises three fundamental steps: (i) the absorption of photons, which have energy larger than the semiconductor bandgap to excite electrons from the valence band (VB) to the conduction band (CB). This process will create electron-hole pairs (or excitons). (ii) Then, the photoexcited charge carriers are separated and subsequently migrate to the surface-active sites. (iii) Finally, the surface redox reactions are initiated by the electrons and holes to generate hydrogen and oxygen, respectively, with the assistance of the cocatalyst in some systems which will be further explained in section *1.3.5.2*. It should be emphasised that the primary role of the semiconductor in photocatalysis is to absorb an incident photon, generate an electron-hole pair and facilitate its charge separation and transportation, while the catalysis of the reaction is an additional function that can be performed by different materials such as cocatalysts[35].

The migration or travelling of the reactants and products proceed in a mass diffusion manner concurrently[36]. As a detrimental factor of the mechanism, recombination of photoexcited carriers occurs along with these reactions. Therefore, the charge separation and the reactions on the surface must proceed within the lifetimes of photoexcited carriers in a complete water splitting reaction. These concepts hindering the activities will be further explained in section *1.2.5*.

The typical concerted four-electron process in an acidic aqueous solution for water splitting is shown in Eq. (1.10) to Eq. (1.12) [37].

Overall water splitting reaction: $2H_2O \rightarrow 2H_2 + O_2$ (1.10)

Hydrogen evolution reaction (HER): $4e^- + 4H^+ \rightarrow 2H_2$ (1.11)

Oxygen evolution reaction (OER): $2H_2O \rightarrow 4H^+ + O_2 + 4e^-$ (1.12)

The tendency of the adsorbed species (adsorbed hydrogen and water) to accept/donate electrons manifests itself in its reduction/oxidation potential, respectively. By thermodynamics, the ability of a semiconductor to transfer photogenerated charge carriers to adsorbed molecules is governed by the alignment of the conduction and valence band edges of the semiconductor with the redox potentials of the charge carriers in most cases[38, 39]. Therefore, the reaction conditions (*i.e.* the photocatalysts) are generally depicted in terms of the position of the band edges in literature.

As illustrated in Fig. 1.3 (b), protons (H^+) are reduced by electrons in the CB to generate H_2 while O_2 is produced by water oxidation by holes in the VB. To achieve the overall water splitting, the potential of the conduction band minimum (CBM) must be more negative than the H^+/H_2 reduction potential (0 V *vs.* NHE at pH 0). This is because the scale of the redox potential goes from positive to negative with increasing energy, and chemical reactions are

only favourable when they are going from a more negative potential end to a more positive potential end (Fig. 1.4). Analogously, the valence band maximum (VBM) must be more positive than the O_2/H_2O oxidation potential (+ 1.23 V *vs.* NHE pH 0). As a result, the minimum theoretical bandgap energy of overall water splitting is 1.23 eV. It does not matter if the energy of the photons (*i.e.* solar energy) is higher than the bandgap energy. As long as the electrons are excited to the conduction band, they can relax in a fs timescale to lower states in the CB or intraband trap states before reaching the surface of the photocatalyst. It means they never provide a higher reduction potential than the CBM [35, 40].

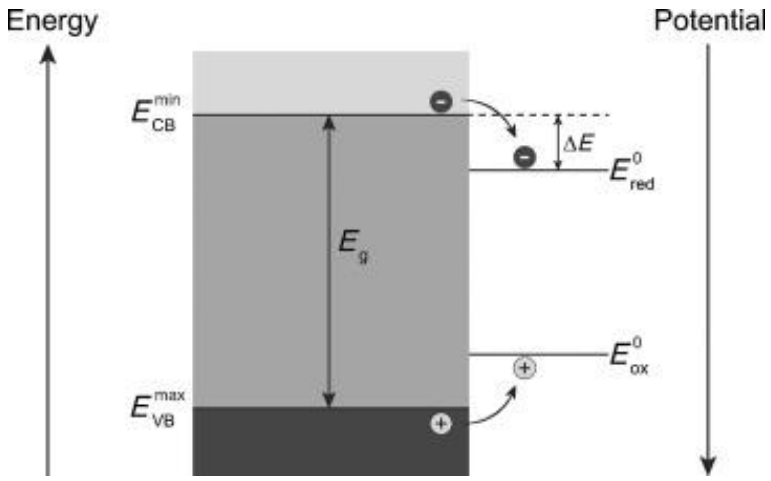

Fig. 1.4. Thermodynamic constraints on the transfer of electrons and holes to the reduction and oxidation potential, respectively. ΔE represents the kinetic overpotential of the reduction process. Reproduced with permission from John Wiley and Sons from reference [35].

The mentioned considerations are the thermodynamic considerations which imply the choice of a photocatalyst needs to be a compromise between two competing factors. On one side, for achieving higher efficiency, it is beneficial to have a smaller bandgap so more solar energy is absorbed and utilised. On the other hand, the band structure of the photocatalyst

needs to have spanned the range of the reduction and oxidation potential of water, or have a suitable band alignment with the two potentials.

To further complicate the situation, it is, in fact, crucial to provide an overpotential for the redox process from a kinetic point of view. The range of potentials should not only be just matched but there should be a substantial margin (ΔE) on each side between the VBM and CBM with the O_2/H_2O oxidation potential and H^+/H_2 reduction potential, respectively (Fig. 1.4). Without an overpotential, even a good catalyst that matches the bandgap energy and band position cannot drive the reaction at reasonable rates[41]. The reaction might still be able to proceed, but it will rely on the Brownian motion of electrons, which is presumably much slower than having the potential difference as the reaction driving force[35]. According to this consideration, the bandgap should be as wide as possible. Some extra energy is also needed to overcome the activation barrier of the reaction like charge transfer at the interface, polarisation, and surface adsorption[42, 43]. As a result, the bandgap of the light absorber is usually required to be >1.6 eV for a practical reaction to proceed at a reasonable rate[44, 45].

1.2.4. Key parameters for photocatalytic activity evaluation

There are several parameters for evaluating a photocatalyst's water splitting performance. These include hydrogen evolution rate, quantum efficiency (QE) and solar to hydrogen (STH) conversion efficiency. Even though QE and STH are comparable between publications for different heterogeneous photocatalysts, QE and STH are only meaningful when the photocatalytic conditions are optimised (*e.g.* the optimised photocatalyst amount and cocatalyst loading)[46]. This research project has not yet achieved the point of optimising the photocatalytic system, therefore, hydrogen evolution rate is used as the main parameter for evaluating a material's water splitting photocatalytic performance.

The hydrogen evolution rate (μmol h^{-1} $g_{catalysts}^{-1}$) is calculated by Eq. 1.13.

$$H_2\ evolution\ rate = \frac{n(H_2)}{t \times m} \qquad (1.13)$$

where $n(H_2)$ is the number of moles of hydrogen generated in the water splitting reaction, t is the reaction time when it reaches the reaction temperature and m is the mass of photocatalysts. An example of the hydrogen evolution rate calculation is shown in the *Appendix*.

1.2.5. Current challenges in photocatalytic water splitting

A recent life cycle study suggested that a minimum threshold of 10% solar-to-hydrogen (STH) efficiency is needed for the industrialisation of photocatalytic water splitting[47]. Nevertheless, decades after the pioneering work from Fujishima and Honda, the photocatalytic water splitting STH efficiency has not reached the industrial benchmark of 10% experimentally until now. The field is still stuck at the embryonic stage of laboratory investigation, with rare pilot plant-studied cases. The current photocatalyst systems still suffer from various challenges, each of which will be elaborated further in the following section.

1.2.5.1. Charge recombination

As mentioned in section *1.2.3*, when a photon with enough energy strikes the semiconductor, an electron is excited from VB to CB, leaving a hole in the VB. A hole is considered a positive charge species and has a strong tendency to attract electrons from the neighbouring atoms. As a result, a hole of one atom might interact with an electron of another atom, or even the excited electron might fall back into the same hole. The merging of the free electron and a hole is called charge recombination. As the excited electrons are relaxed during recombination, energy will be emitted from the electron-hole system in the form of photons

or phonons (lattice vibration). Direct bandgap semiconductors undergo radiative or non-radiative recombination, in which the former dominates (*i.e.* photons are emitted in the process)[48].

The separation and recombination of photoexcited charge carriers are competitive processes in photocatalysis. Any strategies that can prolong the charge lifetimes of charge separation or suppress the recombination time would be beneficial in constructing a highly efficient photocatalytic system.

The recombination process is happening continuously, but the incoming energy keeps forming new electron-hole (or exciton) pairs until it reaches an equilibrium. The average timing between the creation and the disappearance of an electron-hole is termed exciton lifetime. The lifetime varies upon the semiconductor's material, crystal structure, size, and shape.

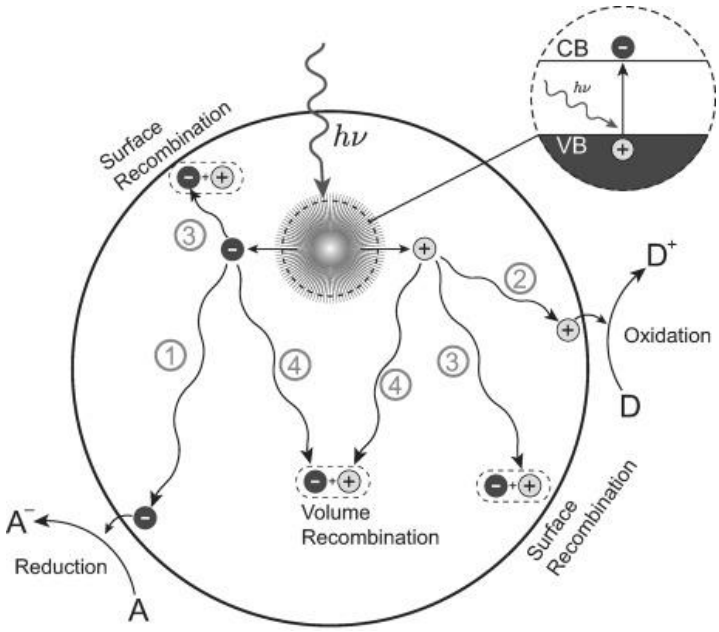

Fig. 1.5. Photoexcitation of electron-hole pair in a semiconductor with possible decay paths including recombination paths and desired reactions. A is denoted as the electron acceptor

and D is the electron donor. Reproduced with permission from John Wiley and Sons from reference [35].

The trapped electrons and holes can either recombine on the surface or in the bulk of the semiconductor, which is also referred to as volume recombination (Fig. 1.5)[35]. Generally, the recombination of photoexcited charges occurs at ps to μs timescale, while the surface water splitting reaction takes place at a longer timescale at μs to s[33]. Therefore, in many cases, recombination is the dominating reaction that photoexcited carriers undergo, because the electron-hole recombination is more kinetically facile. Various factors determine the recombination rate, such as mobility and trapping of charge carriers, the defect density in the semiconductor or the presence of an interface with a secondary material that acts as an electron or a hole sink[35]. Strategies for boosting the surface reaction or suppressing the recombination are advantageous for improving the performance of a photocatalytic water splitting system.

1.2.5.2. Slow charge transfer

The timescale of charge separation and surface catalysis reactions are synergistically correlated[33]. It can be understood as there being only a certain number of active sites on the surface of the photocatalysts and interfacial diffusion (or migration) of reactant (H_2O) and products (H_2 and O_2) are needed to diffuse between the solid-liquid interface into or away before and after the reaction. The diffusional transports and surface reaction is at the timescale of ms to μs[49-51], while the photon transmission and photoexcitation is in the timescale of ps to ns and fs to ms, respectively[52-54]. It shows that the consumption (diffusional transport and surface reaction) of the charged species is much slower than their generation; the surface of the photocatalysts will be congested and blocked with photogenerated species and triggering undesirable charge recombination as there is no other

option for the usually short-lived and reactive charge carriers to react. As a result, charge diffusion from the bulk to the surface-active sites as well as the surface water splitting reaction are mostly the limiting processes in water splitting. Any material design could shorten the diffusional transports so that the surface reaction is preferred, thus promoting photocatalytic activity.

1.2.5.3. Low energy yield and mismatch of band alignment

As mentioned, the VBM and CBM must satisfy the potential of OER and HER for water splitting. Since the minimum photon energy is 1.23 eV (equivalent to a photon with wavelength ~1000 nm), solar photons with a wavelength larger than 1000 nm are not suitable for the reaction. It means a certain amount of solar energy is never going to be able to be utilised in water splitting due to the redox potential limitations and the unmatched photon energy with the bandgap of the photocatalysts. The wasted energy will be dissipated as heat or cause a fluorescence effect. Therefore, designing a photocatalyst with lower bandgap energy is crucial to absorb a larger range of solar energy in the spectrum. However, it will induce a high rate of charge recombination due to the lower overpotentials available for the catalytic half reactions.

Worse still, there are multiple transmission and conversion barriers that impose energy losses. Solar light is made up of a series of the radiation spectrum, containing 5% UV light (<400 nm), 43% visible (400-700 nm) and 52% near-infra-red light (700-2500 nm)[55]. Before reaching the Earth's surface, a large portion of solar radiation is absorbed, scattered, or reflected by humidity and carbon dioxide in the atmosphere, and is wasted for the photocatalytic reaction. Furthermore, before reaching the bulk of photocatalysts to charge separate, solar photons have to transmit through several mediums, such as the reactor, water (as a suspension medium and as a reactant), and the surface of the photocatalysts (as the

electron-hole photoexcitation is happening in the bulk). A large amount of light energy will be absorbed, reflected, and scattered by the medium and will greatly decrease the final transmitted light from reaching the photocatalyst.

Under the theoretical conditions where the efficiency of the light absorbance, carrier separation, as well as quantum efficiencies, are all 100% (ideal but impractical until now), the maximal theoretical efficiency can reach 47% due to the limitation of 1.23 eV redox potential. By taking additional considerations of heat losses and other energy losses factors, the maximum STH efficiency that a photocatalytic water splitting system can achieve is only a mere 18%[56, 57].

Yet, all recent results are still under-performing the theoretical maximum as well as the industrialisation threshold STH (10%). From the literature, possibly the best discovered STH efficiency till now was 5%, which is achieved on a cobalt(II) oxide (CoO) photocatalyst without any cocatalysts or sacrificial reagents[58]. However, further work is needed to support its stability as well as its photocatalytic conditions. Therefore, to date, the highest reported efficiency of any system is still only half of the required efficiencies for practical applications.

1.2.5.4. The incompetence of utilising sacrificial reagents

Photocatalytic water splitting is immensely difficult in a pure water system because water molecules are highly thermodynamically stable and resist dissociation. Overall water splitting is assumed to be a complicated stepwise four-electrons process as limited by OER from Eq. 1.12 [59, 60]. Therefore, a pure water splitting system is highly ineffective. It is often claimed that the incorporation of sacrificial reagents can solve the issue by serving as charge scavengers (h^+ scavenger or e^- donor). A nucleophilic (electron donor) sacrificial reagent is needed to scavenge electrophilic (electron acceptor) photogenerated h^+, while preserving

photogenerated e^- for H_2O reduction to H_2 to prevent charge recombination[61]. Furthermore, O_2 is not produced from the hole scavenger action of sacrificial reagents, since the back reaction to produce water is suppressed. Therefore, the H_2 yield is increased and a subsequent gas separation stage can be avoided. Almost all studies demonstrated increased H_2 generation when sacrificial reagents are incorporated[62]. Most of the investigated sacrificial reagents are organic compounds, such as methanol[63-65], ethanol[66-68], isopropanol[69, 70] and butanol[71, 72] which have all been demonstrated as hole scavengers in previous studies. Combining these organic compounds as electron donors can irreversibly fill in the photogenerated VB holes and can enhance the electron-hole separation efficiency, resulting in higher QE[61, 62].

Unfortunately, using sacrificial reagents in a photocatalytic water splitting system is not ideal. First, these electron donors are continuously consumed in the reaction to provide sustained H_2 production, which is not economical. Apart from the economic aspect, measuring HER in a sacrificial system no longer generates any mechanistic information. For example, it is difficult to determine whether the electron transfer from the CB or the reducing organic radicals is rate-limiting, or whether the QE is limited by initial hole transfer to the sacrificial reagent. Furthermore, H_2 enhancing mechanisms might be due to the dissociation of sacrificial reagents, particularly when the organic sacrificial reagents are H-bearing. This means the scavenging effect toward enhanced H_2 photogeneration without considering photoconversion of organic sacrificial reagents is simply incorrect, especially under the photoconversion conditions[73, 74]. These organic compounds are far less thermodynamically stable than pure water, thus more likely to be photocatalysed to H_2 or other small molecules such as CO_2, CO and CH_4. For example, ΔG_f^0 of CH_4 formation is -228.6 kJ mol^{-1} while the ΔG_f^0 of H_2 formation is 0 kJ mol^{-1}. It shows that the photocatalytic formation of CH_4 is more

thermodynamically viable than the formation of H_2[74]. The photocatalytic mineralisation of organic-type sacrificial reagents can be confirmed by the post-reaction analysis of the liquid phase (residual concentration of sacrificial reagent) and gaseous products (presence of CO_2, CO and CH_4) to confirm the photo-reforming or decomposition of organic sacrificial reagents under photocatalytic water splitting conditions[62]. Finally, the potential to generate secondary pollution from irretrievable sacrificial reagents would associate with high-cost waste management, which contradicts the original aim of generating green H_2.

Although the STH might be lower with the absence of sacrificial reagent, using sacrificial reagent is not a long-term, genuine solution for improving the efficiency of water splitting. Therefore, further discussion will mainly focus upon the water splitting system without the use of sacrificial reagent, where water is the only required reactant and with the help of photocatalyst and solar energy to produce hydrogen.

1.2.5.5. Other related challenges

There are other challenges apart from the aforementioned ones. For a photocatalyst that could be potentially used industrially, it must have excellent physicochemical stability to retain the catalytic activity in the timescale of years. Even though most semiconductors are chemically stable in an aqueous environment, oxidative and/or reductive photo-corrosion processes are often encountered under light irradiation[41]. Therefore, the choice of suitable materials with excellent long-term stability is crucial to support rapid charge migration and surface reactions.

Also, photocatalytic water splitting suffers from a backward reaction, which reverts H_2 and O_2 to H_2O. From a thermodynamic point of view, the formation of water from H_2 and O_2 has a negative Gibbs free energy (ΔG_f = -237 kJ mol^{-1}), which means the reaction is spontaneous. Microscopically, the dissociation of H_2 and O_2 are adjacent to each other on

the surface of photocatalysts. When H_2 and O_2 undergo a slow desorption process, it increases the chance for them to reunite as water.

1.3. Two-dimensional indium selenide (2D-In_2Se_3)

2D-M_2X_3 (M = Al, Ga, In; X = S, Se, Te) (Fig. 1.6) has recently demonstrated outstanding visible light response-ability and electronic structure tunability in numerous theoretical studies[75-77]. Together, they show the potential of 2D-M_2X_3 as water splitting photocatalysts. Among 2D-M_2X_3, indium selenide (In_2Se_3), a relatively less reported 2D material, has been recognised as an intriguing material for solar energy conversion. It is reported that it has excellent stability, suitable bandgap position (suitable H^+/H_2 reduction potential and O_2/H_2O oxidation potential) and bandgap energy (>1.23 eV), high carrier mobility and exceptionally high absorption of visible light[78, 79]. To further understand the excellent potential of 2D-In_2Se_3, its structure is firstly addressed in this section, then its unique intrinsic ferroelectricity and its advantages to potentially be an ultra-thin 2D material are explained. Furthermore, the motives of (i) reacting under elevated temperature, (ii) metal doping and (iii) heterojunction formation as strategies for tackling the mentioned challenges to further enhance the photocatalytic activity will be discussed. Related development of these strategies will be also mentioned alongside for the readers to learn the recent progress in the field.

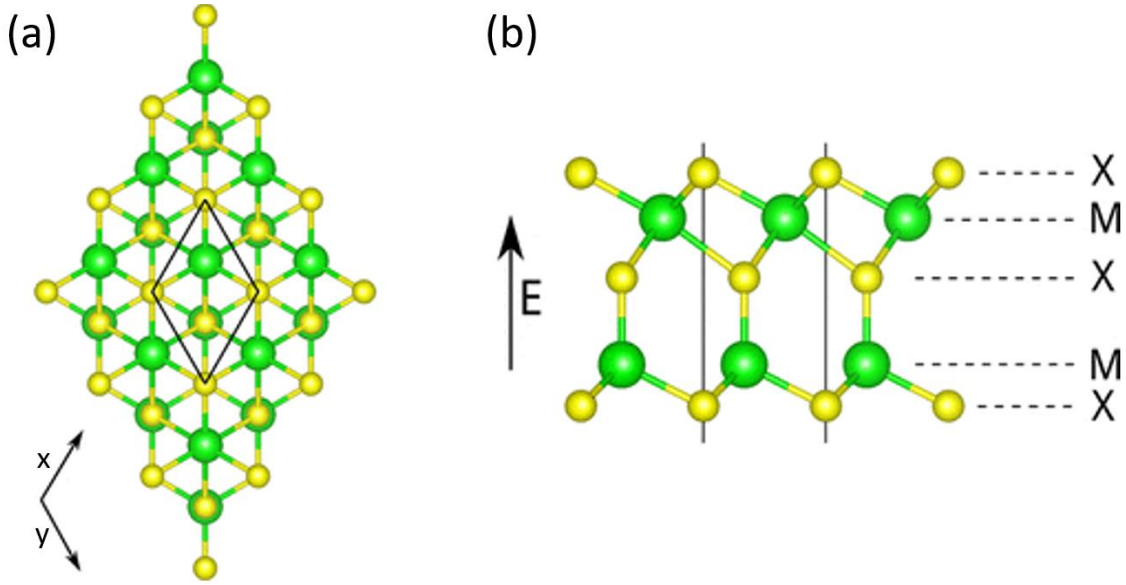

Fig. 1.6. Atomic structure of 2D-M_2X_3 (M = Al, Ga, In; X = S, Se, Te) from (a) top and (b) side views. The unit cell is drawn with black solid lines. The black arrow, E, in (b) indicates the direction of the vertical electric field. The atomic arrangement of monolayer 2D-M_2X_3 from side views is shown in (b). Adapted from reference [75] with permission from ACS.

1.3.1. Structure of In_2Se_3

The crystal structure of In_2Se_3 has been categorised into five phases: α, β, γ, δ and κ, depending on the temperature and material preparation conditions[80]. Among the phases, only α- and β-In_2Se_3 (Fig. 1.7) have semiconducting layered structure bonded to each other via van der Waals interactions, like graphene and MoS_2. The α-In_2Se_3 (space group: R3m) is stable at room temperature while the β-In_2Se_3 (space group: $R\bar{3}m$) is stable at 523 K[81]. The two phases have different stacking arrangements between layers, but they are composed of the same monolayer structure with five atomic planes. Atoms in a monolayer plane are arranged in the Se-In-Se-In-Se set with strong covalent bonds in a direction virtually perpendicular to the layer plane. From Fig. 1.8, it can be seen that the top (and bottom) layer can be viewed as having a silicene-like structure while the middle Se layer can be considered as having an octahedral structure, or 'T-phase' structure[82].

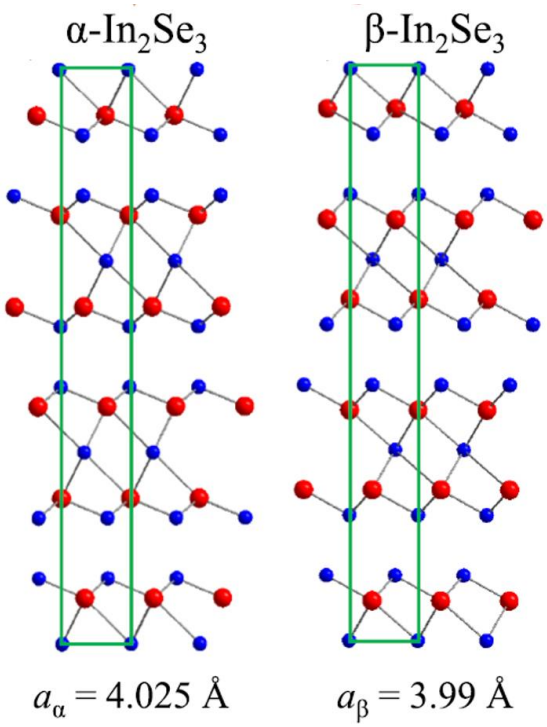

Fig. 1.7. The crystal lattice and the unit cell of α- and β-In_2Se_3. Reproduced from the open-access figure with permission of IOP from reference [83].

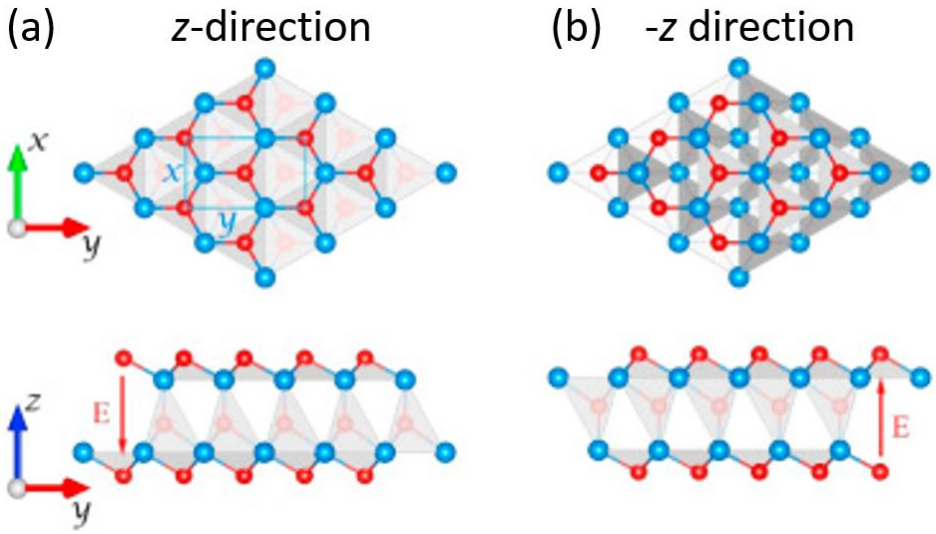

Fig. 1.8. Top and side views of In_2Se_3 monolayer from the (a) z- and (b) -z-direction. The red arrow, E, represents the direction of the intrinsic electric field. The blue atoms represent In atoms; the red atoms represent Se atoms. Adapted from reference [82] with permission from Elsevier.

1.3.2. Unique properties of In_2Se_3

It is reported that 2D-In_2Se_3 has intrinsic ferroelectricity, the presence of spontaneous electric polarisation. This can be explained by the middle position of the Se atom being shifted off from the centre from the quintuple layer such that it breaks the centro-symmetry, as seen from Fig. 1.8. The broken structural symmetry of the In_2Se_3 layer leads to intrinsic electronic polarisation, which results in an out-of-plane intrinsic electric field from the top surface to the bottom surface. This unique property has been proven by theoretical calculation and experimental work[84]. In the work of Fu *et al.*, they demonstrated In_2Se_3 features out-of-plane ferroelectricity by first-principles calculations. The intrinsic spontaneous polarisation will generate an internal driving force for the spatial separation of photoexcited electrons and holes[82]. This is hugely beneficial in suppressing the charge recombination process and therefore does positive work in photocatalytic water splitting. They even provided theoretical proof that monolayer In_2Se_3 has a theoretical >10% STH efficiency in water splitting, indicating its potential to be a highly efficient potential photocatalyst[75]. In another independent work of Zhao *et al.*, they demonstrated In_2Se_3 has suitable band edge positions and is a polarised semiconductor that is favourable for reducing the carrier recombination. By density functional theory (DFT), they further provide evidence that the partial charge density of CBM and VBM are at different faces in an In_2Se_3 layer and prove that In_2Se_3 exhibits intrinsic ferroelectricity. It further implies that the material promotes spatial distribution of charge carriers and restrains the combination of photogenerated carriers. Furthermore, they have calculated the carrier mobility of In_2Se_3 as the results show there is a mobility disparity between photo-generated electrons and holes, which further encourages the separation of carriers. The carrier mobility results are higher than some of the 2D transition metal dichalcogenides which implies the outstanding properties of 2D-In_2Se_3[82]. These reports demonstrate the unique potential of 2D-In_2Se_3 to be

a highly efficient water splitting photocatalyst, especially since the intrinsic ferroelectricity is able to suppress charge recombination and the suitable band edge positions hugely benefit the photocatalytic performance.

1.3.3. 2D materials

Two-dimensional, ultrathin In_2Se_3 is studied in this research instead of Bulk-In_2Se_3. This is due to the favourable properties of 2D materials which have attracted intense research interest for application in photocatalytic water splitting since the experimental discovery of graphene[85]. It has been investigated that a change of thickness of the material will induce an effect in photocatalytic activity. A lot of the studied 2D materials are semiconductors that exhibit diverse and tuneable electronic and optical properties and can be used as photocatalysts. These layered materials include metal oxides, MXenes, g-C_3N_4, and transition metal chalcogenides[86].

There are numerous advantages that 2D materials possess for efficient photocatalytic water splitting. First, 2D materials have an ultra-high surface-to-volume ratio, which provides a large number of active sites available for adsorbing reactant molecules (*i.e.* water) to undergo photocatalytic reactions[87]. Furthermore, the average distance which a charge carrier can migrate before reaching the solid-water interface (or termed as the diffusion length) is minimal for 2D materials. This short distance between the bulk and surface leads to the charges having a much higher probability to migrate to the surface (interface between water and photocatalysts) in a quicker manner without bulk recombination. Therefore, 2D materials have a good ability to suppress charge recombination and often demonstrate excellent photocatalytic activities. It is expected that 2D-In_2Se_3 will exhibit these advantages to have an exceptional photocatalytic water splitting activity.

It is also widely agreed that the optical and electronic properties are strongly dependent on the thickness of 2D semiconductors. Studies on MoS_2 and CdSe show that the optical bandgap widens as the thickness, or the size of the quantum dots decreases due to the quantum confinement effect[88-90]. This is not a unique feature for these two 2D materials, as it is also reported that In_2Se_3 exhibits this behaviour. The bandgap energy of α-In_2Se_3 is shown to be thickness-dependent by the report published by Quereda *et al.*[91]. They measured the optical absorption spectra of exfoliated α-In_2Se_3 crystals and observed a strong thickness-dependent shift of the bandgap energy from 1.45 eV in 25.1 nm to 2.80 eV in 3.1 nm flakes. They claimed the bandgap variation is because of quantum confinement and is among the largest reported in 2D semiconductor materials to date. Furthermore, they used DFT calculations combined with many-body techniques to estimate the bandgap of the materials with various thicknesses. The calculations reproduced the experimental results of the strong thickness-dependent optical bandgap of 2D-In_2Se_3. Other reports have also reported that In_2Se_3 has a narrow bandgap of 1.36-2.00 eV and is thickness-dependent[92, 93]. Therefore, the thickness-dependent bandgap energy of 2D-In_2Se_3 shows the band structure can be tuned by changing the thickness of the material. Furthermore, even though the bandgap energy of In_2Se_3 is not conclusive in the literature, it is fortunate that the bandgap energy range fits perfectly with the requirement of photocatalytic water splitting and can absorb a majority of solar light.

Additionally, it is reported that when reducing the dimension of material from 3D to 2D, the introduction of intrinsic defects into the 2D structure will play an increasingly important role in determining the properties of materials[94]. Defect sites such as interstitial atoms, vacancies, and grain boundaries often lead to the recombination process. Therefore, eliminating crystal defects is thought to be an effective route to improve photocatalytic activity. For example, Jung *et al.* reported that increasing the calcination temperature can lead to more crystallinity

and the reduction of the internal defects in titania particles, which is responsible for the recombination of photogenerated exciton pairs[95]. This subsequently implies that reducing the defects might achieve a higher photoactivity. In stark contrast, some also proved the opposite statement that defects can effectively trap charge carriers. In the work of Yamakata *et al.*, defect-rich $SrTiO_3$ exhibited an exciton lifetime of 1 ms, compared to the defect-free single-crystalline $SrTiO_3$ that has a lifetime of only 50 ns[96]; they explained that most of the charge carriers are trapped in the defects which are responsible for prolonging electrons' lifetime and enhanced photocatalytic activity. The two examples show introducing defects might cause promotional or detrimental effects on photocatalysis and it usually depends on the reactivity of trapped charge and its trapping depth. Qian *et al.* has provided a summary of this trend: in a general case, deeply trapped charges possess lower reactivity compared to shallowly trapped charge generally as deep traps have an energy level located at the middle region of bandgap and are pronounced charge-recombination sites, especially when the lifetime of holes is similar to that of electron[97]. However, till now, it is challenging to predict the depth of traps or control it experimentally. Numerous trial-and-error experiments are needed to carry out manually to obtain the desired trap depth and material properties[74].

To conclude, 2D materials are still a relatively new class of materials that might lead to the unexpected discovery of novel chemicals that could be useful in various applications. Recent advances in the field of nanomaterials allow precise modification of 2D materials' shapes and dimensions. For instance, some 2D materials can be cleaved or exfoliated from bulk crystals to change their electronic structure to investigate the relationship between their morphology and their photocatalytic activity. Notable examples include MoS_2[98] and black phosphorus (BP)[99]. Several 2D materials, such as WS_2[100], MoS_2[101] and ZnSe[102] have already been identified as suitable candidates for water splitting. However, the shortcomings of these materials are also becoming more apparent. For instance, their weak coulomb screening

results in large exciton binding energies, inhibiting the separation of photogenerated carriers and further lead to robust charge recombination. More importantly, these materials do not possess high light absorption efficiency. Therefore, the search for novel 2D materials for highly efficient photocatalytic water splitting is still ongoing. As mentioned, In_2Se_3 carries great potential in water splitting: it is a 2D material and is predicted to exhibit many advantages; it has suitable bandgap energy and band structure for photocatalytic water splitting as well as its intrinsic ferroelectricity for supressing charge recombination. It will, thus, be explored as a water splitting photocatalyst in this project; the motives and unique aspects of this research of 2D-In_2Se_3 is further explained in the next section.

1.3.4. Motivations for exploring 2D-In_2Se_3 in this research

Considering the unique properties of 2D-In_2Se_3 as mentioned, this key studied material carries a great potential to display superior water splitting efficiency. Although advances in discovering the properties of 2D-In_2Se_3 have been achieved, most of the reports are theoretically based and its applications in photocatalytic water splitting is still in an infancy stage. There appears to be no report on demonstrating sole 2D-In_2Se_3 for photocatalytic water splitting experimentally until now. There are only limited reports in using fabricated 2D-In_2Se_3 as a photocatalyst: Wang *et al.* has reported synthesizing homojunction γ-In_2Se_3 nanoparticle/α-In_2Se_3 nanosheet by a solvothermal method and has demonstrated its ability in photocatalytic H_2 evolution with S^{2-}/SO_3^{2-} sacrificial reagent and Cr(VI) removal[92]; Zhang *et al.* has synthesised g-C_3N_4/In_2Se_3 heterojunction by one-step in-situ solution-phase method and has exhibited visible-light-driven hydrogen evolution rate with the use of triethanolamine as sacrificial reagent[103]; Zhang *et al.* synthesised γ-In_2Se_3/α-In_2Se_3/rGO as a homo-heterojunction by solvothermal method and it exhibits H_2 evolution activity with the use of S^{2-}/SO_3^{2-} sacrificial reagent[104]. Currently, the limited literature of In_2Se_3 for

photocatalytic water splitting is often theoretical or involves sacrificial reagents in photocatalytic water splitting testing. It should be reiterated that it is always preferable to develop a water splitting system without sacrificial reagents, not only because it is economical, but the presence of sacrificial reagents also complicates the system, which leads to difficulties with the investigation of the reaction mechanisms as mentioned in section *1.2.3*. Therefore, the usage of sacrificial reagents is not investigated in this research project. Herein, the main objectives of this research project are to provide experimental evidence of 2D-In_2Se_3 as a photocatalyst for water splitting without the use of a sacrificial reagent, and to determine the structure-activity relationship.

This research will also explore synthesising 2D-In_2Se_3 by the intercalation lithium method and characterisation of its structure. To date, there are some recent successes in producing specific polytypes and thickness of In_2Se_3 via molecular beam epitaxy (MBE), chemical vapour deposition (CVD) and physical vapour deposition (PVD)[84, 105-108]. Although these results are encouraging, these techniques require high cost, high energy consumption and advanced instruments. Besides, the stoichiometry and polytype phase grown on specific substrates are generally difficult to control and predict. Different stoichiometric ratios exist in the In-Se system including InSe, In_3Se_4 and In_6Se_7[109]. Therefore, it is desirable to investigate new methods to synthesise 2D-In_2Se_3 in an easier and more eco-friendly manner. Our group has previously demonstrated layered materials like MoS_2 can be chemically exfoliated into 2D-layered sheets in solution through lithium intercalation method[110, 111]. Chemical exfoliation (in common solvents like water) is relatively easier, insensitive to air and can potentially be scaled up to give large quantities of exfoliated materials[112]. To date, there is no publication on the exfoliation of In_2Se_3 by lithium intercalation method and its characterisation. Therefore, in this research project, I proposed for the first time to use the

lithium intercalation method to exfoliate In_2Se_3 into layered 2D-In_2Se_3 and its structure would be thoroughly characterised by advanced techniques.

1.3.5. Strategic designs for enhancing photocatalytic activity of 2D-In_2Se_3

Numerous researchers have devoted great effort to suppressing the aforesaid challenges in section *1.2.5*. However, single component photocatalysts have difficulty achieving high water splitting activity and need to address all the requirements of an ideal semiconductor: it needs to have a sufficient thermodynamic potential to achieve overall water splitting (over 1.23 eV with a suitable bandgap position) while having a sufficiently narrow bandgap to harvest the visible light in solar energy (1.5-3.2 eV) that accounts for 43% of total solar energy[113, 114]. It also requires circumventing the issue related to the rapid recombination of photogenerated charge carriers. Due to these stringent requirements, undecorated single component photocatalysts for water splitting with reasonable activities are hard to obtain. Therefore, single component photocatalysts are often modified with different strategies to tackle these challenges. Common strategies aim to extend the absorption spectrum, improve spatial separation of photogenerated charges and facilitate the transport phenomena.

Like every single photocatalytic semiconductor, it is anticipated that 2D-In_2Se_3 as a single photocatalyst semiconductor is unlikely to achieve an excellent water splitting performance. Therefore, apart from studying the undecorated 2D-In_2Se_3, several strategies have been employed as an initial point to strategically enhance the photocatalytic activity of 2D-In_2Se_3 in this research. They include (1) photocatalytic reactions at an elevated temperature; (2) metal doping as cocatalyst and (3) heterojunction formation.

1.3.5.1. Photocatalytic reactions at an elevated temperature

The photocatalytic reaction will be conducted at an elevated temperature in this research. This is a novel approach compared to conventional photocatalytic water splitting reaction conditions as they are usually conducted at ambient conditions including room temperature. Unlike the conventional approach, this is inspired by a breakthrough with the use of the thermo-photo concept that was first demonstrated by Li *et al.*[115]. In this report, heat energy (maintaining the system at 543 K) is coupled with light irradiation for the synergetic amelioration of water splitting activities in an Au/N-doped TiO_2/MgO (111) system. This system has achieved a stunning hydrogen evolution rate of over 11,000 μmol g^{-1} h^{-1} without any sacrificial reagent. The report also showed that the necessary high temperature can be supplied through a solar concentrator, which focuses the solar light beam to provide both the heat and photon energy for the reaction. This is an environmentally friendly way to provide the required heat for the reaction as it does not involve extra energy input other than solar energy. It has been successfully demonstrated that the temperature (543 K) could be maintained by the simulated solar irradiation with a solar concentrator.

It is proposed that this thermo-photo activity enhancement effect can be translated to the 2D-In_2Se_3 system in this research by the explanation as follows: the elevated reaction temperature can lead to enhanced photocatalytic water splitting performance by increasing the concentration of H^+ and OH^- at saturated water vapour pressure at high temperatures. The increased concentration of H^+ and OH^- is attributed to the temperature-dependent ionic dissociation of water. The water splitting activity might peak at around 543 K, as this temperature coincides with the maximal water ionic dissociation constant (in which the ionic dissociation constant of water at 543 K is about four orders of magnitude compared with that at room temperature)[116]. As higher concentrations of H^+ and OH^- are produced at a high

temperature, more charge species are adsorbed on the surface of the semiconductor. Consequently, the adsorption of the charged ions might create a local electric field (LEF) to further attract opposite charge species, suppressing the charge recombination and prolonging exciton lifetime, eventually enhancing the overall photocatalytic activity.

1.3.5.2. Metal doping as cocatalyst

It is well-established that doping metal cocatalysts onto a photocatalyst can significantly improve the water splitting efficiency. To date, the exact reaction sites of photocatalysts for water splitting are not well-understood. They might be located either directly on the surface of the semiconductor (interface between the photocatalysts and water) within which photoexcitation took place in the bulk, or indirectly across the interface at the surface of another semiconductor or metal nanoparticles, which is referred to as the cocatalyst. It is generally believed that the cocatalysts provide active sites for the two redox reactions in water splitting by decreasing the activation energy for HER or OER[117].

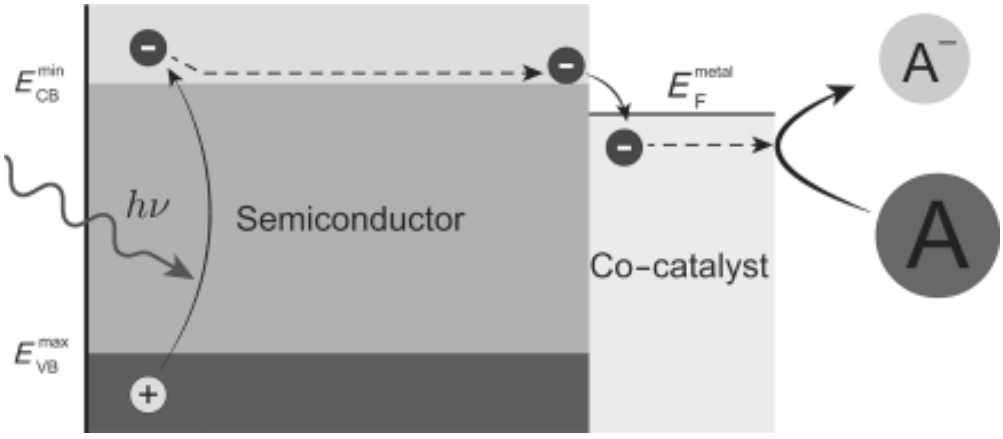

Fig. 1.9. Photogenerated electron transfer from a semiconductor photocatalyst to the acceptor molecule via a metal cocatalyst. Reproduced with permission from John Wiley and Sons from reference [35].

Moreover, a cocatalyst is considered to be able to promote charge separation and suppress the charge recombination process by extracting photoexcited electrons or holes. For example, when metal cocatalysts (HER cocatalyst) are supported on the semiconductor, the photo-generated electrons are accepted by the metal, because the available states of its Fermi level lie energetically below the CB states of the semiconductor in general cases. Given that the Fermi level of the metal is lower in energy than the CB of the semiconductor, this shifts the Fermi level of the semiconductor-metal composite upwards, so that its potential becomes more negative (*i.e.* more reducing, with more overpotential to drive the reaction kinetically), which is depicted in Fig. 1.9. Thus, the electrons are shuttled to the reactants and are more kinetically driven to undergo the H^+/H_2 reduction than by the photocatalysts themselves. The formation of the Schottky barrier at the semiconductor-metal interface promotes the separation of charge carriers by the accumulation of electrons in the metal, while holes remain in the semiconductor. The improved charge carriers' separation translates to slower recombination rates and, thus, increases the efficiency of the process.

The choice of cocatalyst must be finely tuned in terms of energy levels and electronic structure so to ensure the charge flow is in the right direction at the semiconductor-cocatalyst interface[34]. In general, Pt, Rh, Ru, Ir and Ni are the promotor for HER while oxides of Co, Fe, Ni, Mn, Ru and Ir are the cocatalysts for OER[118]. It is well-known that Pt, Ni, Rh and Ru are excellent promotors for HER as they can lower overpotential. Nevertheless, they can also catalyse a backward water formation reaction, which limits their usefulness as cocatalysts in overall water splitting, especially when the later reaction is a thermodynamically more favourable process[119].

Sole cocatalysts for HER or OER and the co-deposition of both HER and OER cocatalysts are all used to improve the activity of a semiconductor. HER cocatalysts can help to improve

H^+ reduction as a photocatalytic water splitting system often has an insufficient overpotential than that for H_2O oxidation; individual OER cocatalysts can boost the slow concerted four-electrons oxygen formation reaction which is widely considered as the bottleneck of water splitting reaction[117]. Even though dual cocatalyst can hugely enhance the performance and durability compared to single cocatalyst for some photocatalysts[120, 121], the location of two cocatalysts and the optimisation of the loading amount of each cocatalyst needs to be adjusted carefully.

There has been very little coverage of metal-doped In_2Se_3 as cocatalyst in literature. The most related literature is the theoretical work by Li *et al.*[81]. They demonstrated that As doping at Se sites in In_2Se_3 monolayers exhibits enhanced ferromagnetism compared to the bulk. The work by Yang *et al.* revealed that Fe-doped 2D-In_2Se_3 can be synthesised by chemical vapour transport technique and the Fe doping at the In sites induces multiferroic in 2D-In_2Se_3[122]. The two pieces of literature show that 2D-In_2Se_3 has the potential to be doped with metals, but other than that, the link between this research project remains minimal.

The photocatalytic effect of metal-doped 2D-In_2Se_3 is still seemingly unknown in the literature. Herein, the metal-doping strategy would be employed to try to enhance the photocatalytic water splitting activity. A range of metals were doped to 2D-In_2Se_3 to discover the cocatalyst that delivers the best water splitting performance. The metal-doped 2D-In_2Se_3 with the highest activity is further characterised to investigate more about its structure-activity relationship, hoping to give insights in further developing highly efficient 2D-In_2Se_3-based photocatalysts.

1.3.5.3. Heterojunction formation

Heterojunction formation is another well-established strategy for enhancing photocatalytic activity. A heterojunction is formed when a semiconductor couples with another semiconductor. It can improve photocatalytic activity due to the potential of broadening light-harvesting properties, improving utilisation of light absorption and increasing chemical stability[123]. Depending on the bandgaps and the electronic affinity of semiconductors, heterojunction structures can be divided into three types: type-I, type-II and type-III band alignment as shown in Fig. 1.10.

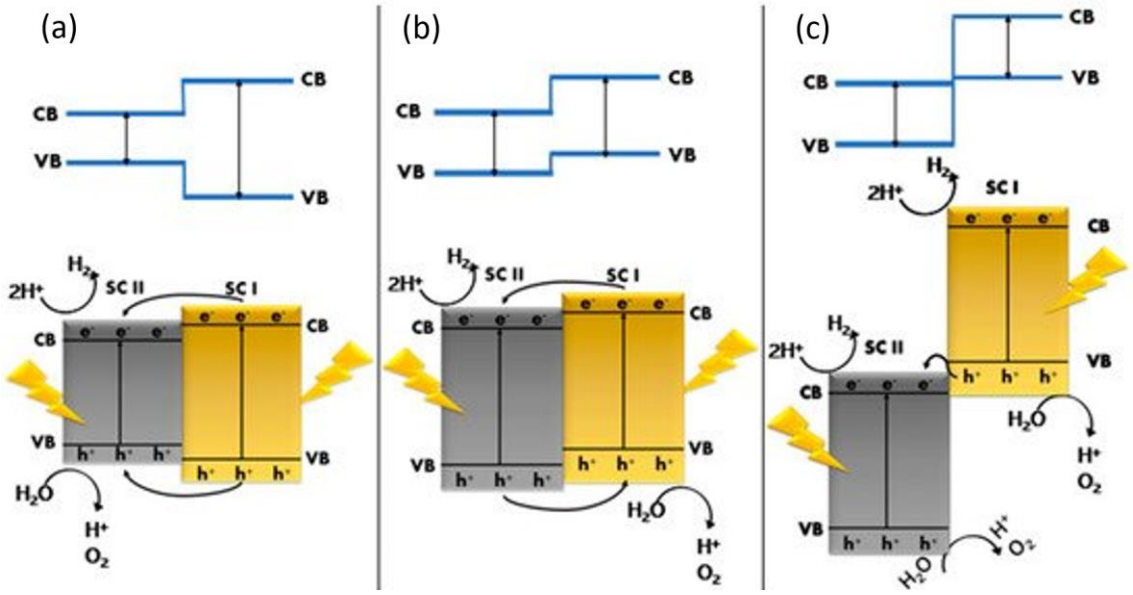

Fig. 1.10. Schematic band diagram of the three types of semiconductor junctions. (a) Type-I, (b) Type-II and (c) Type-III. SC is short-termed for semiconductors. Reproduced with the open access figure with permission of MDPI from reference [124].

Among the three types of semiconductor junctions, only type-II heterostructure is beneficial for enhancing the water splitting activity. In a type-II band alignment, the position of VB and CB of the second semiconductor is higher than that of the first semiconductor, and the steps in the bands go in the same direction, unlike type-I and type-III heterojunction. The

difference of the chemical potential between the two semiconductors causes band bending at the interface of the junction, inducing a build-in field that drives the photogenerated electrons and holes to move in an opposite direction – holes transfer to the less positive VB while electrons transfer to the less negative CB. It promotes the effective separation of electron-hole pairs by spatially distributing the photogenerated electron and hole in CBM and VBM, respectively, in two different materials. Therefore, type-II semiconductor heterojunction is the specific type of heterojunction that is suitable for enhancing water splitting efficiency.

Furthermore, a wide bandgap semiconductor can couple with a narrow bandgap semiconductor to improve the light absorption efficiency. For example, a UV excited semiconductor (*e.g.* TiO_2 and ZnO) can couple with a visible light excited semiconductor (CdS and g-C_3N_4)[125]. This improves the solar energy utilisation efficiency from the extension of the light response range to a larger solar spectrum by the synergic absorption of two semiconductors with different bandgaps. It can also circumvent the band position requirements to match the two redox potentials of water splitting because the redox reactions no longer take place in a single semiconductor. Thus, more semiconductors can be chosen to form the photocatalyst for water splitting.

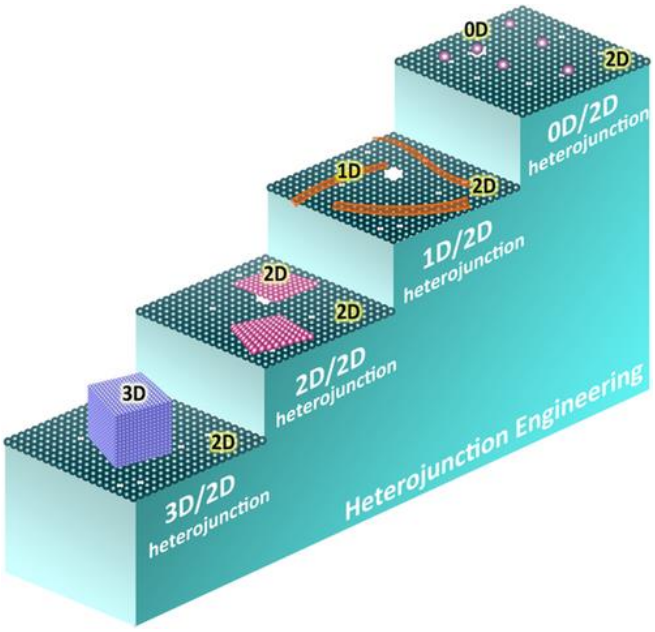

Fig. 1.11. Heterojunction of 0D/2D interface (point to face contact), 1D/2D interface (line to face contact), 2D/2D (face to face contact) and 3D/2D interface (bulk to face contact). Reproduced with permission from Wiley from reference [126].

Various type-II heterojunction structures have been explored. Compared with pure semiconductors, these type-II heterojunctions including CdS/TiO_2[127], ZnO/ZnS[128], ZnO/WSe_2[129], CdS/MoS_2[130], and CdS/ZnS[131] have achieved greater photocatalytic activity and solar energy absorption. Numerous synthesis techniques, such as chemical vapour deposition, chemical deposition, electrochemical deposition, ion exchange, electrostatic assembly, and solvothermal/hydrothermal methods have been well-developed to prepare type-II heterojunction structures. Nanoscale or low-dimensional (0D, 1D and 2D) functional components are often incorporated in the formation of type-II heterojunction due to their large surface area and significantly enhanced light absorption efficiency. The heterojunction structures can form by different dimensions, for example, 3D/2D, 2D/2D, 1D/2D and 0D/2D (Fig. 1.11). Among these, 2D/2D heterojunction received more attention because of their high overlapping surface area that can provide better charge separation, more active sites

and amenability for efficient charge transfer[132]. These are all beneficial for increasing energy conversion efficiency. The above descriptions only briefly discuss the main principle of type-II heterojunctions and mentioned a few recent breakthroughs; readers are encouraged to gain a deeper understanding of type-II water splitting heterojunction systems with their compositions, construction and synthesis techniques, and their water splitting performance from excellent review papers[124, 125, 133, 134].

In this research, it is proposed that 2D-In_2Se_3 is suitable for building heterojunctions with other materials with different electronic states. The heterojunction formation is believed to be able to create novel materials with emergent synergistic phenomena such as enhancement in the absorption of solar light, efficient charge separation and longer charge carrier lifetime[126, 135, 136].

2D-MoS_2 is chosen to construct a heterojunction structure with 2D-In_2Se_3 in this project. 2D-MoS_2 is well-studied in our group as a photocatalytic water splitting material with numerous ground-breaking discoveries[111, 137]. By lithium intercalation method, MoS_2 can be exfoliated to a 2D layered material, presuming to have a similar structure with 2D-In_2Se_3 so the heterojunction could be more easily formed[93]. It is proposed that the heterojunction structure formed between 2D-In_2Se_3 and 2D-MoS_2 would form a 2D/2D heterojunction catalyst with enhanced photocatalytic performance.

To date, several reports have been published that focused on 2D-In_2Se_3/2D-MoS_2 heterojunction structure. Zou *et al.* and Mohapatra *et al.* independently synthesised the van der Waals epitaxial formation of In_2Se_3/MoS_2 heterostructures by a typical two-step CVD method. The material displayed a promising photoresponsivity and specific detectivity which have a potential application in high-performance broadband photodetectors[138, 139]. The two reports show the In_2Se_3/MoS_2 heterojunction displays certain stability and can be

successfully synthesised, even though the application is not directly linked to this research project. In the report of Yuan *et al.*, they used a dry transfer method to fabricate the In_2Se_3/MoS_2 van der Waals heterostructure. They demonstrated an enhanced piezoelectric property resulting from the type-II band alignment, which causes a larger interfacial dipole moment than the individual In_2Se_3 and MoS_2[140]. This intriguing report gave an insight into the In_2Se_3/MoS_2 heterojunction as a type-II heterojunction leading to a larger interfacial dipole moment, which facilitates efficient charge separation and suppresses charge recombination compared to the two separated semiconductors. Therefore, using In_2Se_3/MoS_2 heterojunction may be a promising approach for splitting water effectively. κ-In_2Se_3/MoS_2 was assembled by a solution-based ultrasonic method by Jiang *et al.* and it was shown that the material as a photoanode exhibited diminished photo-generated charge recombination, improved photocurrent density and higher photoelectrochemical OER performance than its pristine components[141]. Even though our project is not focused on κ-In_2Se_3, a rarely reported metastable In_2Se_3 phase, and photoelectrochemical water splitting, this report demonstrates the heterojunction formed between In_2Se_3 and MoS_2 can benefit photogenerated charge transfer and decrease charge recombination. Finally, Zhang *et al.* have theoretically constructed an In_2Se_3/MoS_2 heterojunction composite by DFT[93]. The results also revealed that it is a type-II heterojunction structure and is thermodynamically stable. There was a photogenerated charge migration from MoS_2 to In_2Se_3, which again confirms that the heterojunction can promote the charge separation and suppress charge recombination. The mobility of the charge carriers in the composite was also excellent due to their small effective mass. Furthermore, the composite has outstanding optical absorption of infrared, visible and ultraviolet light, meaning it has excellent absorption of solar light spectrum. This report shows an encouraging theoretical vision that In_2Se_3/MoS_2 is a potential material for experimental research in the field of photocatalytic water splitting.

In light of the previous research, MoS_2/In_2Se_3 is anticipated to be a promising photocatalyst for water splitting. Here, I propose to construct the heterojunction by a facile electrostatic self-assembly approach for the first time (experimental details in section *3.2.4*). This method can be done under ambient conditions; unlike CDV and PCD, this approach is not energy-intensive and does not require an advanced instrumental setup. After the assembly, the series of heterojunctions with a range of component ratios will be tested. The one with optimal activity would be robustly characterised to further understand its structure. It is hoped that this experimental research could open doors to design next-generation 2D/2D heterojunction-based photocatalysts for water splitting.

1.3.5.4. Other related strategies

The photocatalytic reactions will be done by vigorously mixing the colloidal or suspension solution by adding a stirring system with a magnetic bar. As mentioned, interfacial mass diffusional transfer of reactants is one of the limitations to the rate of water splitting reaction. Therefore, fresh H_2O molecules need to be constantly transported to the active sites on the surface of the photocatalyst to undergo water splitting by vigorously mixing.

1.4. Aims and objectives

As discussed in the previous sections, the hydrogen evolution reaction via photocatalytic water splitting has the potential to play a crucial role in the move towards a decarbonised-energy society.

The aim of this thesis is to provide an understanding of the photocatalysis chemistry of 2D-In_2Se_3 based materials for water splitting. To reiterate, there is no previous experimental study conducted regarding the use of 2D-In_2Se_3, which is synthesised by the lithium intercalation method, for photocatalytic water splitting. It is hoped that this research can

provide insight into synthesising and engineering more effective 2D-In_2Se_3 based photocatalysts so as to contribute to the industrialisation of this technology.

The objective of this thesis is to systematically study the 2D-In_2Se_3 photocatalytic water splitting chemistry in the following manner: (i) the structure-activity relationship of 2D-In_2Se_3; to study the enhanced photocatalytic effect in water splitting reaction by (ii) doping metal into 2D-In_2Se_3 and (iii) the formation of MoS_2/In_2Se_3 heterojunction structures.

1.5. Thesis overview

This thesis contains five chapters with Chapter 3 and Chapter 4 detailing the research performed throughout my MSc (by research) degree.

Chapter 1 introduces the fundamentals of water splitting and outlines the challenges in the development of photocatalysts for this reaction. Additionally, a background description and a review of strategies for enhancing the photocatalytic performance used in the experimental work is provided.

Chapter 2 provides an overview and brief theoretical discussion of the operational principles of the analytical techniques used.

Chapter 3 details the experimental protocols followed during the synthesis of 2D-In_2Se_3 and its related decorated forms, characterisations and activity testing of catalysts reported in the following chapter.

Chapter 4 details the characterisations and investigates the structure-activity relationship of 2D-In_2Se_3. Furthermore, the enhanced activity and the characterisations of a range of metal-doped 2D-In_2Se_3 and MoS_2/In_2Se_3 heterojunction structures were explored.

Chapter 5 concludes the thesis and suggests possible future works.

1.6. References

1. Niu, H., Correlations between crude oil and stocks prices of renewable energy and technology companies: A multiscale time-dependent analysis. *Energy* **2021,** *221*, 119800.
2. Qadir, S. A.; Al-Motairi, H.; Tahir, F.; Al-Fagih, L., Incentives and strategies for financing the renewable energy transition: A review. *Energy Reports* **2021,** *7*, 3590-3606.
3. Bhandari, R.; Shah, R. R., Hydrogen as energy carrier: Techno-economic assessment of decentralized hydrogen production in Germany. *Renewable Energy* **2021,** *177*, 915-931.
4. IEA, World Energy Outlook 2019. **2019**.
5. IEA, Net Zero by 2050: A Roadmap for the Global Energy Sector. **2021**.
6. El Haj Assad, M.; Alhuyi Nazari, M.; Rosen, M. A., Chapter 1 - Applications of renewable energy sources. In *Design and Performance Optimization of Renewable Energy Systems*, Assad, M. E. H.; Rosen, M. A., Eds. Academic Press: 2021; pp 1-15.
7. Londoño-Pulgarin, D.; Cardona-Montoya, G.; Restrepo, J. C.; Muñoz-Leiva, F., Fossil or bioenergy? Global fuel market trends. *Renewable and Sustainable Energy Reviews* **2021,** *143*, 110905.
8. Barone, G.; Buonomano, A.; Forzano, C.; Giuzio, G. F.; Palombo, A., Increasing renewable energy penetration and energy independence of island communities: A novel dynamic simulation approach for energy, economic, and environmental analysis, and optimization. *Journal of Cleaner Production* **2021,** *311*, 127558.
9. Shahbaz, M.; Topcu, B. A.; Sarıgül, S. S.; Vo, X. V., The effect of financial development on renewable energy demand: The case of developing countries. *Renewable Energy* **2021,** *178*, 1370-1380.
10. Duan, J.; van Kooten, G. C.; Liu, X., Renewable electricity grids, battery storage and missing money. *Resources, Conservation and Recycling* **2020,** *161*, 105001.
11. Karamov, D. N., Methodology for calculating the lifetime of storage batteries in autonomous energy systems with renewable power generation. *Energy Reports* **2020,** *6*, 15-24.
12. da Silva Lima, L.; Quartier, M.; Buchmayr, A.; Sanjuan-Delmás, D.; Laget, H.; Corbisier, D.; Mertens, J.; Dewulf, J., Life cycle assessment of lithium-ion batteries and vanadium redox flow batteries-based renewable energy storage systems. *Sustainable Energy Technologies and Assessments* **2021,** *46*, 101286.
13. Su, T.; Lyu, N.; Zhao, Z.; Wang, H.; Jin, Y., Safety warning of lithium-ion battery energy storage station via venting acoustic signal detection for grid application. *Journal of Energy Storage* **2021,** *38*, 102498.
14. Council, W.; Wyman, O., World Energy Trilemma Index 2020. *World Energy Council: London, UK* **2020**.
15. Falcone, P. M.; Hiete, M.; Sapio, A., Hydrogen economy and sustainable development goals: Review and policy insights. *Current Opinion in Green and Sustainable Chemistry* **2021,** *31*, 100506.
16. Xing, H.; Stuart, C.; Spence, S.; Chen, H., Alternative fuel options for low carbon maritime transportation: Pathways to 2050. *Journal of Cleaner Production* **2021,** *297*, 126651.
17. McCay, M. H.; Shafiee, S., 22 - Hydrogen: An Energy Carrier. In *Future Energy (Third Edition)*, Letcher, T. M., Ed. Elsevier: 2020; pp 475-493.
18. Møller, K. T.; Jensen, T. R.; Akiba, E.; Li, H.-w., Hydrogen - A sustainable energy carrier. *Progress in Natural Science: Materials International* **2017,** *27* (1), 34-40.
19. Miao, B.; Giordano, L.; Chan, S. H., Long-distance renewable hydrogen transmission via cables and pipelines. *International Journal of Hydrogen Energy* **2021,** *46* (36), 18699-18718.
20. Oliveira, A. M.; Beswick, R. R.; Yan, Y., A green hydrogen economy for a renewable energy society. *Current Opinion in Chemical Engineering* **2021,** *33*, 100701.
21. IEA, The Future of Hydrogen: Seizing today's opportunities. **2019**.
22. Fujishima, A.; Honda, K., Electrochemical Photolysis of Water at a Semiconductor Electrode. *Nature* **1972,** *238* (5358), 37-38.

23. Usgs.gov, How Much Water is There on Earth? https://www.usgs.gov/special-topic/water-science-school/science/how-much-water-there-earth?qt-science_center_objects=0#qt-science_center_objects. last accessed 13 July 2021.
24. Van Leeuwen, P. W., *Homogeneous catalysis: understanding the art*. Springer Science & Business Media: 2006.
25. Kakaei, K.; Esrafili, M. D.; Ehsani, A., Chapter 1 - Introduction to Catalysis. In *Interface Science and Technology*, Kakaei, K.; Esrafili, M. D.; Ehsani, A., Eds. Elsevier: 2019; Vol. 27, pp 1-21.
26. Zeng, M.; Li, Y., Recent advances in heterogeneous electrocatalysts for the hydrogen evolution reaction. *Journal of Materials Chemistry A* **2015,** *3* (29), 14942-14962.
27. Ekspong, J.; Gracia-Espino, E.; Wågberg, T., Hydrogen Evolution Reaction Activity of Heterogeneous Materials: A Theoretical Model. *The Journal of Physical Chemistry C* **2020,** *124* (38), 20911-20921.
28. Sabatier, P., Hydrogénations et déshydrogénations par catalyse. *Berichte der deutschen chemischen Gesellschaft* **1911,** *44* (3), 1984-2001.
29. Kosaka, T.; Teduka, Y.; Ogura, T.; Zhou, Y.; Hisatomi, T.; Nishiyama, H.; Domen, K.; Takahashi, Y.; Onishi, H., Transient Kinetics of O2 Evolution in Photocatalytic Water-Splitting Reaction. *ACS Catalysis* **2020,** *10* (22), 13159-13164.
30. Fabbri, E.; Schmidt, T. J., Oxygen evolution reaction—the enigma in water electrolysis. ACS Publications: 2018.
31. Li, X.; Cheng, Z.; Wang, X., Understanding the mechanism of oxygen evolution reaction (OER) with the consideration of spin. *arXiv pre-print server* **2020**.
32. Narayanan, H.; Viswanathan, B.; Krishnamurthy, K. R.; Nair, H., Hydrogen from photo-electrocatalytic water splitting. In *Solar Hydrogen Production*, Elsevier: 2019; pp 419-486.
33. Li, R.; Li, C., Chapter One - Photocatalytic Water Splitting on Semiconductor-Based Photocatalysts. In *Advances in Catalysis*, Song, C., Ed. Academic Press: 2017; Vol. 60, pp 1-57.
34. Wang, Q.; Domen, K., Particulate Photocatalysts for Light-Driven Water Splitting: Mechanisms, Challenges, and Design Strategies. *Chemical Reviews* **2020,** *120* (2), 919-985.
35. Habisreutinger, S. N.; Schmidt-Mende, L.; Stolarczyk, J. K., Photocatalytic Reduction of CO2 on TiO2 and Other Semiconductors. *Angewandte Chemie International Edition* **2013,** *52* (29), 7372-7408.
36. Hisatomi, T.; Kubota, J.; Domen, K., Recent advances in semiconductors for photocatalytic and photoelectrochemical water splitting. *Chemical Society Reviews* **2014,** *43* (22), 7520-7535.
37. Liu, J.; Liu, Y.; Liu, N.; Han, Y.; Zhang, X.; Huang, H.; Lifshitz, Y.; Lee, S.-T.; Zhong, J.; Kang, Z., Metal-free efficient photocatalyst for stable visible water splitting via a two-electron pathway. *Science* **2015,** *347* (6225), 970-974.
38. Kisch, H., Semiconductor Photocatalysis—Mechanistic and Synthetic Aspects. *Angewandte Chemie International Edition* **2013,** *52* (3), 812-847.
39. Bahnemann, D. W.; Hilgendorff, M.; Memming, R., Charge carrier dynamics at TiO2 particles: reactivity of free and trapped holes. *The Journal of Physical Chemistry B* **1997,** *101* (21), 4265-4275.
40. Colombo, D. P.; Bowman, R. M., Does Interfacial Charge Transfer Compete with Charge Carrier Recombination? A Femtosecond Diffuse Reflectance Investigation of TiO2 Nanoparticles. *The Journal of Physical Chemistry* **1996,** *100* (47), 18445-18449.
41. Hakki, A.; Schneider, J.; Bahnemann, D., CHAPTER 2 Understanding the Chemistry of Photocatalytic Processes. In *Photocatalysis: Fundamentals and Perspectives*, The Royal Society of Chemistry: 2016; pp 29-50.
42. Li, X.; Yu, J.; Low, J.; Fang, Y.; Xiao, J.; Chen, X., Engineering heterogeneous semiconductors for solar water splitting. *Journal of Materials Chemistry A* **2015,** *3* (6), 2485-2534.
43. Kamat, P. V., Manipulation of Charge Transfer Across Semiconductor Interface. A Criterion That Cannot Be Ignored in Photocatalyst Design. *The Journal of Physical Chemistry Letters* **2012,** *3* (5), 663-672.

44. Zhu, S.; Wang, D., Photocatalysis: Basic Principles, Diverse Forms of Implementations and Emerging Scientific Opportunities. *Advanced Energy Materials* **2017,** *7* (23), 1700841.
45. Eliseeva, S. V.; Bünzli, J.-C. G., Rare earths: jewels for functional materials of the future. *New Journal of Chemistry* **2011,** *35* (6), 1165-1176.
46. Mei, B.; Han, K.; Mul, G. D., Driving Surface Redox Reactions in Heterogeneous Photocatalysis: The Active State of Illuminated Semiconductor-Supported Nanoparticles during Overall Water-Splitting. *Acs Catalysis* **2018,** *8* (10), 9154-9164.
47. Sathre, R.; Scown, C. D.; Morrow, W. R.; Stevens, J. C.; Sharp, I. D.; Ager, J. W.; Walczak, K.; Houle, F. A.; Greenblatt, J. B., Life-cycle net energy assessment of large-scale hydrogen production via photoelectrochemical water splitting. *Energy & Environmental Science* **2014,** *7* (10), 3264-3278.
48. Burns, G., 10 - Band Theory. In *Solid State Physics*, Burns, G., Ed. Academic Press: San Diego, 1985; pp 241-352.
49. Godin, R.; Wang, Y.; Zwijnenburg, M. A.; Tang, J.; Durrant, J. R., Time-Resolved Spectroscopic Investigation of Charge Trapping in Carbon Nitrides Photocatalysts for Hydrogen Generation. *Journal of the American Chemical Society* **2017,** *139* (14), 5216-5224.
50. Wang, X.; Xu, Q.; Li, M.; Shen, S.; Wang, X.; Wang, Y.; Feng, Z.; Shi, J.; Han, H.; Li, C., Photocatalytic Overall Water Splitting Promoted by an α–β phase Junction on Ga2O3. *Angewandte Chemie International Edition* **2012,** *51* (52), 13089-13092.
51. Guo, L.; Chen, Y.; Su, J.; Liu, M.; Liu, Y., Obstacles of solar-powered photocatalytic water splitting for hydrogen production: A perspective from energy flow and mass flow. *Energy* **2019,** *172*, 1079-1086.
52. Pu, Y.-C.; Kibria, M. G.; Mi, Z.; Zhang, J. Z., Ultrafast Exciton Dynamics in InGaN/GaN and Rh/Cr2O3 Nanoparticle-Decorated InGaN/GaN Nanowires. *The Journal of Physical Chemistry Letters* **2015,** *6* (13), 2649-2656.
53. Corp, K. L.; Schlenker, C. W., Ultrafast Spectroscopy Reveals Electron-Transfer Cascade That Improves Hydrogen Evolution with Carbon Nitride Photocatalysts. *Journal of the American Chemical Society* **2017,** *139* (23), 7904-7912.
54. Tamaki, Y.; Furube, A.; Murai, M.; Hara, K.; Katoh, R.; Tachiya, M., Dynamics of efficient electron–hole separation in TiO2 nanoparticles revealed by femtosecond transient absorption spectroscopy under the weak-excitation condition. *Physical Chemistry Chemical Physics* **2007,** *9* (12), 1453-1460.
55. Granqvist, C. G., Transparent conductors as solar energy materials: A panoramic review. *Solar Energy Materials and Solar Cells* **2007,** *91* (17), 1529-1598.
56. Walter, M. G.; Warren, E. L.; McKone, J. R.; Boettcher, S. W.; Mi, Q.; Santori, E. A.; Lewis, N. S., Solar Water Splitting Cells. *Chemical Reviews* **2010,** *110* (11), 6446-6473.
57. Fan, L.; Wang, Y. X.; Li, L., Surfactants modified egg shells for removal of methyl violet from aqueous solutions. *Desalination and Water Treatment* **2018,** *124*, 319-325.
58. Liao, L.; Zhang, Q.; Su, Z.; Zhao, Z.; Wang, Y.; Li, Y.; Lu, X.; Wei, D.; Feng, G.; Yu, Q.; Cai, X.; Zhao, J.; Ren, Z.; Fang, H.; Robles-Hernandez, F.; Baldelli, S.; Bao, J., Efficient solar water-splitting using a nanocrystalline CoO photocatalyst. *Nature Nanotechnology* **2014,** *9* (1), 69-73.
59. Chuayboon, S.; Abanades, S.; Rodat, S., Stepwise Solar Methane Reforming and Water-Splitting via Lattice Oxygen Transfer in Iron and Cerium Oxides. *Energy Technology* **2020,** *8* (8), 1900415.
60. Jeong, H. H.; Kwak, J. H.; Han, G. Y.; Yoon, K. J., Stepwise production of syngas and hydrogen through methane reforming and water splitting by using a cerium oxide redox system. *International Journal of Hydrogen Energy* **2011,** *36* (23), 15221-15230.
61. Kumaravel, V.; Imam, M. D.; Badreldin, A.; Chava, R. K.; Do, J. Y.; Kang, M.; Abdel-Wahab, A., Photocatalytic hydrogen production: role of sacrificial reagents on the activity of oxide, carbon, and sulfide catalysts. *Catalysts* **2019,** *9* (3), 276.
62. Schneider, J.; Bahnemann, D. W., Undesired Role of Sacrificial Reagents in Photocatalysis. *The Journal of Physical Chemistry Letters* **2013,** *4* (20), 3479-3483.

63. Guzman, F.; Chuang, S. S. C.; Yang, C., Role of Methanol Sacrificing Reagent in the Photocatalytic Evolution of Hydrogen. *Industrial & Engineering Chemistry Research* **2013,** *52* (1), 61-65.
64. Galińska, A.; Walendziewski, J., Photocatalytic Water Splitting over Pt−TiO2 in the Presence of Sacrificial Reagents. *Energy & Fuels* **2005,** *19* (3), 1143-1147.
65. Zhao, J.; Shi, R.; Li, Z.; Zhou, C.; Zhang, T., How to make use of methanol in green catalytic hydrogen production? *Nano Select* **2020,** *1* (1), 12-29.
66. Husin, H.; Alam, P.; Zaki, M.; Hasfita, F. In *Enhanced photocatalytic hydrogen production from water-ethanol solution by Ruthenium doped La-NaTaO3*, IOP Conference Series: Materials Science and Engineering, IOP Publishing: 2018; p 012003.
67. Enzweiler, H.; Yassue-Cordeiro, P. H.; Schwaab, M.; Barbosa-Coutinho, E.; Olsen Scaliante, M. H. N.; Fernandes, N. R. C., Catalyst concentration, ethanol content and initial pH effects on hydrogen production by photocatalytic water splitting. *Journal of Photochemistry and Photobiology A: Chemistry* **2020,** *388*, 112051.
68. Cao, B.; Yu, Y.; Xu, S.; Qu, J.; Gao, G.; Li, H.; Gao, N.; Ren, Y.; Zhou, C., Selective photocatalytic C–C coupling of isopropanol into pinacol with concurrent hydrogen evolution over GONaOH photocatalyst. *New Journal of Chemistry* **2019,** *43* (4), 1936-1942.
69. Smirnova, E.; Ermakov, V.; Rozenkevich, M., Photocatalytic formation of hydrogen in aqueous-alcohol solutions of cobalt cyanide complexes. *Kinetics and Catalysis* **2000,** *41* (1), 48-51.
70. Yu, S.; Webster, R. D.; Zhou, Y.; Yan, X., Ultrathin gC 3 N 4 nanosheets with hexagonal CuS nanoplates as a novel composite photocatalyst under solar light irradiation for H 2 production. *Catalysis Science & Technology* **2017,** *7* (10), 2050-2056.
71. Liu, R.; Fang, S.-Y.; Dong, C.-D.; Tsai, K.-C.; Yang, W.-D., Enhancing hydrogen evolution of water splitting under solar spectra using Au/TiO2 heterojunction photocatalysts. *International Journal of Hydrogen Energy* **2021**.
72. Cao, B.; Li, G.; Li, H., Hollow spherical RuO2@TiO2@Pt bifunctional photocatalyst for coupled H2 production and pollutant degradation. *Applied Catalysis B: Environmental* **2016,** *194*, 42-49.
73. Lv, D.; Lei, Y.; Zhang, D.; Song, X.; Li, Y.-W.; Niemantsverdriet, J. W. H.; Hao, W.; Deng, Y.; Su, R., Effect of Pd and Au on Hydrogen Abstraction and C–C Cleavage in Photoconversion of Glycerol: Beyond Charge Separation. *The Journal of Physical Chemistry C* **2020,** *124* (37), 20320-20327.
74. Ng, K. H.; Lai, S. Y.; Cheng, C. K.; Cheng, Y. W.; Chong, C. C., Photocatalytic water splitting for solving energy crisis: Myth, Fact or Busted? *Chemical Engineering Journal* **2021,** *417*, 128847.
75. Fu, C.-F.; Sun, J.; Luo, Q.; Li, X.; Hu, W.; Yang, J., Intrinsic Electric Fields in Two-dimensional Materials Boost the Solar-to-Hydrogen Efficiency for Photocatalytic Water Splitting. *Nano Letters* **2018,** *18* (10), 6312-6317.
76. Ju, L.; Shang, J.; Tang, X.; Kou, L., Tunable photocatalytic water splitting by the ferroelectric switch in a 2D AgBiP2Se6 monolayer. *Journal of the American Chemical Society* **2019,** *142* (3), 1492-1500.
77. Ju, L.; Qin, J.; Shi, L.; Yang, G.; Zhang, J.; Sun, L., Rolling the WSSe bilayer into double-walled nanotube for the enhanced photocatalytic water-splitting performance. *Nanomaterials* **2021,** *11* (3), 705.
78. Caliskan, S.; Kim, J. K.; Han, G. S.; Qin, F.; Cho, I. S.; Han, H. S.; Lee, J.-K., Enhancing Solar Water Splitting of Textured BiVO4 by Dual Effect of a Plasmonic Silver Nanoshell: Plasmon-Induced Light Absorption and Enhanced Hole Transport. *ACS Applied Energy Materials* **2020,** *3* (12), 11886-11892.
79. Chen, S.-H.; Jiang, Y.-S.; Lin, H.-y., Easy Synthesis of BiVO4 for Photocatalytic Overall Water Splitting. *ACS Omega* **2020,** *5* (15), 8927-8933.
80. Li, Y.; Gao, J.; Li, Q.; Peng, M.; Sun, X.; Li, Y.; Yuan, G.; Wen, W.; Meyyappan, M., Thermal phase transformation of In2Se3 nanowires studied by in situsynchrotron radiation X-ray diffraction. *Journal of Materials Chemistry* **2011,** *21* (19), 6944-6947.

81. Li, X.; Zuo, X.; Li, H.; Han, L.; Gao, Q.; Li, D.; Cui, B.; Liu, D.; Qu, F., Exotic magnetism in As-doped α/β-In2Se3 monolayers with tunable anisotropic carrier mobility. *Physical Chemistry Chemical Physics* **2019,** *21* (35), 19234-19241.
82. Zhao, P.; Ma, Y.; Lv, X.; Li, M.; Huang, B.; Dai, Y., Two-dimensional III2-VI3 materials: Promising photocatalysts for overall water splitting under infrared light spectrum. *Nano Energy* **2018,** *51*, 533-538.
83. Balakrishnan, N.; Steer, E. D.; Smith, E. F.; Kudrynskyi, Z. R.; Kovalyuk, Z. D.; Eaves, L.; Patanè, A.; Beton, P. H., Epitaxial growth of γ -InSe and α , β , and γ -In 2 Se 3 on ε -GaSe. *2D Materials* **2018,** *5* (3), 035026.
84. Cui, C.; Hu, W.-J.; Yan, X.; Addiego, C.; Gao, W.; Wang, Y.; Wang, Z.; Li, L.; Cheng, Y.; Li, P.; Zhang, X.; Alshareef, H. N.; Wu, T.; Zhu, W.; Pan, X.; Li, L.-J., Intercorrelated In-Plane and Out-of-Plane Ferroelectricity in Ultrathin Two-Dimensional Layered Semiconductor In2Se3. *Nano Letters* **2018,** *18* (2), 1253-1258.
85. Geim, A. K.; Novoselov, K. S., The rise of graphene. *Nature Materials* **2007,** *6* (3), 183-191.
86. Haque, F.; Daeneke, T.; Kalantar-Zadeh, K.; Ou, J. Z., Two-Dimensional Transition Metal Oxide and Chalcogenide-Based Photocatalysts. *Nanomicro Lett* **2018,** *10* (2), 23.
87. Singh, A. K.; Mathew, K.; Zhuang, H. L.; Hennig, R. G., Computational Screening of 2D Materials for Photocatalysis. *The Journal of Physical Chemistry Letters* **2015,** *6* (6), 1087-1098.
88. Pagona, G.; Bittencourt, C.; Arenal, R.; Tagmatarchis, N., Exfoliated semiconducting pure 2H-MoS2 and 2H-WS2 assisted by chlorosulfonic acid. *Chemical Communications* **2015,** *51* (65), 12950-12953.
89. Sahoo, D.; Kumar, B.; Sinha, J.; Ghosh, S.; Roy, S. S.; Kaviraj, B., Cost effective liquid phase exfoliation of MoS2 nanosheets and photocatalytic activity for wastewater treatment enforced by visible light. *Scientific Reports* **2020,** *10* (1), 10759.
90. Zhao, J.; Holmes, M. A.; Osterloh, F. E., Quantum Confinement Controls Photocatalysis: A Free Energy Analysis for Photocatalytic Proton Reduction at CdSe Nanocrystals. *ACS Nano* **2013,** *7* (5), 4316-4325.
91. Quereda, J.; Biele, R.; Rubio-Bollinger, G.; Agraït, N.; D'Agosta, R.; Castellanos-Gomez, A., Strong Quantum Confinement Effect in the Optical Properties of Ultrathin α-In2Se3. *Advanced Optical Materials* **2016,** *4* (12), 1939-1943.
92. Wang, R.; Wan, J.; Jia, J.; Xue, W.; Hu, X.; Liu, E.; Fan, J., Synthesis of In2Se3 homojunction photocatalyst with α and γ phases for efficient photocatalytic performance. *Materials & Design* **2018,** *151*, 74-82.
93. Zhang, J.-R.; Deng, X.-Z.; Gao, B.; Chen, L.; Au, C.-T.; Li, K.; Yin, S.-F.; Cai, M.-Q., Theoretical study on the intrinsic properties of In 2 Se 3/MoS 2 as a photocatalyst driven by near-infrared, visible and ultraviolet light. *Catalysis Science & Technology* **2019,** *9* (17), 4659-4667.
94. Jiang, J.; Xu, T.; Lu, J.; Sun, L.; Ni, Z., Defect Engineering in 2D Materials: Precise Manipulation and Improved Functionalities. *Research* **2019,** *2019*, 4641739.
95. Jung, K. Y.; Park, S. B.; Anpo, M., Photoluminescence and photoactivity of titania particles prepared by the sol–gel technique: effect of calcination temperature. *Journal of Photochemistry and Photobiology A: Chemistry* **2005,** *170* (3), 247-252.
96. Yamakata, A.; Vequizo, J. J. M.; Kawaguchi, M., Behavior and Energy State of Photogenerated Charge Carriers in Single-Crystalline and Polycrystalline Powder SrTiO3 Studied by Time-Resolved Absorption Spectroscopy in the Visible to Mid-Infrared Region. *The Journal of Physical Chemistry C* **2015,** *119* (4), 1880-1885.
97. Qian, R.; Zong, H.; Schneider, J.; Zhou, G.; Zhao, T.; Li, Y.; Yang, J.; Bahnemann, D. W.; Pan, J. H., Charge carrier trapping, recombination and transfer during TiO2 photocatalysis: An overview. *Catalysis Today* **2019,** *335*, 78-90.
98. Zhang, L.; Zunger, A., Evolution of Electronic Structure as a Function of Layer Thickness in Group-VIB Transition Metal Dichalcogenides: Emergence of Localization Prototypes. *Nano Letters* **2015,** *15* (2), 949-957.

99. Qiao, J.; Kong, X.; Hu, Z.-X.; Yang, F.; Ji, W., High-mobility transport anisotropy and linear dichroism in few-layer black phosphorus. *Nature Communications* **2014,** *5* (1), 4475.
100. Voiry, D.; Yamaguchi, H.; Li, J.; Silva, R.; Alves, D. C.; Fujita, T.; Chen, M.; Asefa, T.; Shenoy, V. B.; Eda, G., Enhanced catalytic activity in strained chemically exfoliated WS 2 nanosheets for hydrogen evolution. *Nature materials* **2013,** *12* (9), 850-855.
101. Gupta, U.; Rao, C. N. R., Hydrogen generation by water splitting using MoS2 and other transition metal dichalcogenides. *Nano Energy* **2017,** *41*, 49-65.
102. Sun, Y.; Sun, Z.; Gao, S.; Cheng, H.; Liu, Q.; Piao, J.; Yao, T.; Wu, C.; Hu, S.; Wei, S.; Xie, Y., Fabrication of flexible and freestanding zinc chalcogenide single layers. *Nature Communications* **2012,** *3* (1), 1057.
103. Zhang, S.; Xu, D.; Chen, X.; Zhang, S.; An, C., Construction of ultrathin 2D/2D g-C3N4/In2Se3 heterojunctions with high-speed charge transfer nanochannels for promoting photocatalytic hydrogen production. *Applied Surface Science* **2020,** *528*, 146858.
104. Zhang, Q.; Wang, R.; Xie, X.; Tang, C.; Hu, X.; Fan, J.; Liu, E., Fabrication of γ-In2Se3/α-In2Se3/rGO homo-heterojunction for efficient photocatalytic hydrogen evolution. *International Journal of Hydrogen Energy* **2020,** *45* (58), 33370-33380.
105. Xue, F.; Zhang, J.; Hu, W.; Hsu, W.-T.; Han, A.; Leung, S.-F.; Huang, J.-K.; Wan, Y.; Liu, S.; Zhang, J.; He, J.-H.; Chang, W.-H.; Wang, Z. L.; Zhang, X.; Li, L.-J., Multidirection Piezoelectricity in Mono- and Multilayered Hexagonal α-In2Se3. *ACS Nano* **2018,** *12* (5), 4976-4983.
106. Zhou, J.; Zeng, Q.; Lv, D.; Sun, L.; Niu, L.; Fu, W.; Liu, F.; Shen, Z.; Jin, C.; Liu, Z., Controlled Synthesis of High-Quality Monolayered α-In2Se3 via Physical Vapor Deposition. *Nano Letters* **2015,** *15* (10), 6400-6405.
107. Zheng, W.; Xie, T.; Zhou, Y.; Chen, Y.; Jiang, W.; Zhao, S.; Wu, J.; Jing, Y.; Wu, Y.; Chen, G., Patterning two-dimensional chalcogenide crystals of Bi 2 Se 3 and In 2 Se 3 and efficient photodetectors. *Nature communications* **2015,** *6* (1), 1-8.
108. Okamoto, T.; Nakada, Y.; Aoki, T.; Takaba, Y.; Yamada, A.; Konagai, M., Structural control of In2Se3 polycrystalline thin films by molecular beam epitaxy. *physica status solidi c* **2006,** *3* (8), 2796-2799.
109. Wei, D.; Lin, Z.; Cui, Z.; Su, S.; Zhang, D.; Cao, M.; Hu, C., Two-step fabrication of a porous γ-In 2 Se 3 tetragonal photocatalyst for water splitting. *Chemical Communications* **2013,** *49* (83), 9609-9611.
110. Liu, G.; Robertson, A. W.; Li, M. M.-J.; Kuo, W. C. H.; Darby, M. T.; Muhieddine, M. H.; Lin, Y.-C.; Suenaga, K.; Stamatakis, M.; Warner, J. H.; Tsang, S. C. E., MoS2 monolayer catalyst doped with isolated Co atoms for the hydrodeoxygenation reaction. *Nature Chemistry* **2017,** *9* (8), 810-816.
111. Lau, T. H. M.; Foord, J. S.; Tsang, S. C. E., 2D molybdenum disulphide nanosheets incorporated with single heteroatoms for the electrochemical hydrogen evolution reaction. *Nanoscale* **2020,** *12* (19), 10447-10455.
112. Coleman, J. N.; Lotya, M.; O'Neill, A.; Bergin, S. D.; King, P. J.; Khan, U.; Young, K.; Gaucher, A.; De, S.; Smith, R. J.; Shvets, I. V.; Arora, S. K.; Stanton, G.; Kim, H. Y.; Lee, K.; Kim, G. T.; Duesberg, G. S.; Hallam, T.; Boland, J. J.; Wang, J. J.; Donegan, J. F.; Grunlan, J. C.; Moriarty, G.; Shmeliov, A.; Nicholls, R. J.; Perkins, J. M.; Grieveson, E. M.; Theuwissen, K.; McComb, D. W.; Nellist, P. D.; Nicolosi, V., Two-Dimensional Nanosheets Produced by Liquid Exfoliation of Layered Materials. *Science* **2011,** *331* (6017), 568-571.
113. Peng, Q.; Xiong, R.; Sa, B.; Zhou, J.; Wen, C.; Wu, B.; Anpo, M.; Sun, Z., Computational mining of photocatalysts for water splitting hydrogen production: two-dimensional InSe-family monolayers. *Catalysis Science & Technology* **2017,** *7* (13), 2744-2752.
114. Fu, S. C.; Zhong, X. L.; Zhang, Y.; Lai, T. W.; Chan, K. C.; Lee, K. Y.; Chao, C. Y. H., Bio-inspired cooling technologies and the applications in buildings. *Energy and Buildings* **2020,** *225*, 110313.
115. Li, Y. Y.; Peng, Y. K.; Hu, L. S.; Zheng, J. W.; Prabhakaran, D.; Wu, S.; Puchtler, T. J.; Li, M.; Wong, K. Y.; Taylor, R. A.; Tsang, S. C. E., Photocatalytic water splitting by N-TiO2

on MgO (111) with exceptional quantum efficiencies at elevated temperatures. *Nature Communications* **2019,** *10*.
116. Bandura, A. V.; Lvov, S. N., The ionization constant of water over wide ranges of temperature and density. *Journal of physical and chemical reference data* **2006,** *35* (1), 15-30.
117. Wang, Z.; Li, C.; Domen, K., Recent developments in heterogeneous photocatalysts for solar-driven overall water splitting. *Chemical Society Reviews* **2019,** *48* (7), 2109-2125.
118. Chen, S.; Takata, T.; Domen, K., Particulate photocatalysts for overall water splitting. *Nature Reviews Materials* **2017,** *2* (10), 17050.
119. Maeda, K.; Domen, K., Photocatalytic Water Splitting: Recent Progress and Future Challenges. *The Journal of Physical Chemistry Letters* **2010,** *1* (18), 2655-2661.
120. Ohno, T.; Bai, L.; Hisatomi, T.; Maeda, K.; Domen, K., Photocatalytic Water Splitting Using Modified GaN:ZnO Solid Solution under Visible Light: Long-Time Operation and Regeneration of Activity. *Journal of the American Chemical Society* **2012,** *134* (19), 8254-8259.
121. Lin, L.; Wang, C.; Ren, W.; Ou, H.; Zhang, Y.; Wang, X., Photocatalytic overall water splitting by conjugated semiconductors with crystalline poly(triazine imide) frameworks. *Chemical Science* **2017,** *8* (8), 5506-5511.
122. Yang, H.; Pan, L.; Xiao, M.; Fang, J.; Cui, Y.; Wei, Z., Iron-doping induced multiferroic in two-dimensional In2Se3. *Science China Materials* **2020,** *63* (3), 421-428.
123. Sudha, D.; Sivakumar, P., Review on the photocatalytic activity of various composite catalysts. *Chemical Engineering and Processing: Process Intensification* **2015,** *97*, 112-133.
124. San Martín, S.; Rivero, M. J.; Ortiz, I., Unravelling the Mechanisms that Drive the Performance of Photocatalytic Hydrogen Production. *Catalysts* **2020,** *10* (8), 901.
125. Wang, Y.; Wang, Q.; Zhan, X.; Wang, F.; Safdar, M.; He, J., Visible light driven type II heterostructures and their enhanced photocatalysis properties: a review. *Nanoscale* **2013,** *5* (18), 8326-8339.
126. Ong, W.-J.; Shak, K. P. Y., 2D/2D heterostructured photocatalysts: an emerging platform for artificial photosynthesis. *Solar Rrl* **2020,** *4* (8), 2000132.
127. Khatamian, M.; Saket Oskoui, M.; Haghighi, M.; Darbandi, M., Visible-light response photocatalytic water splitting over CdS/TiO2 and CdS–TiO2/metalosilicate composites. *International Journal of Energy Research* **2014,** *38* (13), 1712-1726.
128. Devaraji, P.; Mapa, M.; Abdul Hakkeem, H. M.; Sudhakar, V.; Krishnamoorthy, K.; Gopinath, C. S., ZnO–ZnS Heterojunctions: A Potential Candidate for Optoelectronics Applications and Mineralization of Endocrine Disruptors in Direct Sunlight. *ACS Omega* **2017,** *2* (10), 6768-6781.
129. Hu, F.; Tao, L.; Ye, H.; Li, X.; Chen, X., ZnO/WSe2 vdW heterostructure for photocatalytic water splitting. *Journal of Materials Chemistry C* **2019,** *7* (23), 7104-7113.
130. Kadam, S. R.; Gosavi, S. W.; Kale, B. B.; Suzuki, N.; Terashima, C.; Fujishima, A., Unique CdS@MoS2 Core Shell Heterostructure for Efficient Hydrogen Generation Under Natural Sunlight. *Scientific Reports* **2019,** *9* (1), 12036.
131. Nasir, J. A.; Rehman, Z. u.; Shah, S. N. A.; Khan, A.; Butler, I. S.; Catlow, C. R. A., Recent developments and perspectives in CdS-based photocatalysts for water splitting. *Journal of Materials Chemistry A* **2020,** *8* (40), 20752-20780.
132. Kim, I. Y.; Jo, Y. K.; Lee, J. M.; Wang, L.; Hwang, S.-J., Unique advantages of exfoliated 2D nanosheets for tailoring the functionalities of nanocomposites. *The journal of physical chemistry letters* **2014,** *5* (23), 4149-4161.
133. Afroz, K.; Moniruddin, M.; Bakranov, N.; Kudaibergenov, S.; Nuraje, N., A heterojunction strategy to improve the visible light sensitive water splitting performance of photocatalytic materials. *Journal of Materials Chemistry A* **2018,** *6* (44), 21696-21718.
134. Daulbayev, C.; Sultanov, F.; Bakbolat, B.; Daulbayev, O., 0D, 1D and 2D nanomaterials for visible photoelectrochemical water splitting. A Review. *International Journal of Hydrogen Energy* **2020**.

135. Shanker, G. S.; Biswas, A.; Ogale, S. B., 2D materials and their heterostructures for photocatalytic water splitting and conversion of CO2 to value chemicals and fuels. *Journal of Physics: Energy* **2021**.
136. Su, T.; Shao, Q.; Qin, Z.; Guo, Z.; Wu, Z., Role of Interfaces in Two-Dimensional Photocatalyst for Water Splitting. *ACS Catalysis* **2018,** *8* (3), 2253-2276.
137. Li, Y.; Wu, S.; Zheng, J.; Peng, Y.-K.; Prabhakaran, D.; Taylor, R. A.; Tsang, S. C. E., 2D photocatalysts with tuneable supports for enhanced photocatalytic water splitting. *Materials Today* **2020**.
138. Zou, Z.; Li, D.; Liang, J.; Zhang, X.; Liu, H.; Zhu, C.; Yang, X.; Li, L.; Zheng, B.; Sun, X.; Zeng, Z.; Yi, J.; Zhuang, X.; Wang, X.; Pan, A., Epitaxial synthesis of ultrathin β-In2Se3/MoS2 heterostructures with high visible/near-infrared photoresponse. *Nanoscale* **2020,** *12* (11), 6480-6488.
139. Mohapatra, P. K.; Ranganathan, K.; Dezanashvili, L.; Houben, L.; Ismach, A., Epitaxial growth of In2Se3 on monolayer transition metal dichalcogenide single crystals for high performance photodetectors. *Applied Materials Today* **2020,** *20*, 100734.
140. Yuan, S.; Io, W. F.; Mao, J.; Chen, Y.; Luo, X.; Hao, J., Enhanced Piezoelectric Response of Layered In2Se3/MoS2 Nanosheet-Based van der Waals Heterostructures. *ACS Applied Nano Materials* **2020,** *3* (12), 11979-11986.
141. Jiang, Y.; Wang, Q.; Han, L.; Zhang, X.; Jiang, L.; Wu, Z.; Lai, Y.; Wang, D.; Liu, F., Construction of In2Se3/MoS2 heterojunction as photoanode toward efficient photoelectrochemical water splitting. *Chemical Engineering Journal* **2019,** *358*, 752-758.

Chapter 2: Analytical techniques

Answering the question 'what is the structure of the material' is key in understanding the structure-activity relationships in catalysis. As such, characterisations of catalysts have become a vital step in designing a catalyst rationally and intelligently.

No single technique can provide a comprehensive characterisation of a substance; various analytical techniques are needed to identify its structures. There are three main groups of characterisation techniques: microscopy, spectroscopy and diffraction techniques according to the classification of West *et al.*[1]. The techniques presented in the research work will be discussed in the following chapter in terms of the theories and applications. Electrochemical and band structure determination are also employed in the research, so will also be discussed in the chapter. Most of the characterisations are focusing on the surface where the catalysis reaction happens or interacts with reactants, and therefore require most attention in catalysis studies.

2.1. Microscopic techniques

Microscopy is a technique that uses microscopes to view small objects that are otherwise invisible to naked eyes. One traditional way to see small objects is through a common optical microscope, using magnifying lenses to produce surface images with focused visible light. However, the spatial resolution of optical microscopes (in the range of μm) is not enough to distinguish nanoscale materials in catalysts, or distance between atoms. This is because the resolving power of imaging instruments is governed by the Rayleigh criterion stated in Eq. 2.1.

$$\theta = \frac{1.22\lambda}{D} \qquad (2.1)$$

where θ is the angular separation that the centres of two objects are just resolvable by the instrument, this is also the representation of resolution limit; λ is the wavelength of the light source (or electromagnetic radiation); D is the circular aperture diameter of the instrument.

Electron microscopes use electrons that have a much shorter wavelength (in the order of 10^{-10} m) than that of visible light (in the order of 10^{-7} m) as a source of imaging. Therefore, by relating the Rayleigh criterion formula in Eq. 2.1, the extreme small wavelength of electrons allows electron microscopes to have an ultrahigh-resolution (or θ) to image materials in a nanometre range and probe into atomic structures. In this project, atomic force microscopy and transmission electron microscopy are used for determining the morphology, thickness, and particle sizes of the nanoscale catalysts.

2.1.1. Atomic force microscopy

Atomic force microscopy (AFM) is a powerful technique to characterise nanomaterials' spatial properties such as size, morphology, surface texture and roughness. A wide range of particle sizes can be characterised, ranging from 1 nm to 8 μm^2. It could visualise high-resolution 3D images which is a unique feature compared to transmission electron microscopy (TEM) or scanning electron microscopy (SEM); AFM could offer a height profile of a nanomaterial quantitatively. Also, it could characterise nearly any type of nanomaterial surface (polymers, ceramics, and composites) in multiple mediums including ambient air or even liquid dispersion. This can overcome a basic drawback with SEM – SEM can only image conducting or semiconducting surfaces[3]. One disadvantage of AFM compared to SEM is the measuring size. SEM can image an area on the order of millimetres × millimetres with a depth of field in the order of millimetres. However, AFM can only image a maximum height only on the order of micrometres with a maximum scanning area of around 150 × 150 micrometres[4].

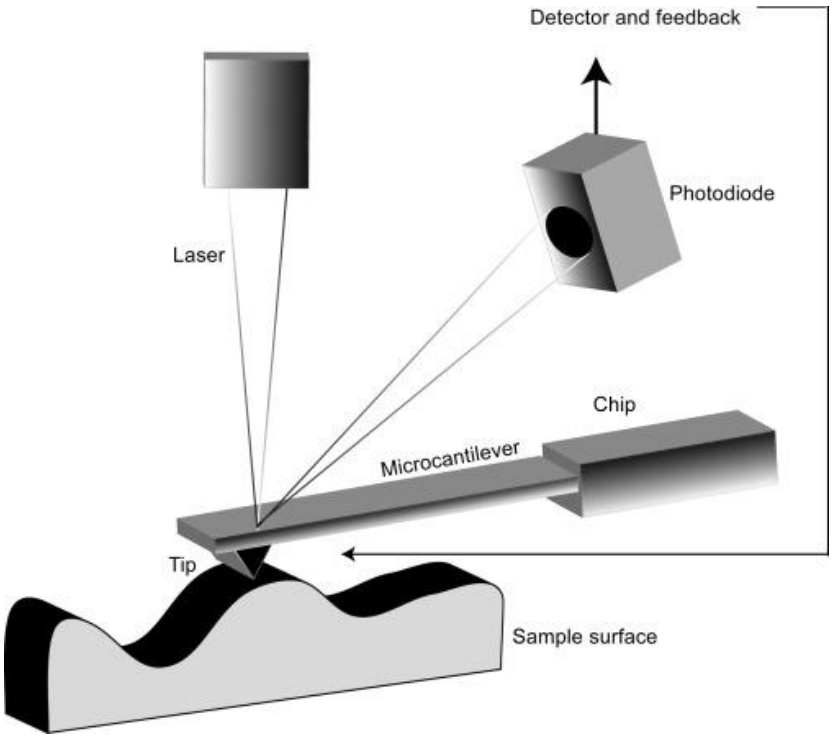

Fig. 2.1. The schematic showing the principle of AFM. Reproduced with permission from Elsevier from reference [5].

Fig. 2.1 shows the basic principle of AFM. It is based on a sharp tip that is approximately 10-20 nm[6], which is attached to a cantilever. The material of the tip is usually silicon or silicon nitride. The tip moves in response to the surface and interacts with it. The up-and-down and side-to-side motion of the cantilever is monitored through a laser beam reflected off from the back of a cantilever. The laser reflected signal is consequently tracked by a photodetector that detects the motion of the tip. The signal is then fed into a feedback loop, which is used to control the force and tip position and to track the surface for imaging and measuring. The sensitivity of the detector needs to be calibrated in terms of the length of movement corresponding to a unit of voltage measured on the detector[7].

A basic AFM can operate in two modes, contact and tapping modes[8]. In the contact mode, the tip is continuously contacting with the measured surface. In tapping mode, the cantilever is oscillating above the sample surface (at the range of frequency between 100 Hz to 2 MHz),

contacting the surface intermittently. It is the recommended mode for AFM as it minimised the potential damage by the tip. The atom at the apex of the tip senses individual atoms on the underlying surface when it starts to develop chemical bonds with each atom. These chemical interactions delicately alter the tip's vibration frequency so the surface of the materials can be detected and measured[6].

2.1.2. Transmission electron microscopy and Energy-dispersive X-ray analysis

Transmission electron microscopy (TEM) is a type of electron microscopy. It creates images by shining a high energy beam of electrons through a thin sample. The interactions between the electrons and the atoms can be used to observe the morphological features of the samples, such as crystal structure, dislocations and defects, and grain boundaries.

TEM operates on the same principles as light microscopes but instead of light, it uses electrons as the sources of energy to 'see' the image. This is due to the small wavelength of electrons that can help TEM to attain a very high resolution. The resolution of TEM depends on the wavelength of the electron, which can be tuned by changing the operating voltage that controls the electric or magnetic field. A typical operating voltage is around 80 to 200 keV, corresponding to a resolution of around 0.3 nm[9].

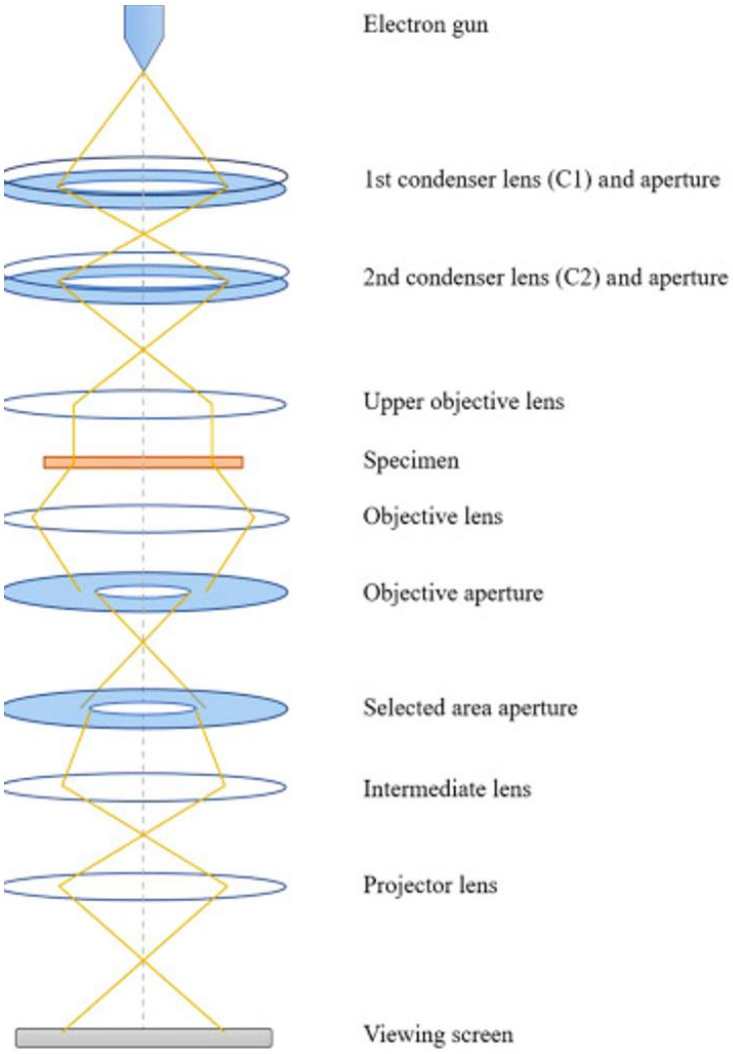

Fig. 2.2. The schematic illustration of a basic TEM setup and ray diagram. Reproduced with permission from Elsevier from reference [10].

Fig. 2.2 shows the schematic illustration of the basic setup of TEM. An electron gun, tungsten filament or LaB_6 crystal creates a beam of electrons and is accelerated to a wavelength that is smaller than the interatomic spacing using an electric or magnetic field. It is then focused into a small, thin, coherent beam by using the condenser lens. The beam then strikes the samples in which the transmittance depends on the thickness and the electron transparency of the particular part of the sample. The transmitted portion is focused by the objective lens to prevent diffraction patterns and the electron beams are converted to signal

for imaging by a charge-coupled device (CCD) or directly on a phosphor screen. The image is finally enlarged by passing through the intermediate and projector lenses column[6].

There are two operation modes of TEM: bright-field and dark-field. They utilise different electron populations to construct the TEM images and each has its advantages and disadvantages. Bright-field is the more common mode among the two and is suitable for most inspections, while dark-field can feature higher image contrast and clarity image which the bright-field technique might have difficulty providing, especially when crystalline features that are too small to be viewed (such as crystal lattice, crystal defects and dislocations)[11]. In bright-field TEM images, darker areas usually represent those areas of the sample that allow fewer electrons to transmit (the electrons are absorbed by the materials or scattered away), while light areas of the images embody more electrons were passed through. This suggests that darker areas are usually thicker than the lighter parts. The representations of dark and light areas in dark-field images are the inverse of bright-field TEM.

A limitation of TEM is that a TEM specimen must be thin enough (usually less than 100 nm) to transmit sufficient electrons to form an image with minimal energy loss[12]. Hence, specimen preparation is an important step for TEM analysis. Also, TEM is usually performed under an ultrahigh vacuum condition to avoid collision between electrons used in TEM and gas molecules, making sure the electron beam can travel in a straight manner.

Energy-dispersive X-ray (EDX) analysis can be used together with TEM or SEM. By using EDX, information such as chemical composition including its spatial distribution and concentrations can be obtained. Every atom has a unique number of electrons that reside in specific energy levels. When the electron beam hits the inner shell of an atom, it kicks off an electron from the shell and leaves a positively charged hole. An outer, higher energy electron would fill in this lower energy vacancy and thus the energy difference would be

released in the form of an X-ray. This X-ray is unique for every element and transition, which could be picked up by a detector in EDX. EDX can identify the sample compositions as well as the percentage of each element in the sample[13]. When EDX is coupled with a TEM or SEM, each specific position of the sample scan produces a spectrum that identifies the identity of elements; when it scans across the 2D surface of a sample, it can map the topography of the elements of the sample[14]. Therefore, EDX is an extremely useful technique in characterisations. However, there are some drawbacks that hinder its utility. First, the quality of the results depends heavily on the signal strength and the signal-to-noise ratio. When the concentration of an element is too low (typically below 0.5%), the amount of X-ray energy emitted might be insufficient to measure its proportion[15]. Furthermore, elements with a low atomic number are generally difficult or not able to be detected by EDX. For H and He, they only have one electron shell, and no electron will fill in the inner shell after the core electrons are excited. EDX is also a surface technique that only penetrates several nanometres in samples. Therefore, if there is a compositional discrepancy between the bulk and the surface layers, it might not be picked up by EDX[16].

2.2. Spectroscopic techniques

All the spectroscopic techniques work according to the principle of energy absorption or emission of the material, usually in the form of electromagnetic radiation. The energy of electromagnetic radiation is usually expressed in frequency, ν, or wavelength, λ of the radiation. The terms can be related to photon energy by Eq. 2.2.

$$E = h\nu = hc\lambda^{-1} \qquad (2.2)$$

where h is the Plank's constant while c is the velocity of light.

2.2.1. Electron paramagnetic resonance

Electron paramagnetic resonance (EPR) also called electron spin resonance (ESR), is a technique that affords to detect and quantify paramagnetism, the presence of unpaired electrons[17]. The technique could be applied to obtain the structure information, the mechanisms of reactions, the kinetics of the reactions and the molecular interaction or environment. Samples may be in fluid solution, solid or in a gas state.

EPR spectroscopy operates based on the absorption of microwave radiation between the Zeeman energy level of molecules in an external magnetic field. Even though the working principle of EPR is similar to nuclear magnetic resonance (NMR), most commonly, it does not vary the frequency of the radiation. Instead, it uses a monochromatic microwave source at a fixed frequency, usually conducted in X-band (9-10 GHz) or Q-band (~35 GHz)[18, 19]. The small energy splitting used in EPR is due to the quantisation of the electron spin. The formation of the energy splitting requires an external dipole magnet. When the paramagnetic molecule is placed in an axial relative to a magnetic field, B, the unpaired electron can align in either 'parallel' or 'antiparallel' (the quantum numbers are m_s = +1/2 and m_s = -1/2) to the external field, two energy states are created. The interaction between an electron spin, S, and a magnetic field, B, is called the electronic Zeeman interaction. This splitting of energy, leading to a higher and a lower energy state, results in its ability to absorb microwave.

The frequency of the microwave is normally fixed in an EPR measurement; the B field applied to the sample is varied to change the Zeeman energy instead. It means the paramagnetism of the molecule is continuously varied by a changing magnetic field. When the splitting of the energy, caused by the magnetic field, happens to be the same as the photon energy of the microwave, absorption occurs. This is the resonance condition which can be described as Eq. 2.3.

$$h\nu = g\mu_B B_0 \qquad (2.3)$$

where h is the Planck constant, ν is the frequency of the microwave, μ_B is the Bohr magneton, B_0 is the magnetic field applied in the experiment, and g is the proportionality constant. g-value is the most important parameter in EPR: it is specific for a studied material that and contains electronic information. An unpaired electron that is loosely bound and more reactive typically have a g-value closer to the g-value for a free electron *in vacuo*, g_e = 2.00232. An unpaired electron that is bound to transition metals, on the other hand, usually has a more pronounced deviation from g_e as the electron is strongly influenced by the positively charged metal nucleus. Therefore, a change of chemical environment of the unpaired electron will shift the g-factor value far away from g_e[20].

There is more magnetic interaction to determine the EPR spectra other than electronic Zeeman interaction. Electron spin S can interact with nuclei with a spin I; it is called hyperfine interaction ($S \leftrightarrow I$). If the complex has more than one unpaired electron (a high spin system), electron spins can mutually interact with each other, called zero-field interaction ($S \leftrightarrow S$). The mentioned interactions are the two relatively more common magnetic interactions observed in EPR; there are more magnetic interactions in a chemical system which are explained in detail in the excellent review of Roessler et al.[20]. These interactions create splitting patterns in an EPR spectrum reflecting the interaction of the unpaired electron with other species. The magnitude of the splitting will give indications of the chemical environment of the unpaired electron[18].

There are two approaches for EPR photon excitation: continuous-wave (CW EPR) and Fourier-transform pulsed EPR. Most EPR make use of CW EPR as it is relatively simple compared to pulsed EPR; recording and interpretation of pulse EPR spectra require sophisticated technical equipment and a more advanced theoretical background. CW EPR is

used in this project and the fundamental is as explained: a sample is excited by microwaves of a fixed frequency while the magnetic field is varied steadily through a defined range. Since B_0 could be changed easily, most EPR experiments measure the first derivative of absorption *vs.* the applied magnetic field. There are various pulsed EPR experiments including electron-nuclear double resonance spectroscopy (ENDOR), electron spin echo envelope modulation (ESEEM), and double electron-electron resonance (DEER). The measurements and principles of these techniques greatly differ from each other; they have their own possibilities and limitations and are usually only available in specialised laboratories. The details of these specialised pulsed EPR techniques are beyond the scope of this thesis.

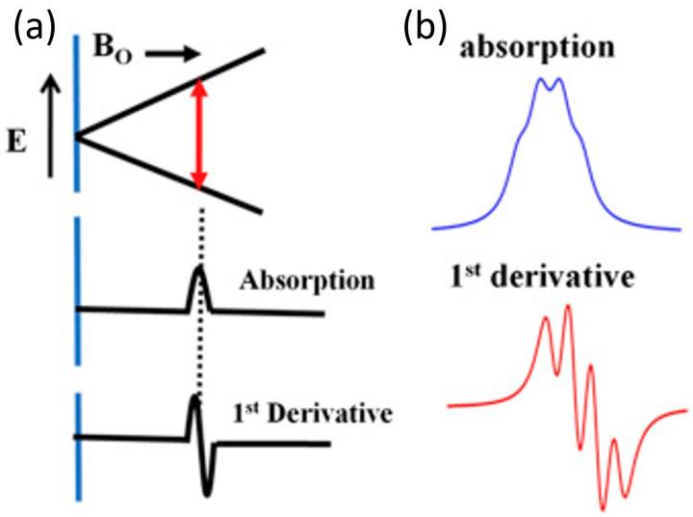

Fig. 2.3. Absorption and first derivative EPR spectra for (a) single signal and (b) signal with multiple lines with hyperfine features. Reproduced with permission from Elsevier from reference [21].

The direct detection of absorption signal is only possible for samples containing a high concentration of unpaired electrons, which is usually not the case. Background noise always appears with the signal, making the detection difficult due to the rather low signal-to-noise ratio[18]. This is overcome by field modulation using a phase-sensitive detector technique –

the first derivative of the signal is shown in Fig. 2.3 (a). The phase-sensitive detector technique will not be explained in detail here, an excellent review on this topic is illustrated by Karunakaran, *et al*[21]. Besides the noisy signal, an EPR signal is often broad and the hyperfine splitting is often hidden due to the short relaxation time of a paramagnetic system. With the use of field modulation, the derivative signal shows a well-resolved hyperfine feature as shown in Fig. 2.3 (b).

2.2.2. Raman spectroscopy

Raman spectroscopy is a spectroscopic chemical analysis technique that provides information about a material's chemical structure, phase, polymorphism and molecular interaction. It is based on the interaction of light with the chemical bonds of a material.

When light is shined on a molecule, the oscillating electromagnetic field of the light induces a polarisation of the electron cloud which leaves the molecule in a high energy state with the energy of the photon transferred to the molecule. This can be thought of as a formation of a very short-lived complex between the photon and molecule, which is commonly called the virtual state of the molecule. The virtual state is highly unstable, and the energy of the molecule will emit in the form of photon almost immediately, as scattered light.

Raman is a light scattering technique, where a molecule scatters incident light from a high-powered laser source. In the vast majority of scattering events, the scattered light has the same energy (same wavelength) after it interacts with the photon (*i.e.* Rayleigh Scattering). Rayleigh scattering is not useful in the Raman measurement as the scattered photon retains its incident wavelength (and its energy), no energy is absorbed or emitted to form a spectrum. However, in rare events (about 1 in 10 million photons), Raman scattering occurs which is an inelastic scattering process with a transfer of energy between the molecule and scattered photon. In *Stokes Raman scattering*, the molecule can gain additional energy from the

photon during the scattering and be excited to a higher vibration level. Then, the scattered photon has lower energy than the incident photons with an increased wavelength. Inversely, in *anti-Stokes Raman scattering*, the molecule can also lose energy from the scattering event by relaxing to a lower vibrational level; the scattered photon gains the corresponding energy and has a decreased wavelength. The Raman scattering processes are depicted in Fig. 2.4. Even though Stokes Raman scattering and anti-Stokes Raman scattering are equally likely to occur quantum-mechanically. The majority of molecules are in the ground vibration level due to Boltzmann distribution and thus Stokes Raman scattering is always more intense than anti-Stokes. Therefore, the Stokes Raman scattering is usually used to measure Raman spectroscopy.

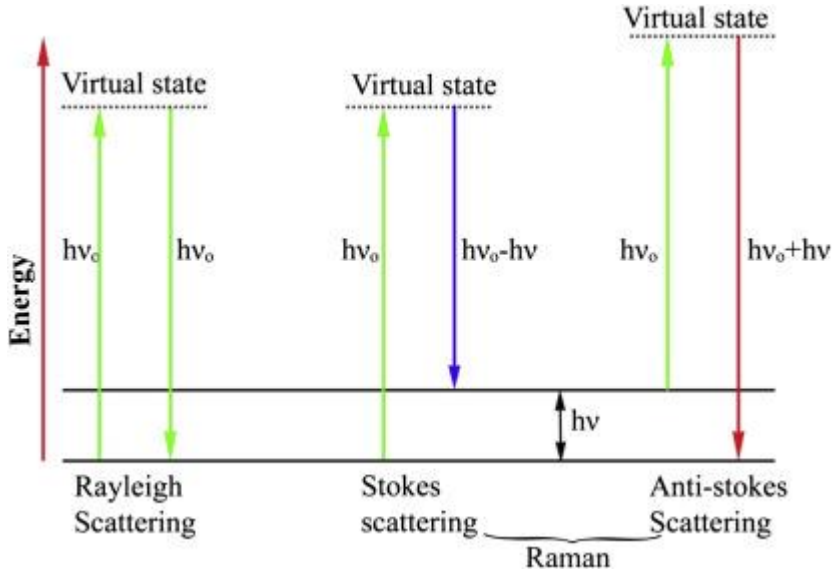

Fig. 2.4. The Jablonski diagram shows the origin of the Rayleigh, Stokes and Anti-Stokes Raman scattering process. Reproduced with permission from Elsevier from reference [22].

Laser excitation choice is one of the most important considerations for Raman spectroscopy measurement. The lasers used in Raman spectroscopy range from the UV into the near-infrared (NIR). Different wavelength regions offer advantages and disadvantages, and the selection is dictated by the sample being studied.

Raman signal intensity, N_{Raman}, is strongly wavelength-dependent by Eq. 2.4 [23].

$$N_{Raman} \sim \lambda^{-3} \qquad (2.4)$$

Therefore, when the laser wavelength is increased, the Raman scattering intensity will fall drastically. Comparing the UV and NIR lasers, the intensity of the spectrum acquired by the latter laser is less intense by a few orders. However, fluorescence, as a hindering factor, might arise and produce a much more intense signal that can effectively hide the Raman scattering signals in the background as the Raman scattering is a relatively weak process. To avoid fluorescence, different excitation lasers can be used and lasers with higher wavelengths (*i.e.* NIR lasers) usually offer a lower fluorescence than lasers with lower wavelengths. It is possible to use longer accumulation times when using NIR laser, however, there is always a risk of sample damage with prolonged laser exposure time. Therefore, a delicate balance between the laser wavelength, the laser power, and the acquisition time is needed when measuring Raman spectra.

Furthermore, different samples are measured using lasers with different wavelengths. It is impractical to compare the wavelengths of the Raman scattered light between samples as it depends on the laser used. Therefore, to compare spectra, the Raman scatter position is converted to a Raman shift away from the excitation wavelength by Eq. 2.5.

$$\Delta\bar{\nu}(cm^{-1}) = \left(\frac{1}{\lambda_0} - \frac{1}{\lambda_1}\right) \qquad (2.5)$$

where λ_0 is the wavelength of excitation laser and λ_1 is the wavelength of Raman scattering.

A Raman spectrum is plotted as intensity *vs.* Raman shift. Each Raman peak corresponds to a certain vibrational mode of a sample. Not all vibrational modes can be detected by Raman spectroscopy. To be Raman active, the vibrational mode must be corresponding to a polarisability change.

A Raman spectrum is typically a distinct chemical fingerprint for a particular material and is a relatively quick measurement. Furthermore, the intensity of a spectrum is directly proportional to concentration. A calibration procedure is needed to determine the relationship between peak intensity and concentration, and the measurements can be used to analyse the component concentrations.

2.2.3. Time-resolved photoluminescence

In the context of photocatalysis, time-resolved photoluminescence (TRPL) spectroscopy is used to measure the exciton lifetimes of photoexcited electron-hole pairs.

In a TRPL measurement system, the nonequilibrium density of electrons and holes are created by an initial laser pulse, and the excess charge carriers are relaxed by recombination. TRPL first uses an initial ultrafast pulse from mode-locked lasers, a technique in which a laser can be made to produce pulses of light with extremely short duration, to excite the samples to generate electrons and holes. Part of the recombination process, called a radiative recombination process, entails the emission of photons and is measured by an optical detector. The recombination processes without emission of photons are called the non-radiative recombination, which cannot be detected and do not contribute to the TRPL signals[24].

Charge recombination in semiconductors is an extremely fast process. In order to resolve short-duration processes, the instruments timescale must be of comparable timescale to the events under study. Therefore, ultrafast laser pulses (ps range is used in this study) are required as a source of excitation; fast detector and readout electronics were also necessary. The detector and readout system also need to be operated on the timescale of the interval between laser pulses. Together, these make TRPL a powerful technique to observe the decay of excited charge carriers created by the absorption of photons from a laser pulse.

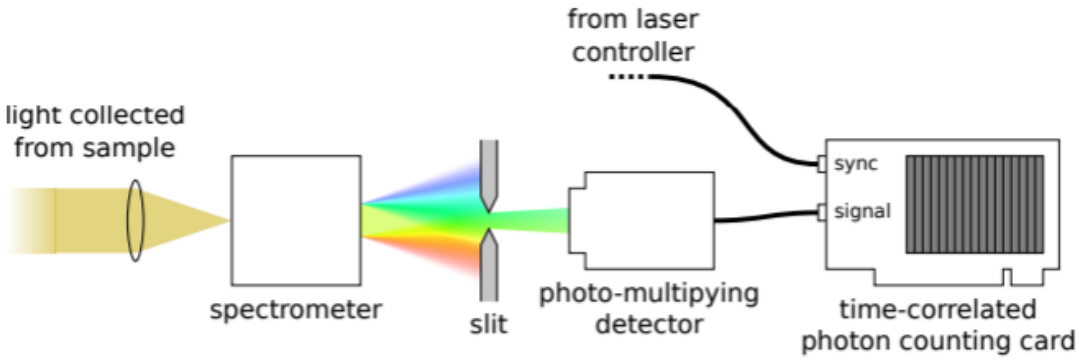

Fig. 2.5. The schematic shows the TRPL measurement system used. The spectrometer and adjustable shutter function as a narrow band-pass filter to provide wavelength selectivity. The time-correlated photon counting card is connected to a computer for recording the data. Reproduced the open resource figure from Oxford University Research Archive (ORA) from reference [25].

Fig. 2.5 shows the schematics of a TRPL measurement system. After the laser excitation, the samples will emit light that is then collected by the spectrometer for diffraction. The light will then pass through a slit to select the wavelength to be detected by the TRPL detection system. There are two main components in the system: the photo-multiplying detector (or photomultiplier tube, PMT), which turns the photons into electrical pulses and is extremely sensitive to light, and the time-correlated single-photon counting (TCSPC) card, which records the arrival time of those pulses relative to pulses arriving at a synchronisation (sync) input.

TRPL measurements usually operate under low intensity but high-repetitive signal, the probability of detecting more than one photon in a signal period is less than unity[26]. Therefore, when TCSPC is performed over a large number of such signal periods, most of the periods detect no signals, while some periods detect one single photon and only for very limited periods, more than one photon is detected. After repeating this process over millions

of pulse periods, a histogram of the detection times relative to the laser pulse arrival times can be built up to construct the waveform (or decay curve) of the original optical pulse. Fig. 2.6 illustrates the measurement principle of TRPL.

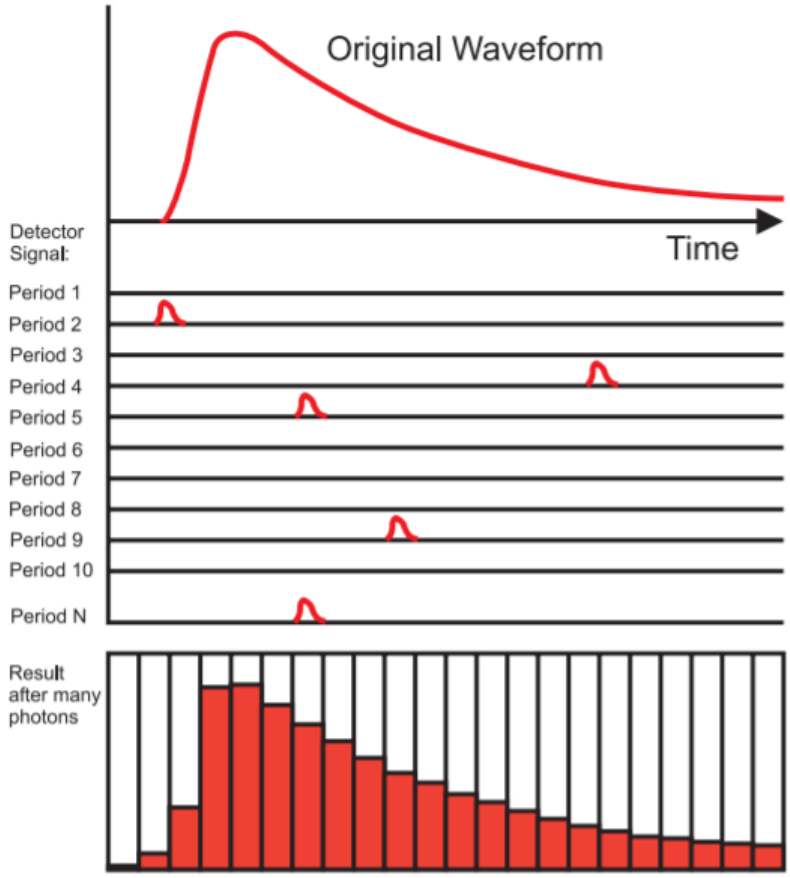

Fig. 2.6. The diagram shows the principle of TCSPC. Repeated sampling of the original waveform allows the construction of a histogram showing the number of photons detected in each signal period. The histogram resembles the original waveform. Reproduced the open resource figure from Oxford University Research Archive (ORA) from reference [26].

The TCSPC control unit is synchronised with a reference laser pulse to give time reference in a computer. It operates on the principle of recording the arrival time of each voltage pulse it receives. After a pulse arrives on the sync input, an internal timer is started. When another

sync pulse is received, the timer resets; all times are recorded relative to the last sync pulse. So, it is possible to deduce the time delay relative to the reference pulse.

The decay of the excited charge carriers carries a lot of information; a sample's energy levels and carrier dynamics can be extracted by analysing the shape of the decay curve. However, there are some limitations of TRPL. First, older TCSPCs can only record the arrival time of a single signal pulse and no further signal could be recorded until the next sync pulse arrives. Some more advanced TCPCs have the multi-stop capability that can record multiple signal pulses after a single sync pulse. Furthermore, there is a deadtime of the TCPC card. After detecting an electrical pulse from the PMT on the input channel, there is a delay before the recording operation is complete and the electronics are ready to receive another pulse. Pulses received during the deadtime are lost, leading to some data points being discarded and hence distortions in the shape of the decay curve[25]. Besides the deadtime-related issue, PMT would not respond ideally to incident photons in practice. Detectors can have flaws such as electrical reflections inside the processing circuitry which introduce random delays or secondary peaks to the electrical signal. All the limitations need to be addressed before the measurements. Therefore, commercial TRPL systems are often required to have time-consuming manual alignment or optimisation before conducting experiments; sometimes it is necessary to construct a bespoke set-up for specific experiments.

2.2.4. UV-Vis spectroscopy and UV-Vis diffuse reflectance spectroscopy

Ultraviolet-visible (UV-Vis) spectroscopy is a technique that measures the amount of UV-Vis light absorbed by the studied material as a function of wavelength. When UV-Vis light is passed through a sample, the transmittance, T, of light by a sample with respect to the intensity of light through a reference sample is measured. It can be converted to absorbance, A, by Eq. 2.6.

$$A = -\log T \qquad (2.6)$$

Most molecules will absorb photons in the UV-Vis wavelength range (UV range: 100-380 nm; visible-light range: 380-700 nm). Typical UV-Vis spectrometers use a hydrogen-deuterium lamp for the UV region that produces light from 170-375 nm and a tungsten filament lamp for the visible-light region, which produces light from 350-2500 nm.

The absorbance at various wavelengths corresponds to the structure and the concentration (in the liquid or gas phase) of the molecules. UV-Vis can be used in a qualitative or quantitative manner. The former could identify functional groups or be used as an aid to identity a compound, while the latter manner could analyse the concentration of the analyte that is related to the absorbance with Beer-Lambert law (Eq. 2.7).

$$A = \varepsilon c l \qquad (2.7)$$

where ε is the molar absorption coefficient, c is the molar concentration and l is the optical path length.

Theoretically, when a photon hits a sample, the molecule is promoted to a more excited, energetic state. UV-Vis light usually has enough energy to promote electrons to a higher electron state, from the valence band (or highest occupied molecular orbital, HOMO) to the conduction band (or lowest unoccupied molecular orbital, LUMO). The energy of the photon needs to match the bandgap. Therefore, molecules with different structures will have different bandgap energy, and thus, different absorption spectra.

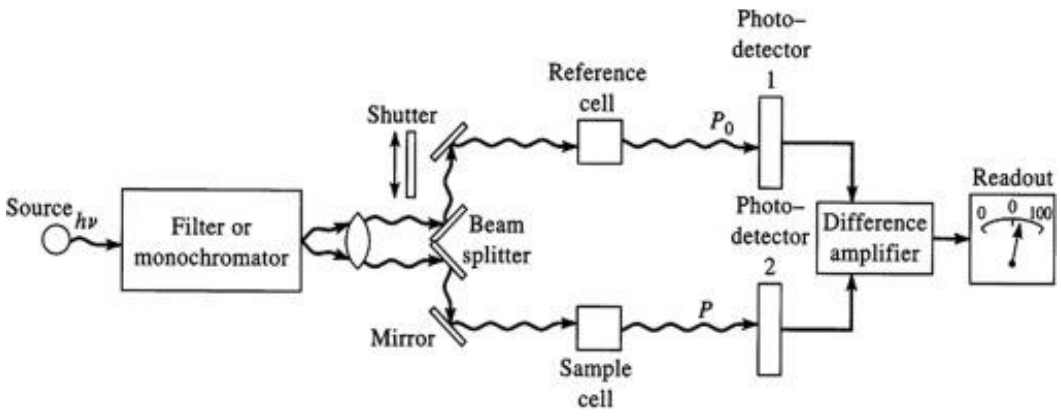

Fig. 2.7. The schematic shows the basic components of a double beam UV-Vis spectrometer. Reproduced with permission from Elsevier from reference [27].

Fig. 2.7 shows the basic design of a double beam UV-Vis spectrometer. The light source enters the instrument through the entrance slit and the polychromatic white light is dispersed to bands of monochromatic light of a single wavelength by the rotating prism or diffraction grating monochromator. Then, the exit slit selects the desired monochromatic wavelength and is further divided into two identical beams with the help of another prism. The beam passes through the sample or reference compartment (the UV-Vis cell is often made with silica or quartz as they do not absorb light in the UV region). Finally, the light passed through the cells is detected by the detector and produced signals to feed into a computer.

UV-Vis is a simple technique with versatile applications and gives rapid response regarding quantitative information including analyst concentrations and bandgap energy[28]. However, it is not the most sensitive spectroscopy technique as only a limited amount of light is absorbed over the short path length.

Generally, UV-Vis records absorption or transmission spectrum under the desirable UV-Vis range for normal incidence. The technique is used to characterise samples in thin-film or liquid form as light can pass through the thin film or the cuvette holding the solution, with

a minimal amount of dispersion. However, light cannot penetrate opaque solid samples as they do in solution; light is reflected on the surface of the samples instead.

Diffuse Reflectance Spectroscopy (DRS) is a way to circumvent this problem by recording the reflectance of a solid. DRS can also be converted to the absorbance of the sample by collecting the diffused reflected light beam. The measurement is performed by placing the sample in front of an incident light window and concentrating the UV-Vis light reflected from the sample on the detector using a sphere with a white reference inside (such as barium sulfate pallet, opal glass or ceramic). There are two types of light reflections in a DRS sphere: (1) specular reflection, where incident light is reflected symmetrically with respect to the normal; and (2) diffuse reflection, where incident light is scattered in different directions. The specular reflected light directed at the sample at an angle of 0° leaves the integrating sphere without being detected, leading to only diffuse reflected light is measured. The measured value is the reflectance with respect to the reference standard whiteboard, which is assumed as 100%[29].

2.2.5. X-ray absorption spectroscopy

X-ray absorption spectroscopy (XAS) is a bulk measurement of the elemental and chemical state analysis technique used in a broad range of disciplines. XAS requires a high intensity, coherent X-ray beam which is tunable over a wide energy range. Therefore, this must be carried out using a synchrotron radiation source[30].

XAS works by the photoelectric effect. The photoelectric effect refers to the emission of electrons from the sample surface in response to the electromagnetic radiation of light. When the X-ray energy is higher than the binding energy of the core level of the atom, photoelectrons are produced and ejected from the core atom. In the X-ray region, atoms absorb X-rays sharply at certain energy due to the absorption of incident photons by core-

level electron ejection. This energy range is referred to as the X-ray absorption edge – a characteristic of that particular species. Therefore, by controlling the energy of X-ray, one can control the type of atom to emit electrons[31].

During a measurement, a monochromatic X-ray beam is tuned to excite the electrons from the targeted atom. The intensity of the transmitted X-ray beam will drop due to the excitation and the difference between the incident beam (I_0) and transmitted beam (I_t) is expressed by Eq. 2.8.

$$I_t = I_0 e^{-\mu t} \qquad (2.8)$$

where t is the thickness of the sample and μ is the absorption coefficient. The XAS spectrum can then be plotted as μ *vs.* the energy. The most common XAS techniques are X-ray Absorption Near-Edge Structure (XANES) (or Near Edge X-Ray Absorption Fine Structure (NEXAFS)) and Extended X-ray Absorption Fine Structure (EXAFS) as shown in Fig. 2.8.

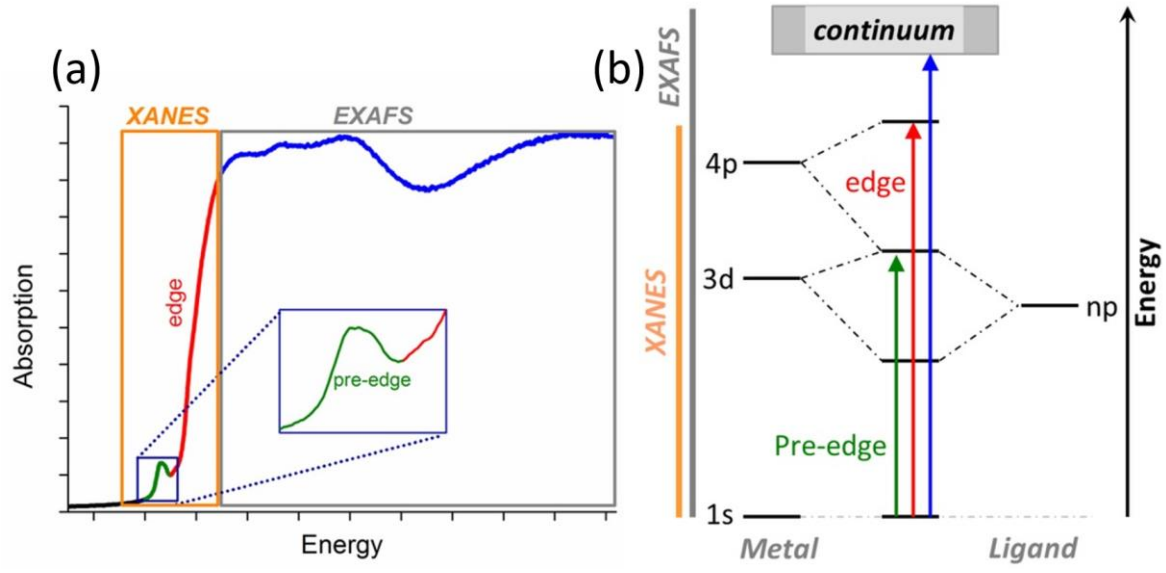

Fig. 2.8. (a) XAS spectrum marked with XANES and EXAFS, and the pre-edge and edge features. (b) The origin of the transitions corresponding to the characteristic features in an XAS spectrum. Reproduced with permission from Elsevier from reference [32].

XANES/NEXAFS: It refers to the absorption fine structure close to an absorption edge (about 10 eV below the absorption edge and 20 eV above the edge). This region shows the largest variation in the X-ray absorption according to the binding energy of the studied element. The region exhibits narrow intense resonance peaks. This part of the spectrum provides information about local atomic states, such as the electronic structure of the unoccupied levels, the oxidation states, and the ratio of chemical states of a particular element using linear combination fitting (LCF). In LCF, the XANES spectrum of an element in the target material is assumed to be constructed as the linear combination of the standard spectra. In which, the standard spectra come from the standard materials with well-defined chemical states and they are used to describe as the mixture of the states of the element in the target material[33].

EXAFS: This is the part of the spectrum starting from 50 eV above the absorption edge typically. The gentle oscillation in the measured signal originates from the scattering of the ejected photoelectron from the absorption atom and its neighbouring atoms. EXAFS measurements are used to determine local structure around the target elements, such as the elemental composition, chemical coordination environments and bonding distances.

XAS is a very powerful technique in material chemistry. Very few techniques can provide ample information about the electronic structure and the local coordination environments of the studied element. Moreover, due to the high intensity of synchrotron X-rays, it is possible to detect elements present in very low concentrations. The tunability of the radiation allows XAS to detect virtually all the elements in a relatively short period of time. The amount of sample required is also minimal due to the focused X-ray beam shining on the sample. However, like every synchrotron technique, XAS is still beamtime-limited and relatively

hard to access as there are only limited synchrotron facilities around the world. It also requires specially trained operators to monitor the instrument and analyse the data.

2.2.6. X-ray photoelectron spectroscopy

X-ray Photoelectron Spectroscopy (XPS) is a standard electron spectroscopy technique for analysing the elemental composition, empirical formula, chemical state, and electronic state of the elements of materials near the surface. XPS is initiated by irradiating a sample with monochromatic soft X-rays (200-2000 eV), usually Mg Kα (1253.6 eV) or Al Kα (1486.6 eV), to a solid surface. By Einstein's photoelectric effect, electrons will be emitted (ionised) from the occupied core (inner) atomic shells (Fig. 2.9) to the vacuum chamber. The number of ejected electrons is then counted by a detector over a range of electron kinetic energy.

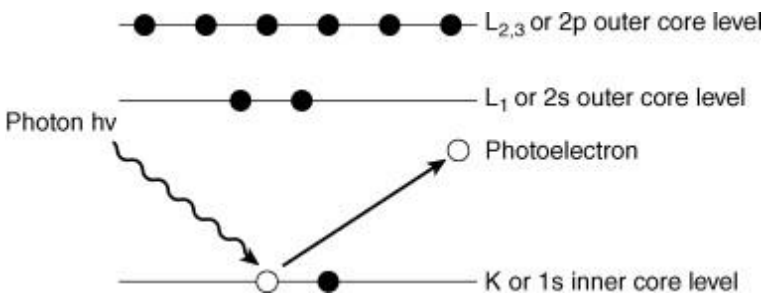

Fig. 2.9. Schematic diagram of photoemission process used for XPS. X-rays excite and eject a core-level electron. The kinetic energy of the photoelectron is then measured by the detector to find the binding energy. Reproduced with permission from Elsevier from reference [34].

The electronic kinetic energy, E, is converted to the binding energy, E_b, of the material by Eq. 2.9.

$$E = h\nu - E_b \qquad (2.9)$$

XPS spectra are plotted as counts *vs.* binding energy. Each electronic state of atoms has its own characteristic binding energy. Therefore, the peak position indicates the chemical composition, while the intensity (*i.e.* counts) measures the elemental concentration at the surface of the material[34].

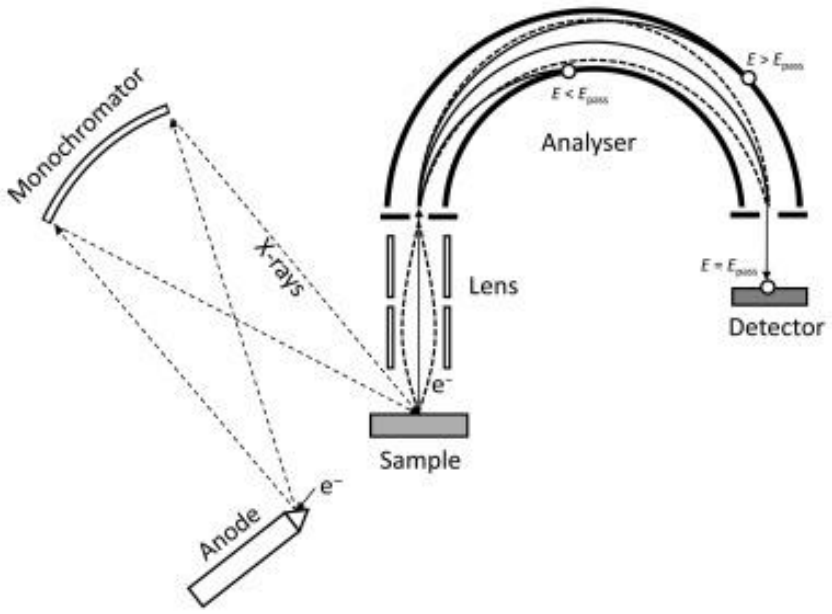

Fig. 2.10. Schematic of a typical photoelectron spectrometer. Reproduced with permission from Elsevier from reference [35].

In a typical X-ray photoelectron spectrometer as depicted in Fig. 2.10, electrons ejected from the sample are with a range of energies and travel in different directions. They pass through a lens to change their kinetic energy and are focused on the entrance to the analyser. The analyser consists of two concentric hemispheres with the inner hemisphere having a certain positive electric charge compared to the outer hemisphere. Electrons with suitable kinetic energy will travel in a hemisphere along the tunnel and hit the detector. Electrons outside the 'suitable' kinetic energy will strike either the outer or inner hemispheres and will not be detected. The electric field of the analyser can vary to control the kinetic energy of the exiting electrons that are count by the detector. Noted that XPS relies on electrons leaving

the sample. An electric field will gradually build on the sample surface if the emitted electrons are not replaced, affecting its electrical environment and thus the accuracy of the binding energies measured. Therefore, the charge compensation needs to be restored by an external source: conducting samples can be connected electrically to provide electrons while insulating samples need low energy electrons to introduce to their surface.

XPS is regarded as a surface characterisation technique. The electron ejecting species involved are usually on the top 1-10 nm of the material, depending on the measuring angle. The exact sampling depth is also dependent on the kinetic energy of the escaping electrons (electrons from the atoms at a deeper length need higher kinetic energy to ionise and to be detected), hence changing the X-rays energy (photon) also changes the measuring depth or potentially the measured volume of samples.

A quantitative elemental composition can be determined by CasaXPS, a powerful data processing software for analysing XPS peaks. The rule of thumb to selecting a transition to determine its element compositions is to choose a peak with the largest peak area and that is free from other interfering peaks. The electronic states of a certain element have their specific sensitivities to be excited by the X-rays. Therefore, the peak area of a certain atom at a certain electronic transition then needs to be scaled by relative sensitivity factors (RSF) to obtain its atomic concentration. The best way to compare XPS intensities is by percentage of atomic concentrations, which is a percentage of the intensity to the total intensity of electrons in the measurements. XPS spectra are usually calibrated with C 1s at 285.0 eV to be comparable between different studies.

Other meaningful parameters such as full width at half maximum (FWHM) indicates the chemical state changes and physical influences. For example, a peak broadening may be attributed to a change in the number of chemical bonds, X-ray damaged samples and

differential charging of the surface. Auger lines, satellite peaks and multiple splitting can also be used to identify chemical states.

Even though XPS is straightforward, non-destructive and the data analysis is relatively easy, a disadvantage of XPS is that it cannot detect hydrogen and helium, leading to problems in differentiating acidified materials compared to neutral ones[34].

2.2.7. Ultraviolet photoelectron spectroscopy

Ultraviolet photoelectron spectroscopy (UPS) is the most common technique for measuring the spectrum of electron density of states (DOS), valence band structures and electronic properties. It works on a very similar principle as XPS except for the irradiation source: UPS uses vacuum UV radiation (10-45 eV) instead of soft X-rays. As UPS is using a lower energy photon energy (normally He I with 21.2 eV, or He II with 40.8 eV) than XPS, it only excites the low-binding energy electrons states in valance band instead of core electrons in XPS. In general, UPS has a higher energy resolution (< 0.1 eV) than XPS. However, due to the advances in synchrotron radiation, the distinction between UPS and XPS is becoming less well defined nowadays.

The typical path length of electrons released during UPS is a few angstroms, leading to its high surface sensitivity. Even with the short path length, it is still able to reach the bulk layer in some materials, which could be resolved by angle-resolved UPS.

For semiconductor, as the focused material in this research project, UPS can determine the broad distribution of valence band which provide insights in the material's band structure. UPS can be used to determine the alignment of the valence band maximum (VBM). Together with the bandgap energy which the determination method will be further explained

in *2.5*, one can derive the alignment of the conduction band minimum (CMB) and thus the band structure alignment.

2.3. Diffraction

2.3.1. X-ray diffraction

X-ray diffraction (XRD) is one of the most widely used techniques for characterising nanoscale materials due to its ease and availability. Analysis of a sample by powder XRD provides important information such as crystallite structure, phase identification, atomic spacing, chemical composition, and sometimes, the morphology of crystalline materials, which form the basis of many heterogeneous catalysts[36].

X-rays are considered as waves of electromagnetic radiation. It will be scattered by the regular arrays of atoms in crystal through the interaction with the electrons – electrons become a secondary source of electromagnetic radiation that scatters the incident radiation. The scattering process in XRD is known as elastic scattering. A regular array of electrons produces a regular array of spherical waves from the scattering process. The waves interact destructively in most of the directions, while in some particular direction, they interact constructively. The constructive interference of a monochromatic beam of X-rays scattered at specific angles from the set of lattice planes creates XRD peaks[30].

Bragg's law (Eq. 2.10) relates the incident angle and the d-spacing of the crystal planes.

$$2dsin\theta = n\lambda \qquad (2.10)$$

where d is the spacing between diffracting planes, θ is the incident angle, n is an integer and λ is the beam wavelength. Bragg's equation assumes that incident X-ray beam reflects on the parallel crystal planes indexed in hkl and spaced d. In Bragg's law, X-rays are reflected by the atoms on the plane and reflected X-rays from successive planes interfere

constructively to produce XRD peaks. Constructive interference occurs when the path difference between the reflected X-rays is integer multiples of the wavelength. Bragg's law simplifies the physical phenomena to assume that the incoming X-rays are 'reflected' specularly (mirror-like) from each crystal plane and neglects the fact that the X-rays source is first scattered by the electrons to all directions (then the waves subsequently interfere constructively in certain directions to give XRD signals); Bragg's law is generally adequate to solve the d-spacing for the crystals. Fig. 2.11 demonstrates the schematic of Bragg's law.

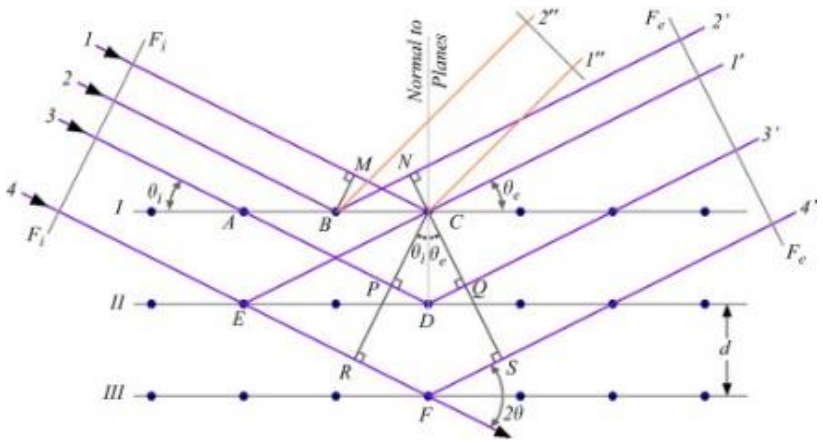

Fig. 2.11. Schematic of X-rays scattering by atoms and the formation of a diffraction pattern. Reproduced with permission from Elsevier from reference [37].

XRD analysis is usually done with an X-ray source of Cu Kα radiation (λ = 1.5418 Å). X-rays are generated by a cathode ray tube and filtered to produce monochromatic radiation and then directed to the sample. The resulting scattered X-rays are detected over a range of angles (recorded as 2θ on XRD pattern) by rotating the detector position relative to the X-ray source and the sample.

The identity of the atoms and the atomic positions within the lattice planes determine the XRD peak intensities and positions. Each material has a unique set of d-spacings. Therefore, it is a fingerprint of the periodic atomic arrangements of materials. Detailed crystal structure

information, such as unit cell dimensions, bond-lengths, bond-angles, and site-ordering information can be obtained. Furthermore, a standard database for X-ray powder diffraction patterns enable quick phase identification for a crystalline sample[38]. Furthermore, XRD can easily measure the change in d-spacing. Structural changes induced in a crystalline material by blending with other materials can be rapidly monitored with XRD[39].

Albeit the availability of XRD and its power in providing information on unit cell dimension, it cannot provide local structural information, such as amorphous materials, mixed materials, or multiphasic compounds. XRD is a bulk technique; the information from XRD are average values over the whole bulk material[40]. Also, homogenous and signal phase material is required to have good data quality. It is also complicated to index an unknown unit cell if its standard reference file is not present.

2.4. Electrochemical analysis

2.4.1. Zeta potential

Zeta potential is the charge that develops at the interface between a charged particle surface and its liquid medium. In a colloidal system, dispersed charged particles will affect the ion distribution in the near medium region. An electrical double layer is formed in that region of the particle-liquid interface. This double layer consists of two parts: (1) an inner region called Stern layer, which includes ions bound relatively tightly to the surface, and (2) an outer region called diffuse layer, where ions are loosely bound due to the electrostatic forces and the random thermal motion of the ion in the medium. The potential in the diffuse layer region decays with increasing distance from the surface until, at sufficient distance, it reaches the bulk solution value, conventionally taken to be zero. Zeta potential is defined as the electrostatic potential at this particle slipping plane – the outer boundary of the diffuse

layer (Fig. 2.12). In other words, it can be regarded as the potential difference between the dispersion medium and the stationary layer of the fluid attached to the particle layer.

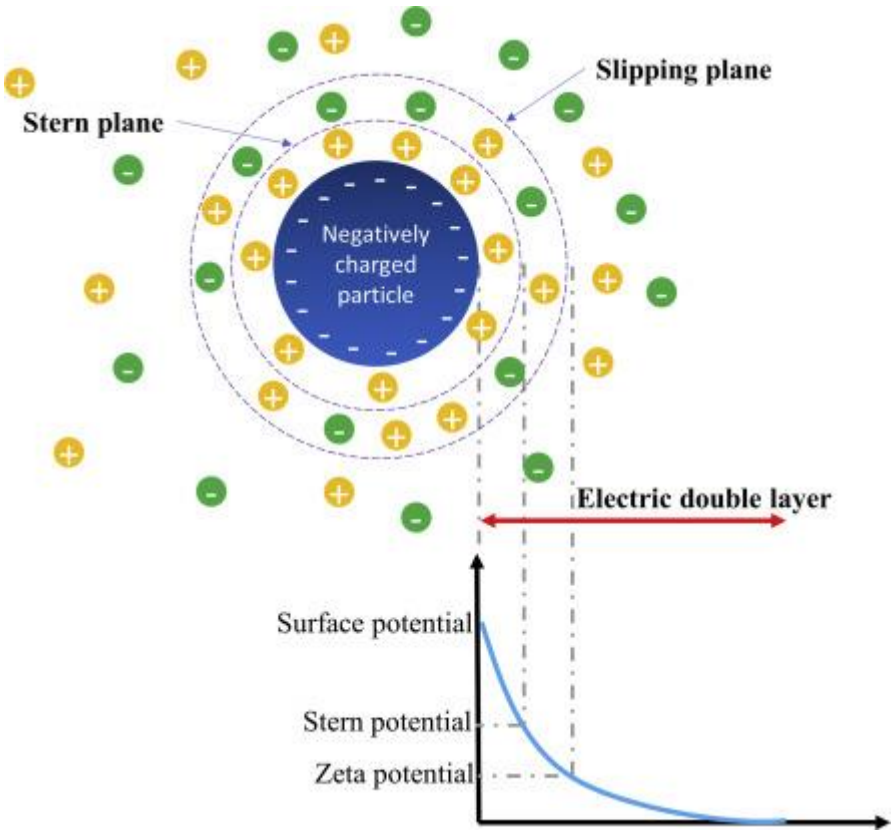

Fig. 2.12. A schematic diagram of an electrical double layer in zeta potential. Reproduced with permission from Elsevier from reference [41].

Zeta potential is a quantitative measure of the effective electric charge on the nanoparticle's surface in a particular medium. For example, a zeta potential of +60 mV has a more positive surface charge than a particle with a zeta potential of +10 mV. As the charged particle has a 'blanket' of counter-ions around it in the liquid, there will be a repulsive force between particles. Colloidal stability is determined by the sum of attractive forces (van der Waals force) and repulsive forces (electrostatic). The stronger the surface charge, the larger the repulsion force and thus the particles are less inclined to aggregate or flocculate due to van der Waals force. In other words, a higher surface charge means higher stability of the

suspensions. Zeta potential is, therefore, also an important parameter to indicate the stability of colloidal particles. In general, zeta potential outside the range of $\pm$ 30 mV is often quoted as a threshold for having sufficient repulsive force to attain better long-term physical colloidal stability.

Charged particles exhibit certain effects under the influence of an applied electric field. These effects are collectively defined as electrokinetic effects and are used for zeta potential measurement. Fundamentally, there are four movements to measure zeta potential: electrophoresis, electro-osmosis, streaming potential, and sedimentation potential. Electrophoresis is the most common movement for the measurement among the four. It is the movement of a charged particle relative to the liquid medium it is suspended in under the influence of an applied electric field.

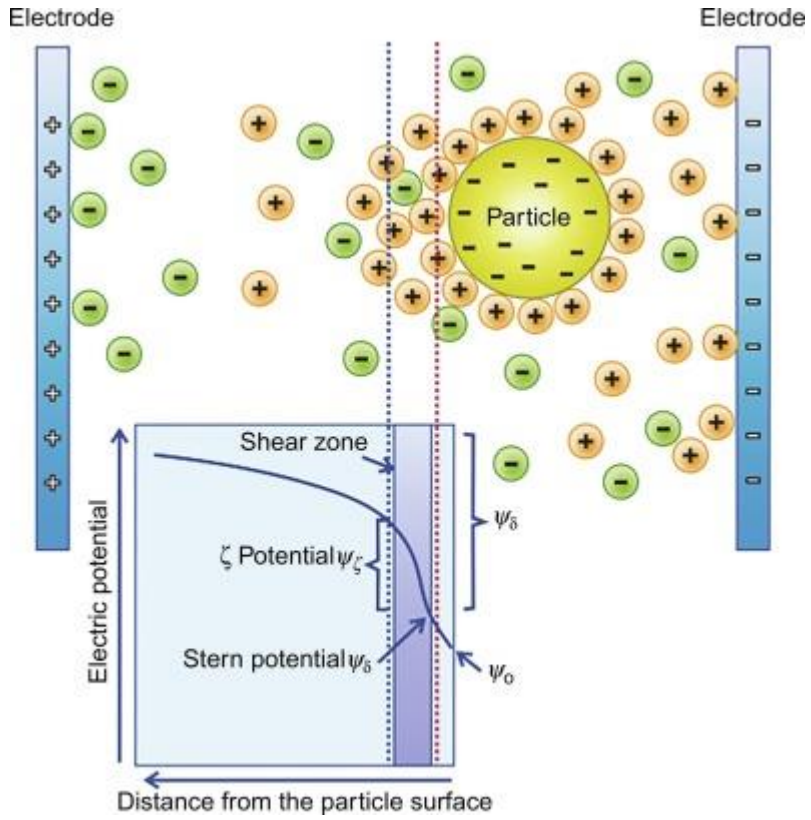

Fig. 2.13. Illustration of zeta potential measurement by electrophoresis method. Reproduced with permission from Elsevier from reference [41].

When a voltage is applied to a suspension solution, charged particles are attracted to the electrode with opposite polarity. The particles and their closely associated ions (fixed Stern layer and diffuse double layer) move through the solution as a unit in the sample cell (Fig. 2.13). Electrophoretic light scattering (ELS) measurements or short video clips are taken when this unit is moving in the medium under the influence of an applied electric field. The particles' electrophoretic mobility and their polarity can be deduced. Electrophoretic mobility can then be related to zeta potential by the Henry equation. The details of the calculations will not be covered here; more information on this topic can be found in the excellent review from Polaczyk *et al.*[42].

Note that a zeta potential value on its own without defining the solution conditions is virtually meaningless. It is only useful when the measurement conditions are known. These factors include the chemistry of both the particle surface and the dispersant, pH, temperature, ionic strength of the medium, as well as the concentration of a formulation component such as polymer and surfactant.

2.5. Band structure determination

Bandgap energy is an important feature of semiconductor materials that determines their activities and potential applications. Therefore, precise determination of bandgap energy is key in understanding a catalyst's properties. In general, the most widely used method is to combine the Tauc method and the optical characterisation techniques (*I.e.* DRS UV-Vis-IR).

The Tauc method is based on the relationship between E_g and the optical absorption coefficient α by Eq. 2.11.

$$\alpha h\nu = C_1\left(h\nu - E_g\right)^n \qquad (2.11)$$

where C_1 is the proportionality constant, $h\nu$ is the energy of the incident photon and n is a coefficient, which is dependent on the kind of electronic transition ($n = \frac{1}{2}$ for direct allowed transition, $n = \frac{3}{2}$ for direct forbidden transition, $n = 2$ for indirect allowed transition, and $n = 3$ for indirect forbidden transitions). The value of E_g is then found at the intersection of the best fit line of the region of the optical absorption edge (*i.e.* the Tauc segment) in the Tauc plot, which is plotted as $(\alpha h\nu)^{\frac{1}{n}}$ *vs* $h\nu$.

α as the optical absorption coefficient is needed for constructing the Tauc plot, and the method is assumed that there is negligible light scattering. However, for powder samples, scattering component is always present, therefore, optical absorption spectroscopy cannot be used to determine E_g. An alternative technique is to use diffuse reflective spectroscopy (DRS) to produce an analogous Tauc plot by Kubelka- Munk or reemission function, $F(R_\infty)$ according to Eq. 2.12 to Eq. 2.14 [43].

$$R_\infty = \frac{R_{sample}}{R_{standard}} \qquad (2.12)$$

$$F(R_\infty) = \frac{K}{S} = \frac{(1-R_\infty)^2}{2R_\infty} \qquad (2.13)$$

$$F(R_\infty)h\nu = C_2\left(h\nu - E_g\right)^n \qquad (2.14)$$

where R_∞ is the reflectance of the sample with 'infinite thickness' and therefore, there is no contribution of the supporting material; K and S are the absorption and scattering K-M coefficients, respectively, and C_2 is a proportionality constant. Practically, samples with a thickness >2 mm are enough to avoid the signal contribution from the sample holder. The value of R_∞ is equal to the ratio of the reflectance of the sample (R_{sample}) and a diffuse reflectance standard material ($R_{standard}$). $BaSO_4$ pallet is used in this research project as the

white standard. The Tauc plot using DRS for solid samples is then plotted as $(F(R_\infty)\ h\nu)^{\frac{1}{n}}$ *vs* $h\nu$. An example of a Tauc plot is illustrated in Fig. 2.14 for linear extrapolation to find the bandgap energy of the material[44].

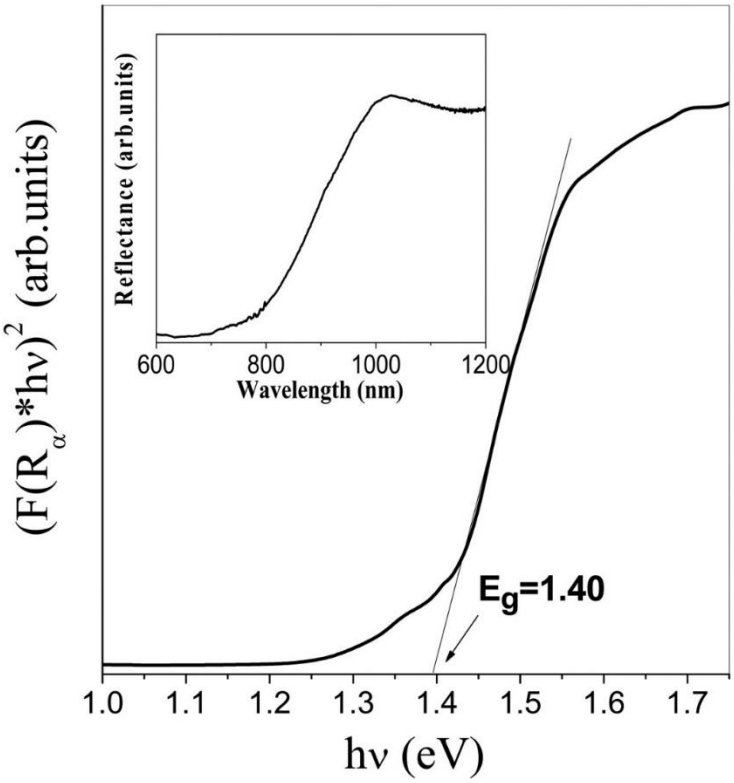

Fig. 2.14. A typical example of Tauc plot, $((F(R_\infty)\ h\nu)^2)$ vs $h\nu$ for estimating the bandgap energy of Cu_3BiS_3 nanoparticles. Reproduced with permission from Elsevier from reference [45].

On the valence region of UPS spectra, the VBM can be obtained by linear extrapolation of the leading edge to the background intensity. One limitation to finding VMB is the valence band edges of the semiconductor must be detectable in the UPS range[46]. After obtaining the bandgap energy from the Tauc plot and VBM from UPS, the CBM is just on the energy level above the VBM by the bandgap energy.

2.6. References

1. West, A. R., *Solid state chemistry and its applications*. John Wiley & Sons: 2014.
2. Farré, M.; Barceló, D., Chapter 1 - Introduction to the Analysis and Risk of Nanomaterials in Environmental and Food Samples. In *Comprehensive Analytical Chemistry*, Farré, M.; Barceló, D., Eds. Elsevier: 2012; Vol. 59, pp 1-32.
3. Ramakrishna, B. L.; Ong, E. W., Surface Evaluation by Atomic Force Microscopy. In *Encyclopedia of Materials: Science and Technology*, Buschow, K. H. J.; Cahn, R. W.; Flemings, M. C.; Ilschner, B.; Kramer, E. J.; Mahajan, S.; Veyssière, P., Eds. Elsevier: Oxford, 2001; pp 9030-9036.
4. Sinha Ray, S., 3 - Structure and Morphology Characterization Techniques. In *Clay-Containing Polymer Nanocomposites*, Sinha Ray, S., Ed. Elsevier: Amsterdam, 2013; pp 39-66.
5. Hussain, C. M.; Rawtani, D.; Pandey, G.; Tharmavaram, M., Chapter 14 - Atomic force microscopy for forensic samples. In *Handbook of Analytical Techniques for Forensic Samples*, Hussain, C. M.; Rawtani, D.; Pandey, G.; Tharmavaram, M., Eds. Elsevier: 2021; pp 259-279.
6. Sinha Ray, S., 4 - Techniques for characterizing the structure and properties of polymer nanocomposites. In *Environmentally Friendly Polymer Nanocomposites*, Sinha Ray, S., Ed. Woodhead Publishing: 2013; pp 74-88.
7. Li, F.; Clark, J. V., *Calibrating Stiffness and Displacement of an Atomic Force Microscope using Self-Calibratable Micro-Electro-Mechanical Systems: Theoretical Study*. 2011; p 410-413.
8. Kuwahara, Y.; Uehara, S.; Aoki, Y., Surface microtopography of lath-shaped hydrothermal illite by tapping-mode (TM) and contact-mode AFM. *Clays and Clay Minerals* **1998,** *46* (5), 574-582.
9. Ebnesajjad, S., 4 - Surface and Material Characterization Techniques. In *Surface Treatment of Materials for Adhesion Bonding*, Ebnesajjad, S., Ed. William Andrew Publishing: Norwich, NY, 2006; pp 43-75.
10. Chen, J.; Warner, J. H., Chapter 6 - Atomic structure of defects in transitional metal dichalcogenides using transmission electron microscopy. In *2D Semiconductor Materials and Devices*, Chi, D.; Goh, K. E. J.; Wee, A. T. S., Eds. Elsevier: 2020; pp 167-197.
11. Klein, N. D.; Hurley, K. R.; Feng, Z. V.; Haynes, C. L., Dark Field Transmission Electron Microscopy as a Tool for Identifying Inorganic Nanoparticles in Biological Matrices. *Analytical Chemistry* **2015,** *87* (8), 4356-4362.
12. Tomoda, B. T.; Yassue-Cordeiro, P. H.; Ernesto, J. V.; Lopes, P. S.; Péres, L. O.; da Silva, C. F.; de Moraes, M. A., Chapter 3 - Characterization of biopolymer membranes and films: Physicochemical, mechanical, barrier, and biological properties. In *Biopolymer Membranes and Films*, de Moraes, M. A.; da Silva, C. F.; Vieira, R. S., Eds. Elsevier: 2020; pp 67-95.
13. Hodoroaba, V.-D., Chapter 4.4 - Energy-dispersive X-ray spectroscopy (EDS). In *Characterization of Nanoparticles*, Hodoroaba, V.-D.; Unger, W. E. S.; Shard, A. G., Eds. Elsevier: 2020; pp 397-417.
14. Harada, Y.; Ikuhara, Y., Chapter 1.1.1 - The Latest Analytical Electron Microscope and its Application to Ceramics. In *Handbook of Advanced Ceramics (Second Edition)*, Somiya, S., Ed. Academic Press: Oxford, 2013; pp 3-21.
15. Wolfgong, W. J., Chapter 14 - Chemical analysis techniques for failure analysis: Part 1, common instrumental methods. In *Handbook of Materials Failure Analysis with Case Studies from the Aerospace and Automotive Industries*, Makhlouf, A. S. H.; Aliofkhazraei, M., Eds. Butterworth-Heinemann: Boston, 2016; pp 279-307.
16. Nasrazadani, S.; Hassani, S., Chapter 2 - Modern analytical techniques in failure analysis of aerospace, chemical, and oil and gas industries. In *Handbook of Materials Failure Analysis with Case Studies from the Oil and Gas Industry*, Makhlouf, A. S. H.; Aliofkhazraei, M., Eds. Butterworth-Heinemann: 2016; pp 39-54.

17. Rowlands, C. C.; Murphy, D. M., Chemical Applications of EPR. In *Encyclopedia of Spectroscopy and Spectrometry*, Lindon, J. C., Ed. Elsevier: Oxford, 1999; pp 190-198.
18. Hagen, W. R., Chapter 4 - EPR spectroscopy. In *Practical Approaches to Biological Inorganic Chemistry (Second Edition)*, Crichton, R. R.; Louro, R. O., Eds. Elsevier: 2020; pp 121-154.
19. Hruszowiec, M.; Nowak, K.; Szlachetko, B.; Grzelczak, M.; Czarczyński, W.; Pliński, E. F.; Więckowski, T., The Microwave Sources for EPR Spectroscopy. *Journal of Telecommunications and Information Technology* **2017**.
20. Roessler, M. M.; Salvadori, E., Principles and applications of EPR spectroscopy in the chemical sciences. *Chemical Society Reviews* **2018,** *47* (8), 2534-2553.
21. Karunakaran, C.; Balamurugan, M., Chapter Four - Electron Paramagnetic Resonance Spectroscopy. In *Spin Resonance Spectroscopy*, Karunakaran, C., Ed. Elsevier: 2018; pp 169-228.
22. John, N.; George, S., Chapter 5 - Raman Spectroscopy. In *Spectroscopic Methods for Nanomaterials Characterization*, Thomas, S.; Thomas, R.; Zachariah, A. K.; Mishra, R. K., Eds. Elsevier: 2017; pp 95-127.
23. Stevenson, C. L.; Vo-Dinh, T., Signal expressions in Raman spectroscopy. *Modern Techniques in Raman Spectroscopy* **1996**, 1-39.
24. Strak, P.; Koronski, K.; Sakowski, K.; Sobczak, K.; Borysiuk, J.; Korona, K. P.; Dróżdż, P. A.; Grzanka, E.; Sarzynski, M.; Suchocki, A.; Monroy, E.; Krukowski, S.; Kaminska, A., Instantaneous decay rate analysis of time resolved photoluminescence (TRPL): Application to nitrides and nitride structures. *Journal of Alloys and Compounds* **2020,** *823*, 153791.
25. Nuttall, L. Scanning micro-photoluminescence studies of GaAs photonic crystals and perovskite structures. University of Oxford, 2019.
26. Robinson, J. W. Time-integrated and time-resolved optical studies of InGaN quantum dots. 2005.
27. Kafle, B. P., Chapter 2 - Theory and instrumentation of absorption spectroscopy: UV–VIS spectrophotometry and colorimetry. In *Chemical Analysis and Material Characterization by Spectrophotometry*, Kafle, B. P., Ed. Elsevier: 2020; pp 17-38.
28. Mujahid, A.; Dickert, F. L., Chapter 6 - Molecularly Imprinted Polymers for Sensors: Comparison of Optical and Mass-Sensitive Detection. In *Molecularly Imprinted Sensors*, Li, S.; Ge, Y.; Piletsky, S. A.; Lunec, J., Eds. Elsevier: Amsterdam, 2012; pp 125-159.
29. Canton, L. C.; Souza Júnior, I. G. d.; Silva, L. S.; Marques Júnior, J.; Costa, A. C. S. d., Identification and quantification of iron oxides by diffuse reflectance spectroscopy with Praying Mantis accessory and integration sphere. *CATENA* **2021,** *196*, 104899.
30. Holbrook, R. D.; Galyean, A. A.; Gorham, J. M.; Herzing, A.; Pettibone, J., Chapter 2 - Overview of Nanomaterial Characterization and Metrology. In *Frontiers of Nanoscience*, Baalousha, M.; Lead, J. R., Eds. Elsevier: 2015; Vol. 8, pp 47-87.
31. Feiters, M. C.; Meyer-Klaucke, W., Chapter 7 - X-ray absorption and emission spectroscopy in biology. In *Practical Approaches to Biological Inorganic Chemistry (Second Edition)*, Crichton, R. R.; Louro, R. O., Eds. Elsevier: 2020; pp 229-273.
32. Kowalska, J. K.; Lima, F. A.; Pollock, C. J.; Rees, J. A.; DeBeer, S., A Practical Guide to High-resolution X-ray Spectroscopic Measurements and their Applications in Bioinorganic Chemistry. *Israel Journal of Chemistry* **2016,** *56* (9-10), 803-815.
33. Tabuchi, M.; Sakamoto, R.; Takeda, S.; Konishi, S.; Suzuki, T.; Nagami, T., Modified linear combination fitting for large-area two-dimensional chemical state mapping. *Radiation Physics and Chemistry* **2020,** *175*, 108257.
34. Baer, D. R.; Thevuthasan, S., Chapter 16 - Characterization of Thin Films and Coatings. In *Handbook of Deposition Technologies for Films and Coatings (Third Edition)*, Martin, P. M., Ed. William Andrew Publishing: Boston, 2010; pp 749-864.
35. Shard, A. G., Chapter 4.3.1 - X-ray photoelectron spectroscopy. In *Characterization of Nanoparticles*, Hodoroaba, V.-D.; Unger, W. E. S.; Shard, A. G., Eds. Elsevier: 2020; pp 349-371.

36. Holder, C. F.; Schaak, R. E., Tutorial on Powder X-ray Diffraction for Characterizing Nanoscale Materials. *ACS Nano* **2019,** *13* (7), 7359-7365.
37. Saini, B. S.; Kaur, R., 3 - X-ray diffraction. In *Handbook of Modern Coating Technologies*, Aliofkhazraei, M.; Ali, N.; Chipara, M.; Bensaada Laidani, N.; De Hosson, J. T. M., Eds. Elsevier: Amsterdam, 2021; pp 85-141.
38. Chapter 3 - Methods for Assessing Surface Cleanliness. In *Developments in Surface Contamination and Cleaning, Volume 12*, Kohli, R.; Mittal, K. L., Eds. Elsevier: 2019; pp 23-105.
39. Rajeswari, A.; Jackcina Stobel Christy, E.; Gopi, S.; Jayaraj, K.; Pius, A., 9 - Characterization studies of polymer-based composites related to functionalized filler-matrix interface. In *Interfaces in Particle and Fibre Reinforced Composites*, Goh, K. L.; M.K, A.; De Silva, R. T.; Thomas, S., Eds. Woodhead Publishing: 2020; pp 219-250.
40. Hussain, C. M.; Rawtani, D.; Pandey, G.; Tharmavaram, M., Chapter 17 - X-ray diffraction for forensic samples. In *Handbook of Analytical Techniques for Forensic Samples*, Hussain, C. M.; Rawtani, D.; Pandey, G.; Tharmavaram, M., Eds. Elsevier: 2021; pp 321-338.
41. Feng, Y.; Kilker, S. R.; Lee, Y., Chapter Seven - Surface charge (zeta-potential) of nanoencapsulated food ingredients. In *Characterization of Nanoencapsulated Food Ingredients*, Jafari, S. M., Ed. Academic Press: 2020; Vol. 4, pp 213-241.
42. Polaczyk, A. L.; Amburgey, J. E.; Alansari, A.; Poler, J. C.; Propato, M.; Hill, V. R., Calculation and uncertainty of zeta potentials of microorganisms in a 1:1 electrolyte with a conductivity similar to surface water. *Colloids and Surfaces A: Physicochemical and Engineering Aspects* **2020,** *586*, 124097.
43. Morales, A. E.; Mora, E. S.; Pal, U., Use of diffuse reflectance spectroscopy for optical characterization of un-supported nanostructures. *Revista mexicana de física* **2007,** *53* (5), 18-22.
44. Escobedo-Morales, A.; Ruiz-López, I. I.; Ruiz-Peralta, M. d.; Tepech-Carrillo, L.; Sánchez-Cantú, M.; Moreno-Orea, J. E., Automated method for the determination of the band gap energy of pure and mixed powder samples using diffuse reflectance spectroscopy. *Heliyon* **2019,** *5* (4), e01505.
45. Morales-Gallardo, M. V.; Pascoe-Sussoni, J. E.; Delesma, C.; Mathew, X.; Paraguay-Delgado, F.; Muñiz, J.; Mathews, N. R., Surfactant free solvothermal synthesis of Cu3BiS3 nanoparticles and the study of band alignments with n-type window layers for applications in solar cells: Experimental and theoretical approach. *Journal of Alloys and Compounds* **2021,** *866*, 158447.
46. Carlson, B.; Leschkies, K.; Aydil, E. S.; Zhu, X. Y., Valence Band Alignment at Cadmium Selenide Quantum Dot and Zinc Oxide $(10\bar{1}0)$ Interfaces. *The Journal of Physical Chemistry C* **2008,** *112* (22), 8419-8423.

Chapter 3: Experimental methods

3.1. Materials

In_2Se_3 (99.99%, metal basis, Alfa Aesar); MoS_2 powder (reagent grade, Sigma-Aldrich); n-butyllithium (1.6 M in hexanes, reagent grade, Sigma-Aldrich); Hexane (≥95%, HPLC, Sigma-Aldrich); Isopropanol (99.9%, Sigma-Aldrich); Hydrochloric acid (ACS reagent, 37%, Sigma-Aldrich); Ruthenium(III) acetylacetonate (reagent grade, Sigma-Aldrich); Chloroplatinic acid solution (8 wt.% in H_2O, Sigma-Aldrich); Palladium(II) chloride (99%, powder, Sigma-Aldrich); Nickel chloride hexahydrate (reagent grade, Sigma-Aldrich); Iron(III) chloride (≥99.99%, anhydrous powder, trace metals basis); Cobalt nitrate hexahydrate (≥98%, reagent grade, Sigma-Aldrich); Rhodium(III) chloride hydrate (99.98%, trace metals basis, Sigma-Aldrich); Gold(III) chloride trihydrate (≥99.9%, trace metals basis, Sigma-Aldrich); Silver nitrate (ACS reagent, ≥99.0%, Sigma-Aldrich); Thiourea (≥99.0%, ACS reagent, Sigma-Aldrich); Polyvinylpyrrolidone (PVP, average mol wt. 40,000, reagent grade, Sigma-Aldrich); Sodium hydroxide (≥97.0%, pellets, ACS reagent, Sigma-Aldrich); Argon gas (99.99%, BOC); Helium gas (99.99%, BOC); Nitrogen gas (99.99%, BOC).

3.2. Methods

3.2.1. Synthesis of 2D-In_2Se_3

The method of synthesizing 2D-In_2Se_3 is developed adapted from the previous work on the synthesis of monolayer MoS_2 in Professor Edman Tsang's group[1-3]. 2D-In_2Se_3 is prepared with the standard lithium intercalation method alongside with Mr Wentian Niu for the first few batches of samples. Bulk-In_2Se_3 (2.00 g) was vigorously stirred in 16 mL of 1.6 M n-butyllithium/hexane under a nitrogen atmosphere for 72 hours. After washing with hexane to remove the unreacted n-butyllithium, the lithiated In_2Se_3 ($Li_xIn_2Se_3$) was separated by centrifugation and followed by drying *in vacuo* at 343 K. The solid was then immersed into 250 mL of water and sonicated for 6 hours (with a power output of 35 W and an operating

frequency at 37 kHz, Elma Schmidbauer, Germany). The suspension was then centrifuged at 5000 rpm for 15 minutes to remove the unexfoliated precursors and only the supernatant was collected. HCl (37%) was then added dropwise to the collected supernatant until precipitates were formed at a pH of around 7. The solid was separated by centrifugation at 5000 rpm for 15 minutes and the exfoliated 2D-In_2Se_3 was obtained after drying *in vacuo* overnight at 343 K. The exfoliation method is illustrated in Fig. 3.1.

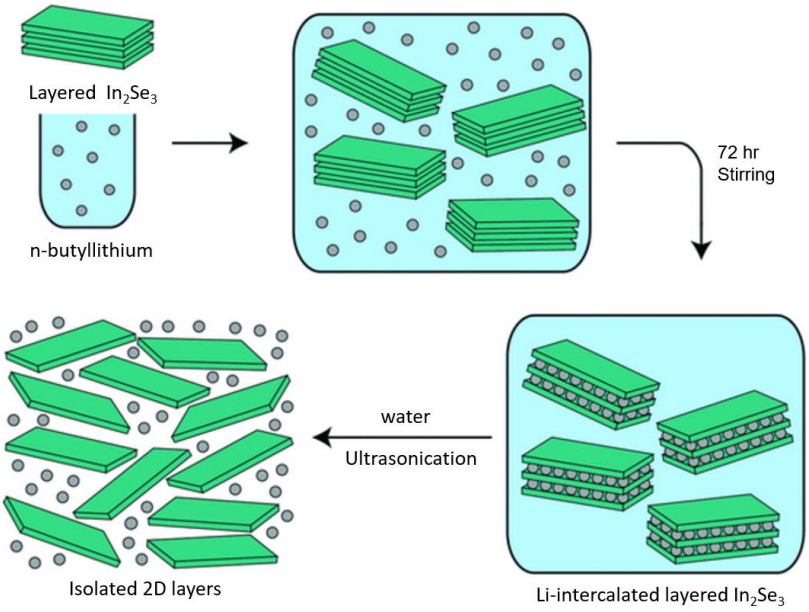

Fig. 3.1. Schematic illustration of the lithium intercalation method for exfoliating Bulk-In_2Se_3 to 2D-In_2Se_3. Reproduced with permission from Elsevier from reference [4].

3.2.2. Synthesis of 2D-MoS_2

2D-MoS_2 was prepared based on the previous report in Tsang group[2-1-3], which highly resembles the method of 2D-In_2Se_3 synthesis in *3.2.1*. 2D-MoS_2 is prepared with the standard lithium intercalation method. Bulk-MoS_2 (2.00 g) was vigorously stirred in 16 mL of 1.6 M n-butyllithium/hexane under a nitrogen atmosphere for 48 hours. After washing with hexane to remove the unreacted n-butyllithium, the lithiated MoS_2 (Li_xMoS_2) was separated by centrifugation and followed by drying *in vacuo* at 343 K. The solid was then

immersed into 250 mL of water and sonicated for 6 hours. The suspension was then centrifuged at 5000 rpm for 15 minutes to remove the unexfoliated precursors and only the supernatant was collected. HCl (37%) was then added dropwise to the collected supernatant until precipitates are formed at a pH of around 7. The solid was separated by centrifugation at 5000 rpm for 15 minutes and the exfoliated 2D-MoS_2 was obtained after drying *in vacuo* overnight at 343 K.

3.2.3. Synthesis of metal-doped 2D-In_2Se_3

3.2.3.1. Hydrothermal synthesis

Ru, Pt, Pd, Ni, Fe and Co-doped 2D-In_2Se_3 were prepared using a hydrothermal method. The metal precursor solution was prepared by dissolving a certain amount (5 wt.% of 2D-In_2Se_3 loading amount) of water-soluble metal precursor and 75.0 mg of thiourea to 10 mL of deionised water. The solution was left overnight to ensure the complete formation of the metal-thiourea complex. This is used as a source of metal for the reaction with 2D-In_2Se_3 in the hydrothermal conditions, yielding the metal-doped 2D-In_2Se_3 (denoted as M-In_2Se_3). For example, $Co(thiourea)_4^{2+}$ was synthesised with cobalt acetate and thiourea, it is used as a source of Co for the hydrothermal doping[1].

The 2D-In_2Se_3 colloidal solution was prepared by dispersing 100 mg of In_2Se_3 and 50 mg of polyvinylpyrrolidone (PVP) into 50 mL of water/isopropanol (3:1, v/v) solution. PVP was added as a capping agent to coat the metal particles, so as to prevent the excessive growth and aggregation of these particles[5]. The colloid solution was sonicated for 1.5 hours and was added to the prepared metal precursor solution. The mixture was then further sonicated for 10 minutes and followed by hydrothermal treatment at 453 K for 24 hours. After the reaction, the obtained solid was separated by centrifugation and was washed with deionised water for three times. The solid was finally treated with a 5% hydrogen (with 95%

N_2) flow in a tubular furnace at 573 K for 2 hours to reduce any oxidised metal during the hydrothermal process.

3.2.3.2. Sonochemical synthesis

Ru, Rh, Pd, Au, Ag and Pt-doped 2D-In_2Se_3 were prepared using the sonochemical doping method. This is used as an alternative doping method because some metals, especially Au and Ag aggregate easily under the condition of hydrothermal treatment even after the addition of PVP as a capping agent. The use of hydrothermal reactions inside an autoclave might also compromise the integrity of the 2D-In_2Se_3 nanostructure[3]. Therefore, we employed the two doping methods and find the M-In_2Se_3 with the best activity.

The procedures of the sonochemical and hydrothermal method were analogous until the step of the hydrothermal treatment. The 2D-In_2Se_3 colloidal solution was prepared by dispersing 100 mg of In_2Se_3 and 50 mg of polyvinylpyrrolidone (PVP) into 50 mL of water/isopropanol (3:1, v/v) solution. PVP was added as a capping agent to coat the metal particles. The colloid solution was sonicated for 1.5 hours and was added to the prepared metal precursor solution. Instead of hydrothermal treatment, the mixture was placed into the sonication tank at room temperature for 24 hours (sonicate for 8 hours per day, for 3 days) to allow the uptake of the metal precursors to 2D-In_2Se_3 during energetic sonication. The solid was washed with deionised water for three times and dried *in vacuo* at 343 K to obtain the product.

3.2.4. Construction of In_2Se_3/MoS_2 heterojunction

Five MoS_2/In_2Se_3 heterojunction samples were prepared with different weight ratios: 9:1, 3:1, 1:1, 1:3 and 1:9. A wide range of ratio was selected for the heterojunction synthesis because it was unclear whether In_2Se_3 or MoS_2 is the smaller flakes that sit on top of one another and form a heterojunction structure with the best photocatalytic activity in the series.

The heterojunction was fabricated through a facile electrostatic self-assembly approach[6]. The as-prepared 2D-MoS_2 (250 mg) was added to aqueous HCl solution (100 mL, 1.5 M) and sonicated for 1 hour, followed by vigorous stirring for 4 hours for further protonation. The resulting acidified suspension was separated by centrifugation at 5000 rpm for 15 minutes and is washed with deionised water until neutral to remove superfluous HCl. The acidified 2D-MoS_2 was redispersed into 100 mL of deionised water. According to the weight ratio, a certain amount of 2D-In_2Se_3 was added. The mixture was sonicated for 30 minutes and then stirred vigorously for another 4 hours. The resulting product was centrifuged at 5000 rpm for 15 minutes and was dried *in vacuo* overnight at 343 K.

3.3. Evaluation of photocatalytic performance

The photocatalytic activity was mainly determined by the hydrogen evolution rate (μmol h^{-1} g^{-1}) from the water splitting, as H_2 is the focused green renewable energy source. The methodology of the testing is derived from the work from Li *et al.*[7]. Reactions were carried out in a closed 25 mL stainless steel autoclave system (Parr, United States) equipped with two quartz windows (with a diameter of 10 mm and a thickness of 18 mm). Blank experiments reveal that no hydrogen was produced without catalyst and light irradiation under detection limit. In a typical activity test, 10 mg of catalyst was added to 8 mL Milli-Q H_2O in a quartz lining (20 mm i.d. × 24 mm o.d. × 52 mm height), then the autoclave was purged with 6 bar of Ar (for hydrogen evolution testing) or He (for oxygen evolution testing) gas as the inert gas after being tightly sealed. The purge was repeated until the air inside the autoclave is fully removed. The mixture in the reactor would then be allowed to heat up to 543 K under vigorous magnetic stirring (750 rpm). Xenon lamp (300 W, Industrial Grade Arc Lamp with Dual Plano-Convex Lens, Fused Silica, Ozone-free, Newport) was then used to shine through the quartz windows at 10 cm distance to provide the irradiation

for water splitting after the autoclave reached 543 K. In Fig. 3.2, the 300 W Xenon arc lamp shows a relatively smooth emission curve in the UV-Vis spectrums, with characteristics wavelengths emitted from 750-1000 nm. The irradiation provides emissions ranged from near-infrared, visible-light, and UV light. After 2 hours reaction, the autoclave was cooled down naturally to room temperature. The content of hydrogen or oxygen was measured by gas chromatography (GC) equipped with thermal conductivity detectors (TCD) with He or N_2 as the carrier gas, respectively. The calibration curves calculating the amount of hydrogen and oxygen are shown in *Appendix*.

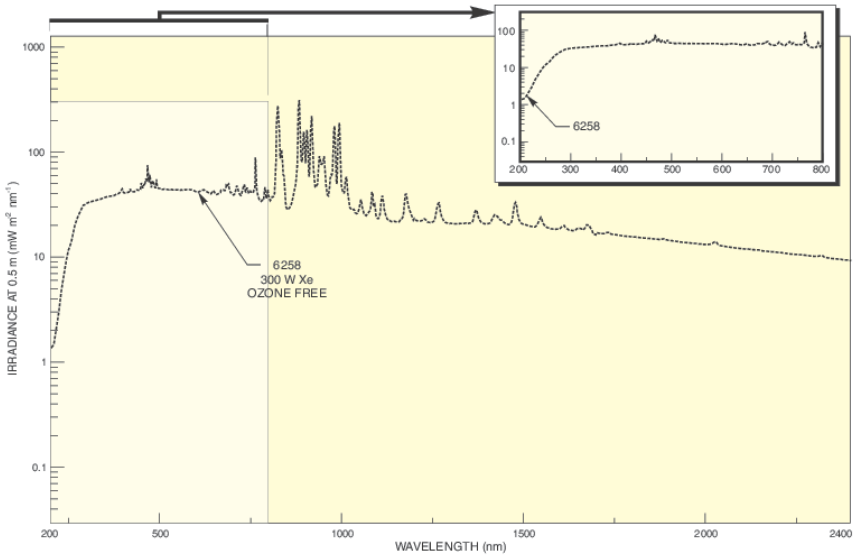

Fig. 3.2. The radiation spectrum of the 300 W Xenon arc lamp used in the experiment. Permission to use granted by Newport Corporation[8]. All rights reserved.

3.4. Photocatalyst characterisation

X-ray diffraction (XRD) measurement was performed using Bruker AXS D8 Advance ECO with LynxEye detector and Copper Kα radiation (λ = 1.5406 Å) with an energy of 8.04 keV. XRD patterns were collected scanning from 5° to 90° with a step size of 0.0195° and a step time of 0.100 s. The measurements were performed at the Department of Chemistry, University of Oxford.

Atomic force microscopy (AFM) was performed by Bruker MM-8 High-resolution AFM with PeakForce Tapping Mode and SNL-10 cantilever, the voltage setpoint was 0.3 V to maintain constant height accuracy. The sample was dispersed in isopropanol and sonicated for 3 hours. Then, the solution was centrifuged at 1500 rpm for 5 minutes to remove large particles. The suspension (2.5 μL) was drop-casted on ultra-flat mica and dried at room temperature. The measurements were performed in the Department of Applied Biology and Chemical Technology, Hong Kong Polytechnic University.

Bright-field imaging and STEM-EDX mapping data were collected by JEOL-2100 LaB6 Transmission Electron Microscope under 200 kV which is equipped with the Oxford instrument 80 mm thin window EDS detector and the Gatan Orius CCD camera. The catalyst suspensions were prepared by dispersing 1 mg of sample in approximately 1 mL of dry ethanol. The mixture was sonicated for 30 minutes to form a uniform suspension. The thin-film sample for TEM (less than 200 nm thick) was then prepared by the deposition of one drop of the as-prepared catalysis suspension onto a Holey carbon film 400 copper mesh grid and dried in the air prior to analysis. Finally, the copper sample grid was transferred to the sample holder of the TEM for measurements. The imaging was performed in the David Cockayne Centre for Electron Microscopy and related facilities at the Department of Materials, University of Oxford.

Scanning transmission electron microscopy (STEM) were performed using FEI Titan G2 60-300 as an SEM or TEM with two aberration correctors. The operating conditions for sample imaging were the accelerating voltage of 300 kV, an electron beam current of 50 pA, and an angular range of 79.5-200.0 mrad for the high-angle annular dark-field (HAADF) imaging detector. The size of each image is 2048×2048 pixels, and the acquiring dwell time per pixel is 6 μs. The microscopy was performed in the Department of Applied Physics, Hong Kong Polytechnic University.

X-ray photoelectron spectroscopy (XPS) was performed using a Kratos Axis SUPRA XPS fitted with a monochromated Al kα X-ray source (1486.7 eV), a spherical sector analyser and 3 multichannel resistive plates, 128 channel delay line detectors. All data was recorded at 150W and a spot size of 700 × 300 μm. Survey scans were recorded at pass energy of 160 eV, and high-resolution scans were recorded at pass energy of 20 eV. Electronic charge neutralization was achieved using a magnetic immersion lens. Filament current = 0.27 A, charge balance = 3.3 V, filament bias = 3.8 V. All sample data was recorded at a pressure below 10^{-8} Torr and a room temperature of 294 K. Data was analysed using CasaXPS v2.3.20PR1.0 and the spectra were calibrated with C 1s peak at 284.8 eV. The deconvolution of the peaks was done using Gaussian-Lorentzian curves and a Shirley type background line. The squared difference between experimental and fitting curves was minimised by least-squares. The measurements were performed in HarwellXPS facilities, UK.

Ultraviolet photoelectron spectroscopy (UPS) was performed with He I at the energy of 21.2 eV. The measurements were performed in HarwellXPS facilities, UK.

Ultraviolet-visible diffuse reflectance spectroscopy (UV-Vis DRS) was performed using Shimadzu UV-2600 under diffuse reflectance mode. Barium sulfate pallet was used as the

white diffuse standard. The data were collected from the Department of Chemistry, University of Oxford.

Time-resolved photoluminescence (TRPL) spectroscopy was performed to measure the photoluminescence spectra and corresponding exciton lifetimes. A bespoke micro photoluminescence setup was used, in which a Ti-Sapphire laser (λ = 375 nm, pulse duration = 150 fs, repetition rate = 76 MHz) was directed onto the sample. Time-resolved measurements were performed using the spectrometer as a monochromator before passing the selected signal to a photomultiplier tube (PMT) detector with an instrument response function width of ~150 ps connected to a time-correlated single-photon counting module. The exciton lifetime is obtained by fitting the corresponding background-corrected TRPL spectra with a mono-exponential decay function in the form of Eq. 3.1 or bi-exponential decay function in the form of Eq. 3.2.

$$y = A_1 e^{-x/t_1} + y_0 \qquad (3.1)$$

$$y = A_1 e^{-x/t_1} + A_2 e^{-x/t_2} \qquad (3.2)$$

The average of the two obtained time parameters, t_1 and t_2, was defined as Eq. 3.3.

$$t\ average = \frac{(A_1 t_1)^2 + (A_2 t_2)^2}{A_1 t_1 + A_2 t_2} \qquad (3.3)$$

The $t\ average$ was then treated as the exciton lifetime of the materials. Errors in the fitting were determined using a least square method. The studies were evaluated at the laboratory of Prof. Robert A. Taylor, University of Oxford.

Continuous-wave electron paramagnetic resonance (CW EPR) spectroscopy was performed by an X-band (9.4 GHz) Bruker EMX EPR spectrometer. All EPR experiments were done at 293 K. 10 mg of sample was weighed and put into an EPR tube (0.60 i.d. and

0.84 o.d.). All X-Band spectra were collected over a 300 Gauss field range and 15 scans were adopted for the measurements. The measurements were performed at the Centre for Advanced Electron Spin Resonance (CAESR), Department of Chemistry, University of Oxford.

X-ray absorption spectroscopy (XAS) data were collected on a beamline at the National Synchrotron Radiation Research Center (NSRRC), Taiwan. Se K-edge X-ray absorption spectrum was conducted in transmittance mode at the BL07A XAS beamline at NSRRC. To examine the local environment around Se atoms, X-ray absorption near edge structure (XANES) and extended X-ray absorption fine structure (EXAFS) data were extracted from XAS. The Demeter ATHENA program was used for XAS data analysis to perform background subtraction, normalization, and Fourier transformation, as well as linear combination fitting. The Demeter ARTEMIS program was used to perform the least-squares curve fitting analysis of the EXAFS $\chi(k)$ data to investigate the local neighbouring structure of Se. The XANES curve was calibrated by selenium powder and Bulk-In_2Se_3 as reference. To confirm the reproducibility of the experimental data, 3 scans were performed for each sample. The data groups were then merged by the ATHENA function, which works on the central limit theorem.

Raman spectroscopy was performed using Perkin Elmer Raman Station 400F with a 785 nm laser source. The samples were exposed for 5 or 8 seconds, for four times with 50 mW or 100mW laser power. The charge-coupled device (CCD) was operating at 224 K. The measurements were done at the Department of Chemistry, University of Oxford.

Zeta potential measurement was performed by Malvern Zetasizer Nano ZS. The samples were dispersed in deionised water at pH 7 and at a temperature of 298 K. The Dispersant RI

was 1.330, viscosity is 0.8872 cP and dispersant dielectric constant is 78.5. The measurement was done at the Department of Materials, University of Oxford.

3.5. References

1. Liu, G.; Robertson, A. W.; Li, M. M.-J.; Kuo, W. C. H.; Darby, M. T.; Muhieddine, M. H.; Lin, Y.-C.; Suenaga, K.; Stamatakis, M.; Warner, J. H.; Tsang, S. C. E., MoS2 monolayer catalyst doped with isolated Co atoms for the hydrodeoxygenation reaction. *Nature Chemistry* **2017,** *9* (8), 810-816.
2. Lau, T. H. M.; Lu, X.; Kulhavý, J.; Wu, S.; Lu, L.; Wu, T.-S.; Kato, R.; Foord, J. S.; Soo, Y.-L.; Suenaga, K.; Tsang, S. C. E., Transition metal atom doping of the basal plane of MoS2 monolayer nanosheets for electrochemical hydrogen evolution. *Chemical Science* **2018,** *9* (21), 4769-4776.
3. Lau, T. H. M.; Wu, S.; Kato, R.; Wu, T.-S.; Kulhavý, J.; Mo, J.; Zheng, J.; Foord, J. S.; Soo, Y.-L.; Suenaga, K.; Darby, M. T.; Tsang, S. C. E., Engineering Monolayer 1T-MoS2 into a Bifunctional Electrocatalyst via Sonochemical Doping of Isolated Transition Metal Atoms. *ACS Catalysis* **2019,** *9* (8), 7527-7534.
4. Nguyen, E. P.; Daeneke, T.; Zhuiykov, S.; Kalantar-zadeh, K., Liquid Exfoliation of Layered Transition Metal Dichalcogenides for Biological Applications. *Current Protocols in Chemical Biology* **2016,** *8* (2), 97-108.
5. Phan, C. M.; Nguyen, H. M., Role of Capping Agent in Wet Synthesis of Nanoparticles. *The Journal of Physical Chemistry A* **2017,** *121* (17), 3213-3219.
6. Zhao, D.; Wang, Y.; Dong, C.-L.; Huang, Y.-C.; Chen, J.; Xue, F.; Shen, S.; Guo, L., Boron-doped nitrogen-deficient carbon nitride-based Z-scheme heterostructures for photocatalytic overall water splitting. *Nature Energy* **2021**.
7. Li, Y.; Wu, S.; Zheng, J.; Peng, Y.-K.; Prabhakaran, D.; Taylor, R. A.; Tsang, S. C. E., 2D photocatalysts with tuneable supports for enhanced photocatalytic water splitting. *Materials Today* **2020**.
8. Newport Coporation, https://www.newport.com/f/medium-power-xenon-light-sources, (last accassed 23 Jul 2021).

Chapter 4: Results and discussion

4.1. 2D-In_2Se_3

4.1.1. Characterisations of 2D-In_2Se_3

4.1.1.1. X-ray diffraction

Powder X-ray diffraction is performed to determine the crystalline changes before and after In_2Se_3 exfoliation. Fig. 4.1 illustrates the XRD patterns of the precursor, Bulk-In_2Se_3 and the exfoliated product, 2D-In_2Se_3. Bulk-In_2Se_3 has an obvious crystalline XRD pattern while the XRD pattern of 2D-In_2Se_3 exhibits no significant diffraction peak. It indicates the material lost its crystalline long-range structure after exfoliation. It suggested that the material might be exfoliated to the desirable thin-layered 2D structure or became an amorphous structure. In an amorphous structure, atoms do not possess periodicity and atoms are randomly distributed in 3D space. X-rays beams will be scattered in random directions, leading to a random distribution of intensity across 2-theta. For 2D materials, although atoms are aligning in a certain arrangement, the scatterings of X-rays from the limited number of atoms in the vertical planes of 2D layers might not be enough to give a significant intensity to be detected. Therefore, the XRD patterns of 2D materials are expected to be a flat line with no obvious peaks.

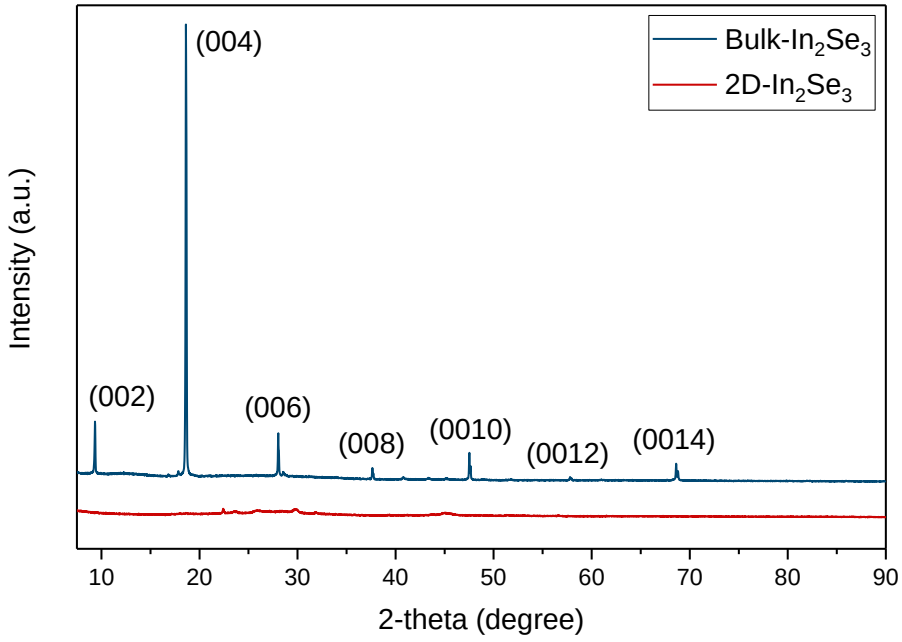

Fig. 4.1. The XRD patterns of Bulk-In_2Se_3 and 2D-In_2Se_3. The XRD was performed at room temperature with ground powder samples. The XRD measurements were performed and analysed by the author at the Department of Chemistry, University of Oxford.

4.1.1.2. Morphology of 2D-In_2Se_3

Transmission electron microscopy (TEM) is used to study the morphologies of the exfoliated 2D-In_2Se_3 structure. Fig. 4.2 shows the irregular shape and size of the exfoliated fractures. The edge of the pieces shows that 2D-In_2Se_3 have a thin sheet-like morphology, implying Bulk-In_2Se_3 was successfully exfoliated to a 2D material. The sheet layers seem to be thicker toward the centre of the fragments on Fig. 4.2 (c), (d) and (e). Apparently, Fig. 4.2 (f) shows a thicker piece compared to the other images such as the flake on Fig. 4.2 (e). It shows chemical exfoliation method cannot precisely control the size and shape and thickness of the 2D-In_2Se_3 synthesised.

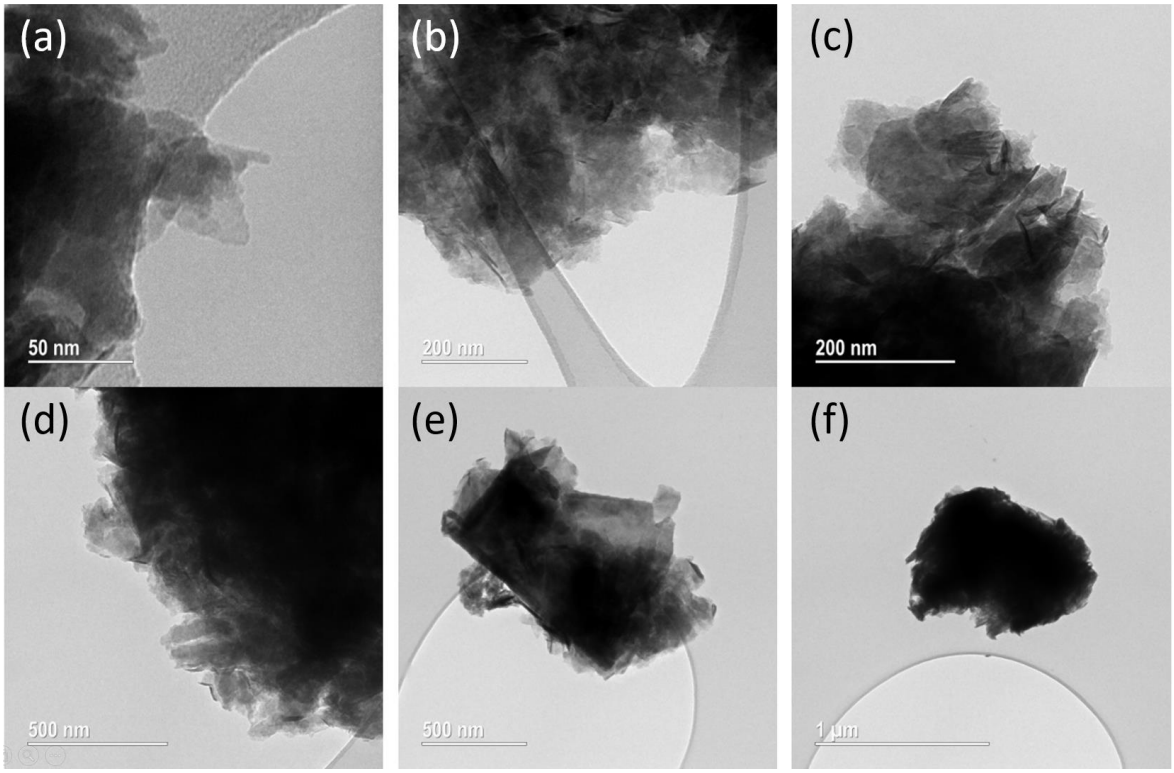

Fig. 4.2. (a-f) Conventional TEM images of 2D-In_2Se_3. The imaging was performed by Mr Ping-Luen (Baron) Ho from Tsang group in the David Cockayne Centre for Electron Microscopy and related facilities at the Department of Materials, University of Oxford. The selection and analysis of the images were performed by the author.

Atomic force microscopy (AFM) was subsequently used to confirm the thickness of individual layers of 2D-In_2Se_3. As shown in Fig. 4.3 (b), the average thickness of the flakes is around 10 nm. Bear in mind that this height profile is done on the edge of the flakes, which is particularly obvious on the green dashed line in Fig. 4.3 (a). The maximum thickness of the flakes is as thick as 40 nm, which is shown as the white patches in Fig. 4.3 (a). It is noted that there is a gradient colour on the background as well as some darker coloured horizontal bars in Fig. 4.3 (a). This is due to the slightly sloped and uneven surface of the mica support. From the AFM height profile, as shown in Fig. 4.3 (b), it can also be seen that the baselines are not ideally flat, which is also associated with the uneven surface of the support. This is

particularly obvious on the green profile that the right-hand side baseline is slightly higher than the one on the left. Such phenomenon is very common in large area scanning AFM, 5 μm × 5 μm in this measurement.

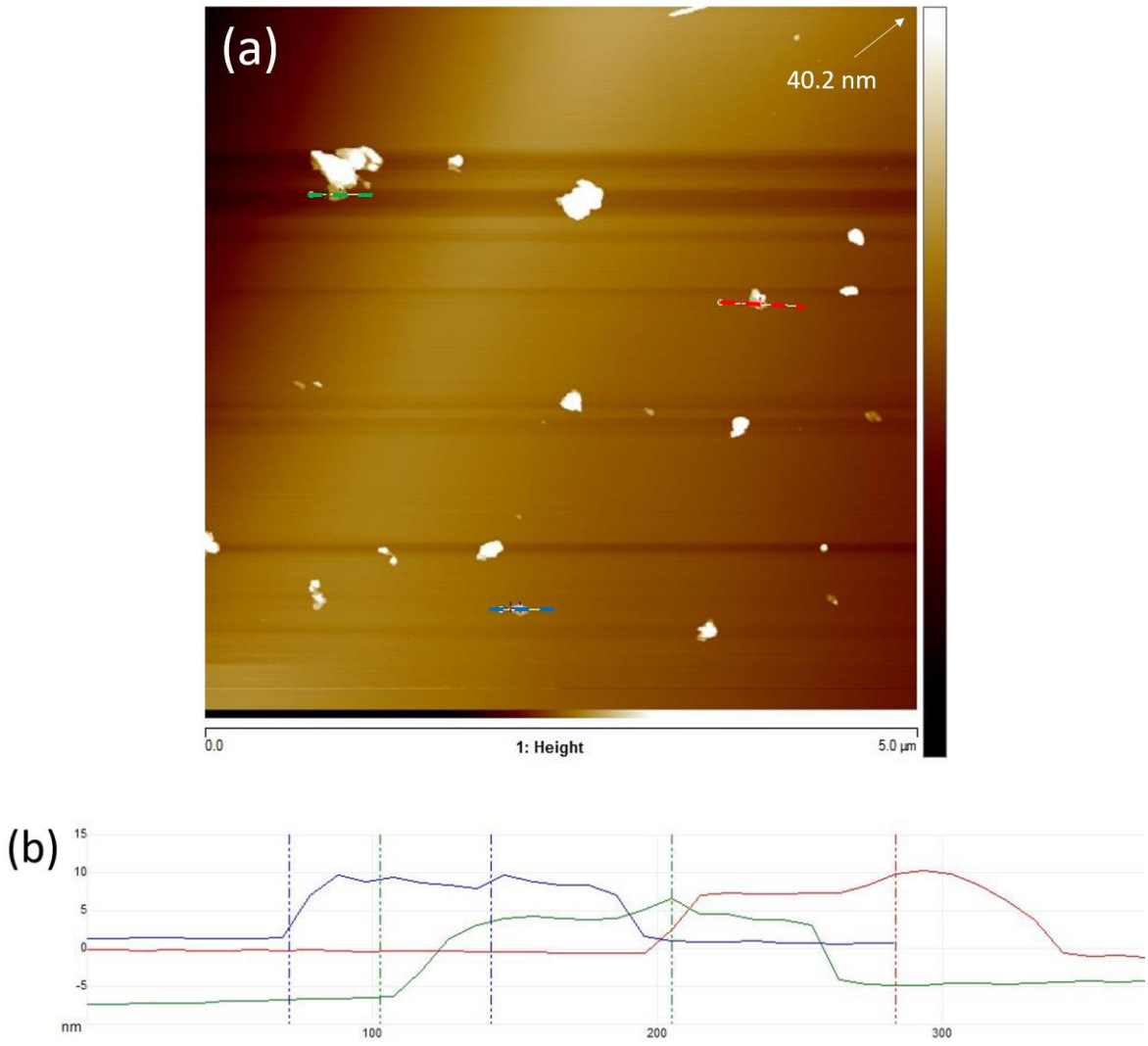

Fig. 4.3. (a) AFM image and (b) the height profile of 2D-In_2Se_3. The blue, red, and green dash lines on the upper image (a) represent the AFM measurements, which their corresponding height profiles are shown on the lower image (b) with the same colour. The AFM measurements were performed by Dr Weiran Zheng in the Department of Applied Biology and Chemical Technology (ABCT), Hong Kong Polytechnic University. The images were selected, adapted, and analysed by the author.

According to the literature, the thickness of monolayer α-In_2Se_3 is 0.9 nm[1]. The thickness of the exfoliated In_2Se_3 nanosheets synthesised by the lithium intercalation method is between 10 nm to 40 nm as demonstrated. Therefore, it corresponds to 10-50 layers of In_2Se_3. It is far from the proposed idea of exfoliating Bulk-In_2Se_3 to mono- or few-layers In_2Se_3. Yet, the exfoliated 10-50 layer In_2Se_3 material is still worth studying since it is much thinner than the bulk material and may exhibit distinct catalytic properties compared to its precursor.

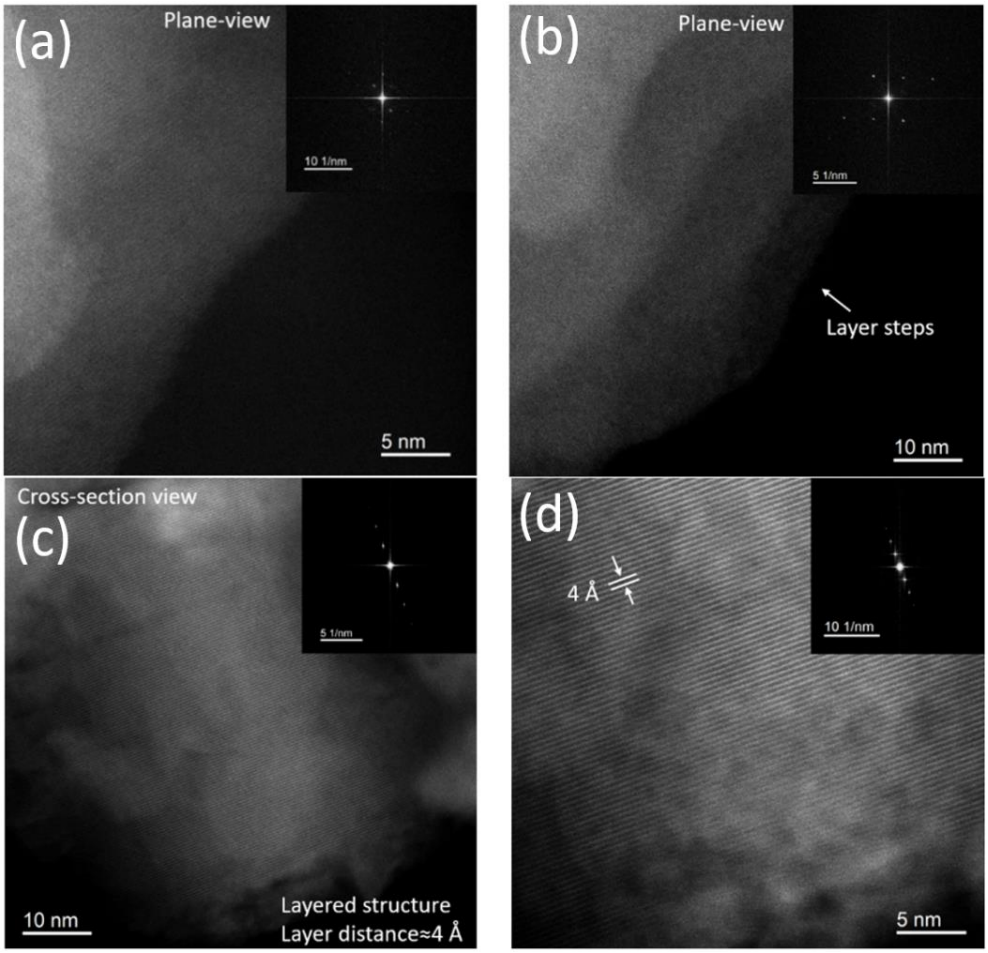

Fig. 4.4. The STEM images of 2D-In_2Se_3. The inset shows the corresponding electron diffraction pattern. (a-b) The STEM images of the plane view of 2D-In_2Se_3. (c-d) The STEM images of the cross-section view of 2D-In_2Se_3. The STEM imaging was performed by Dr Songhua Cai from the Hong Kong Polytechnic University. The images were selected, adapted, and analysed by the author.

The In_2Se_3 morphology is also revealed by the scanning transmission electron microscopy (STEM) image, as shown in Fig. 4.4 (a) and (b), it shows layered steps at the edge of the flakes which agrees with the results of TEM. In Fig. 4.4 (c) and (d), a layered pattern is seen from the STEM images. It is assigned to the lines of selenium atoms on the surface of In_2Se_3 (Fig. 4.5). The distance between the selenium lines is 0.35 nm by the 3R In_2Se_3 crystallographic model under the Cambridge Crystallographic Data Centre (CCDC) entry number 1855522, which further confirms the identity of the layered patterns[2]. The possibility that the STEM layered structure is from the In_2Se_3 quintuple layers is excluded as the distance between two consecutive In_2Se_3 layers is around 0.9 nm instead of 0.4 nm as stated. The lines of atoms appear to be quite well aligned without significant vacancy. It can be concluded that the lithium exfoliation method has mostly preserved the Se surface atomic arrangement of the material.

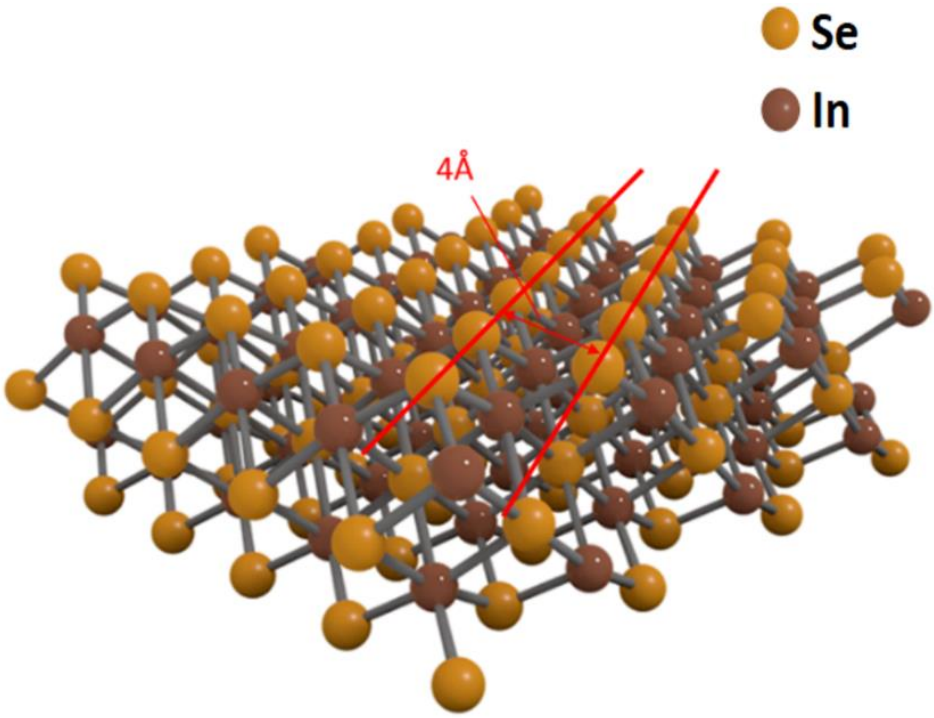

Fig. 4.5. The 3D structural diagram of an In_2Se_3 monolayer. Reproduced with permission from the courtesy of Ossila Limited: Indium (III) Selenide (In_2Se_3) Powder and Crystal[3].

4.1.1.3. X-ray absorption spectroscopy

X-ray absorption spectroscopy (XAS) was used to examine the local electronic structure and coordination environment of 2D-In_2Se_3. In Fig. 4.6 (a) and (b), the XANES spectra at Se K-edge (the main sharp intense peak, or referred to as 'white line' peak, is due to Se 1s → 4p) indicates that the edge energy of 2D-In_2Se_3 (12657.7 eV) is higher than the edge energy of Bulk-In_2Se_3 (Se^{2-}) (12657.4 eV) while lower than that of Se powder (12658.3 eV)[4]. Also, the sharp peak (Se 1s → 4p) of 2D-In_2Se_3 (12657.7 eV) appears to have an intensity between Bulk-In_2Se_3 and Se powder. It might be due to a decreased number of Se^{2-} species and increased number of the unexpected oxidised selenium species (*i.e.* Se^0) in 2D-In_2Se_3, in which the appearance of Se^0 is potentially due to X-ray beam-induced damage. The explanation of the presence of Se^0 will first be discussed by the analysis of XAS data and the justification for beam damage might be the reason of this unexpected appearance will then be examined.

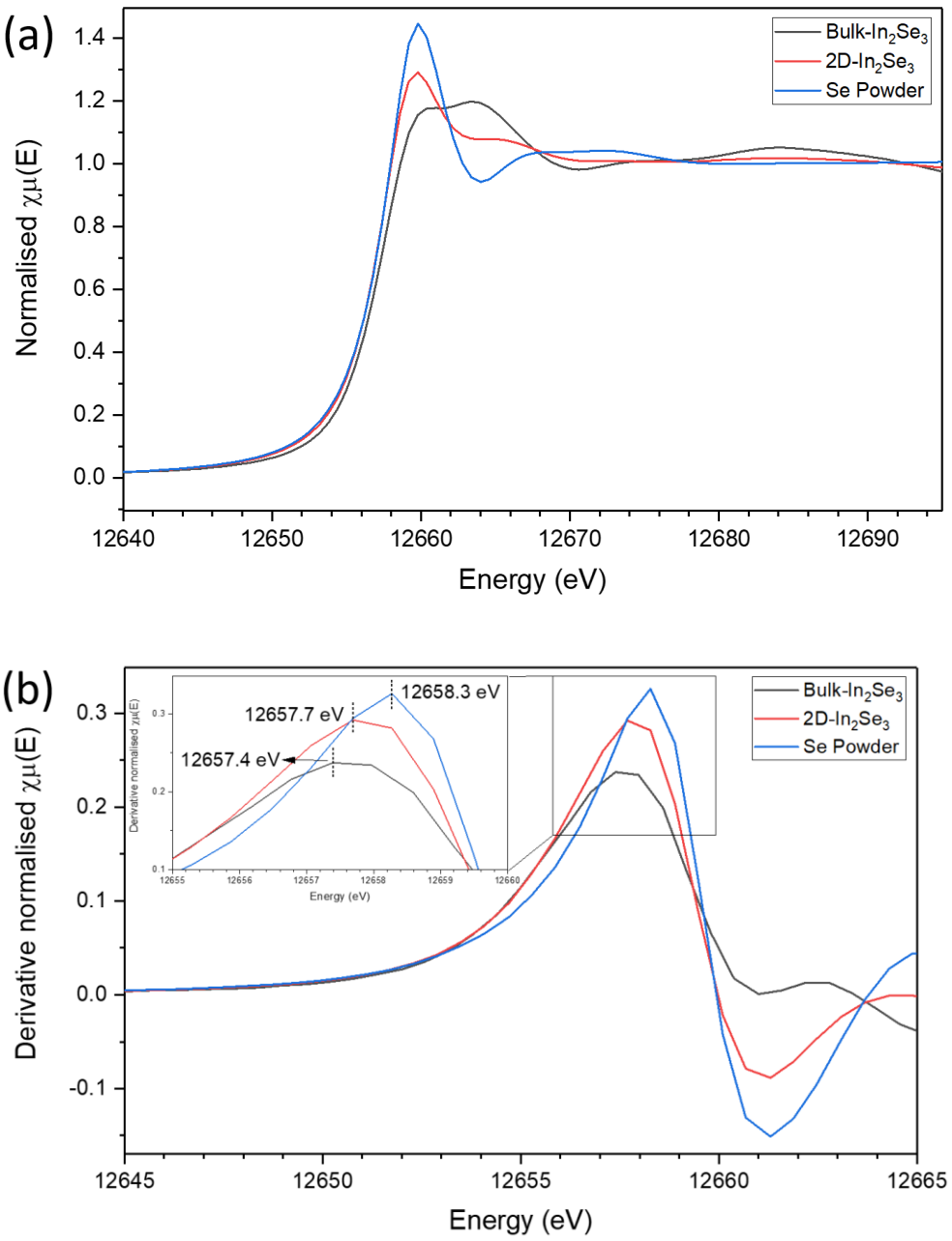

Fig. 4.6. The Se K-edge XANES spectra of 2D-In_2Se_3 with Bulk-In_2Se_3 and Se powder as references. The spectra are shown as (a) normalised $\chi\mu$(E) *vs.* photon energy and (b) first derivative normalised $\chi\mu$(E) *vs.* photon energy. The XAS measurements were performed by Dr Tai-Sing Wu from the National Synchrotron Radiation Research Center (NSRRC), Taiwan. The data analysis and plotting were performed by the author. A special acknowledgement is given to Dr Karen Chan for the XAS result discussions.

The concurrence of Se^{2-} and Se^{0} could be backed by linear combination fitting (LCF) to find the weight ratio of Se^{0} to Se^{2-} in 2D-In_2Se_3.

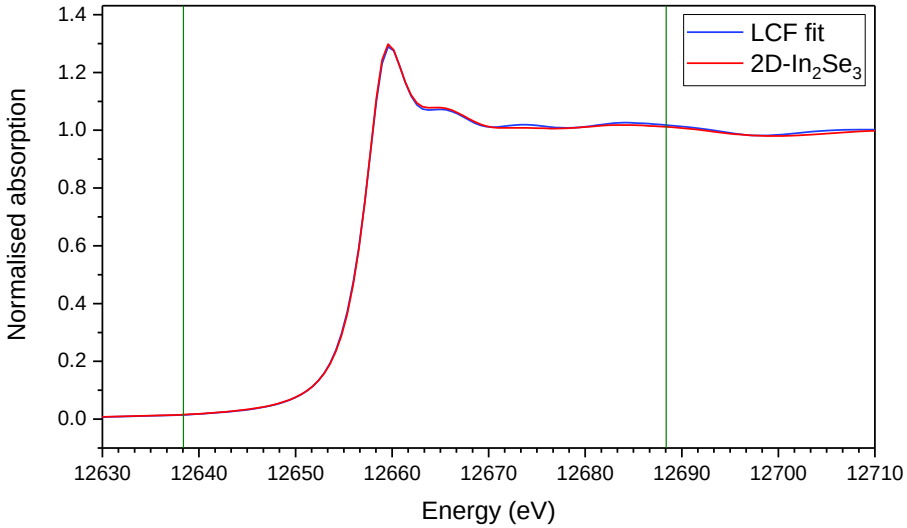

Fig. 4.7. The LCF of 2D-In_2Se_3 with Bulk-In_2Se_3 and Se powder as references. The fitting is done by using normalised μ(E). The LCF data fitting was performed by Mr Wentian Niu from Tsang group. The data analysis and plotting were performed by the author.

Table 4.1. The XANES LCF weighting results of 2D-In_2Se_3 with Bulk-In_2Se_3 and Se powder as the references of Se^{2-} and Se^{0}, respectively.

Standard	**Weight**
Bulk-In_2Se_3	0.499 ± 0.008
Se powder	0.501 ± 0.008

R-factor = 0.0001; χ-square = 0.002; Reduced χ^2 = 0.00003

The LCF results (Fig. 4.7 and Table 4.1) suggested that the weights of Se^{2-} and Se^{0}, with Bulk-In_2Se_3 and Se powder as references, respectively, are nearly in 1:1 ratio. Bulk XAS techniques are measuring the average coordination environment and oxidation state of the probed element[5]. The weights make the average oxidation state of Se in 2D-In_2Se_3 to be Se^{-}.

This deduction agrees with the general trend that an increased in oxidation state (from -2 to -1) will cause an increased edge energy of 2D-In_2Se_3 (Se^-) compared to Bulk-In_2Se_3 (Se^{2-}) in Fig. 4.6[6].

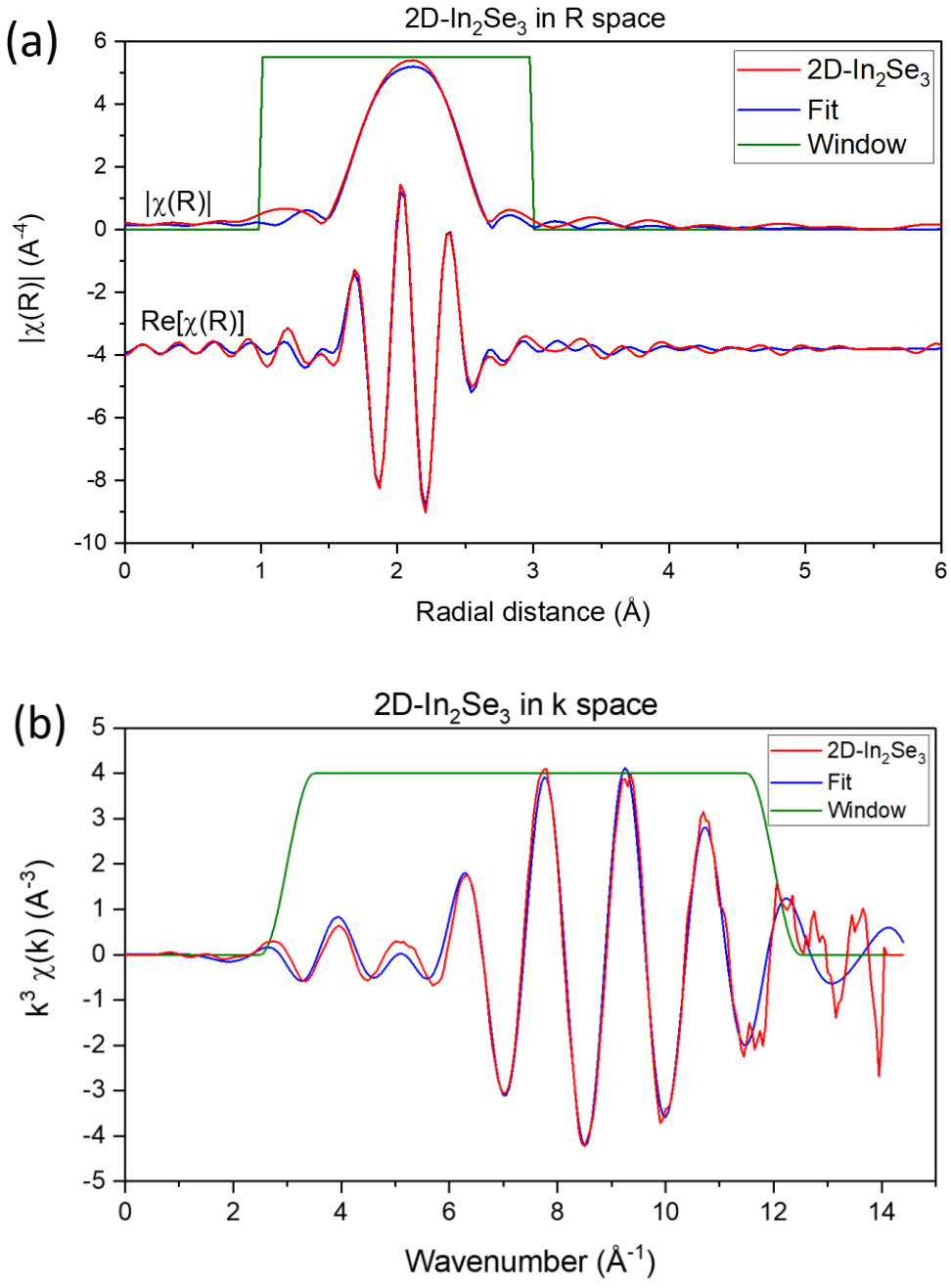

Fig. 4.8. (a) Fourier transforms of k^3-weighted Se K-edge of EXAFS spectrum of 2D-In_2Se_3. The upper spectrum shows the magnitude of χ(R) and the bottom spectrum shows the real part of χ(R). (b) k^3-weighted Se K-edge of EXAFS spectrum of 2D-In_2Se_3 in k space. The

EXAFS data fitting was performed by Mr Wentian Niu from Tsang group. The data analysis and plotting were performed by the author.

Table 4.2. EXAFS scattering path analysis of 2D-In_2Se_3.

Scattering path	Bonding length (Å)	Coordination number	σ^2 ‡
Se-In	2.48 ± 0.01	0.9 ± 0.2	0.006
Se-Se	2.40 ± 0.01	0.9 ± 0.1	0.004

R = 2%; Kwt=1,2,3; k range 3-12; R range 1-3; Enot: -1.83 ± 2.44 §

Fig. 4.8 (a) and (b) illustrate the EXAFS spectrum at Se K-edge of 2D-In_2Se_3 in R space and k space, respectively. From Table 4.2, the coordination number of Se-In (Z_{Se-In}) and Se-Se (Z_{Se-Se}) is 0.9 ± 0.2 and 0.9 ± 0.1, respectively. From literature, Z_{Se-In} is 2.1 while Z_{Se-Se} is 0.4 for α-In_2Se_3[7]. However, the positive experimental value of Z_{Se-Se} suggested that there exists a species or some species with Se-Se bonding, presumably the elemental allotropes of selenium which are usually in the form of Se polymeric rings (for example Se_8, Se_6 or Se_7)[8]. In Se rings, each Se atom is linked to two other Se atoms, making Z_{Se-Se} to be 2 and Z_{Se-In} to be 0. Bear in mind that the weight ratio from the LCF results, the ratio of Se^0 and Se^{2-} is 1:1. As mentioned, XAS measures the bulk. It can be deduced that half of the sample stays as the layered structure of α-In_2Se_3 (Se^{2-}) and another half is oxidised Se species (*i.e.* Se rings, Se^0)[8]. The averages of Z_{Se-In} and Z_{Se-Se} would both be 1 by calculation after

‡ σ^2 represents the disorder in the neighbour distance. The higher value indicates the structure is more disordered.

§ R is a percentage misfit or a numerical evaluation of how closely the fitted function overplots the data. Kwt is shorten for k-weights. It is used to multiply $\chi(k)$ to amplify the spectrum at the high-k end and make all parts of the data range contribute equivalently. In this EXAFS analysis, k^1, k^2 and k^3 are used to analyse the data. k range and R range refer to the range of the window for EXAFS fitting. Enot is the energy difference between the absorption energy in experimental value and calculated value.

considering the 1:1 LCF weights; these calculated values match with the experimental EXAFS coordination number results.

The XAS analysis seems to indicate that Se species such as Se rings coexist with the layered structure of α-In_2Se_3 (Se^{2-}). However, this claim has contradicted the STEM and TEM results in section *4.1.1.2*. No Se cluster, which should appear as a discrete molecule, has been observed in the microscopy images. Instead, the STEM images show a well-aligned atomic structure (all the surface selenium atoms are presumably Se^{2-} species as it is bonded in 2D-In_2Se_3) without significant vacancies or defects. This opposes the claim that there is a 1:1 ratio of Se^0 species and Se^{2-} species. It should be noted that XAS could be a destructive technique when the X-ray irradiation is too strong for the material. Therefore, there is a possibility that the unexpected Se clusters might be produced by X-ray beam-induced damage by oxidising Se^{2-} to Se^0.

4.1.1.4. Raman spectroscopy

In general, Raman spectroscopy is used to identify the crystalline phase of In_2Se_3 due to the presence of distinct vibrational modes for the different phases. One wavenumber should not be used alone to distinguish a phase from the other, but rather a group of wavenumbers or comparison to other sets of Raman spectra should be used to identify a phase or to correlate the eventual shift or misses in the values[9].

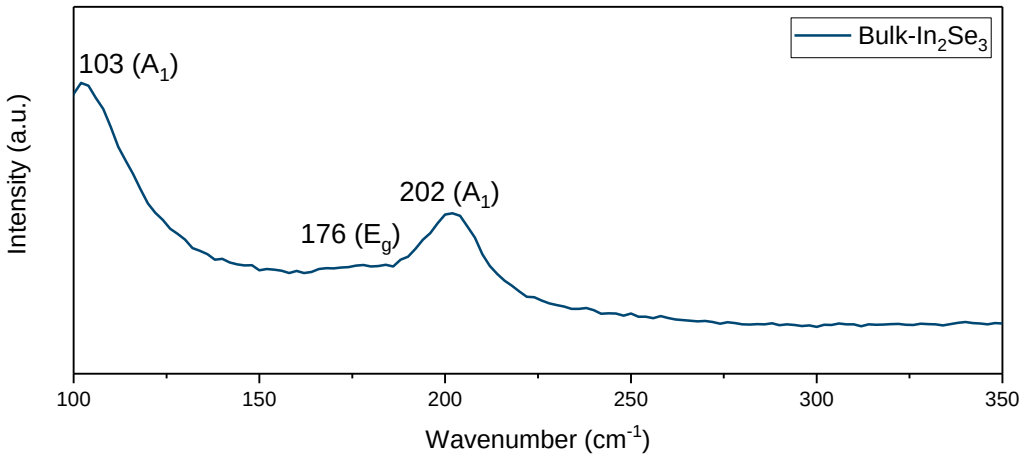

Fig. 4.9. Raman spectra of Bulk-In_2Se_3 in the air at room temperature (T = 298 K). The Raman measurements were performed by the author and Mr Wentian Niu from Tsang group at the Department of Chemistry, University of Oxford. The data work-up and analysis were performed by the author.

The Raman spectrum of Bulk-In_2Se_3 is shown in Fig. 4.9. The Raman modes are centred at 103 cm^{-1} and 202 cm^{-1} which correspond to A_1 mode, and 176 cm^{-1} corresponds to E_g mode[10, 11]. The Raman spectrum further confirms that Bulk-In_2Se_3 is the rhombohedral α-In_2Se_3 with R3m space group.

Fig. 4.10 (a) shows the Raman spectra of 2D-In_2Se_3, a total of 6 scans were collected. The 6 scans were split into three subsets according to their time of laser exposure and the laser power. The conditions were respectively: 1) four 8-second laser exposures with 50 mW laser power, 2) four 5-second laser exposures with 100 mW laser power, and 3) four 5-second laser exposures with 50 mW laser power. Each set of measurement conditions were repeated for two times to confirm their reproducibility. However, the scans were non-reproducible for all sets of measurement conditions as all of them show different peak positions. None of them looks similar to the literature Raman spectra in Fig. 4.10 (b). Worse still, visible laser damage to the samples was observed following Raman measurements. As stated in the XAS

analysis, 2D-In_2Se_3 might be a relatively fragile material under intense irradiation. Therefore, it is concluded that Raman spectroscopy was found to be unsuitable for the characterisation of 2D-In_2Se_3 due to the problems of sample damage and the phase of 2D-In_2Se_3 is inconclusive by the Raman spectroscopy.

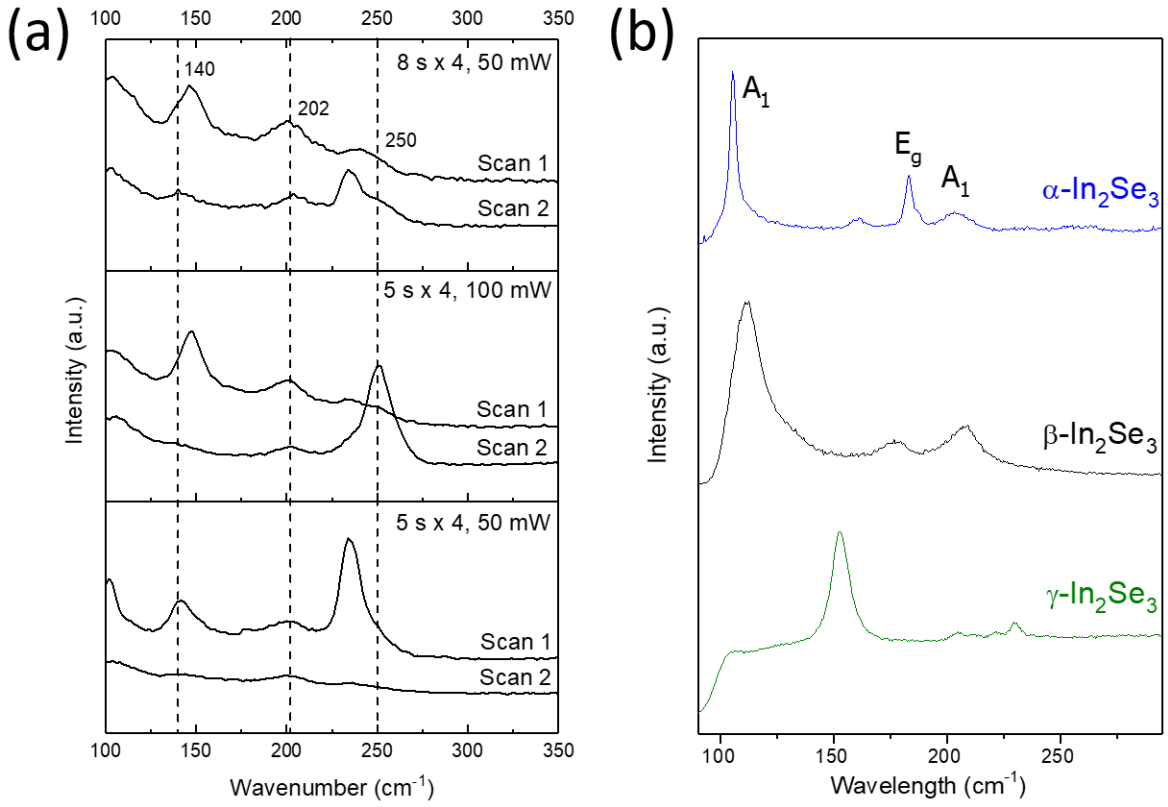

Fig. 4.10. Raman spectra of (a) 6 scans of 2D-In_2Se_3 under three subsets measurement conditions in the air at room temperature at a laser wavelength of 785 nm and (b) the literature Raman spectra of different phases of In_2Se_3. Reproduced with the open access figure with permission of IOP from reference [10]. The Raman measurements were performed by the author and Mr Wentian Niu from Tsang group at the Department of Chemistry, University of Oxford. The data work-up and analysis were performed by the author.

4.1.1.5. Electron paramagnetic resonance

The excited electron-hole pairs that can reach the surface of the photocatalysts are more important than the excitons generated in the bulk as the reaction takes place on the surface of photocatalysts. Selenium (Se) vacancies on the surface may trap the unpaired electrons formed from the excitation steps. Electron paramagnetic resonance (EPR) can detect the unpaired electrons as shown in Fig. 4.11.

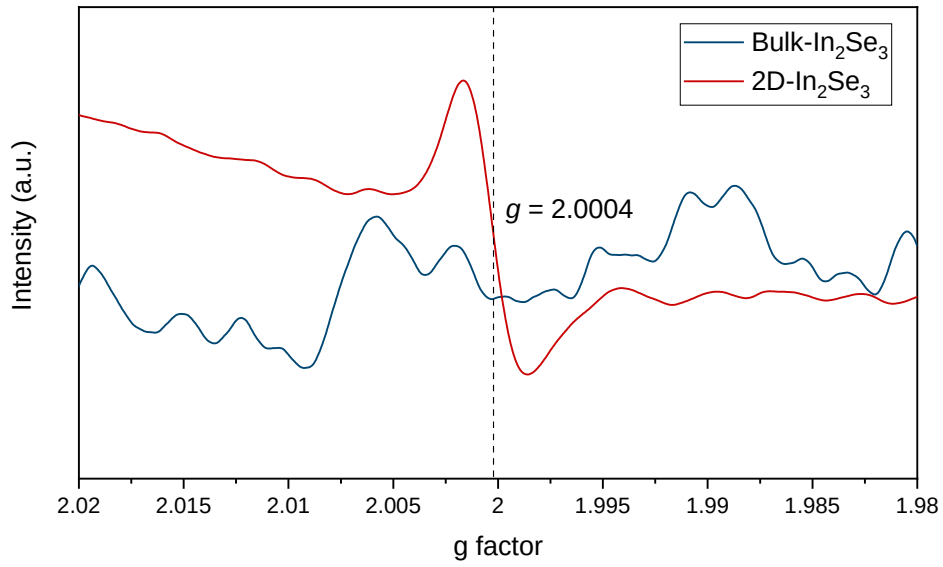

Fig. 4.11. EPR pattern of Bulk-In_2Se_3 (blue) and 2D-In_2Se_3 (red). The CW EPR measurements were performed by Mr Yiyang Li from Tsang group at the Department of Chemistry, University of Oxford. The data work-up and analysis were performed by the author.

It is shown that Bulk-In_2Se_3 is EPR-silent, implying there is a minimal number of unpaired electrons. Hence, Bulk-In_2Se_3 is diamagnetic, which is in agreement with the literature[12]. In contrast, 2D-In_2Se_3 shows an EPR signal at g = 2.0004. In general, group VI singly charge anion vacancies or defect that involves a classic electron trap will give rise to isotropic EPR spectra with a g value that is very close to a free spin (g = 2.0023)[13]. Therefore, it is expected

that the signal for 2D-In_2Se_3 corresponds to free electrons trapped on Se vacancies, further deducing Bulk-In_2Se_3 has an only insignificant amount of Se vacancies[13, 14].

The concentration of the Se vacancies is likely to be very low as the vacancies seem absent in the STEM images in section *4.1.1.2*. However, it should be noted that EPR is a very sensitive technique, and it can pick up a very low concentration of unpaired electrons. Moreover, bear in mind that EPR can only probe species with unpaired electrons, such as the singly ionised Se vacancies as mentioned, radicals and triplets. Therefore, 2D-In_2Se_3 might also contain some neutral or doubly ionised Se vacancies, yet these species are not paramagnetic so cannot be monitored by EPR.

4.1.1.6. X-ray photoelectron spectroscopy

XPS is used to study the chemical composition of Bulk-In_2Se_3 and 2D-In_2Se_3. In Fig. 4.12 (a), the binding energy of In 3d 5/2 shifts from 444.90 eV to 445.94 eV for Bulk-In_2Se_3 to 2D-In_2Se_3. A similar positive shift is observed in In 3d 3/2 from 452.50 eV to 453.54 eV. This blue shift shows the In in 2D-In_2Se_3 has higher binding energy than Bulk-In_2Se_3, implying it has a lower electron density (or is more positively charged) after the exfoliation. In Fig 4.12 (b), the binding energy of Se 3d 5/2 shifts from 57.89 eV to 55.02 eV. A similar negative shift is observed in Se 3d 3/2 from 58.75 eV to 55.88 eV. The negative shift indicates that the Se in 2D-In_2Se_3 has lower binding energy than Bulk-In_2Se_3, and it has a higher electron density (or is more negative charged). This trend suggested that there might be charge transfer between In cation and Se anion after the exfoliation. From the results of EPR, it is concluded that there are Se vacancies in 2D-In_2Se_3. Therefore, In_2Se_{3-x} is a more accurate chemical formula for 2D-In_2Se_3. The charge of In cation is +3, while the charge for Se anion is between -2 and -3 instead of -2 in Bulk-In_2Se_3, as some Se vacancies were created during exfoliation. Therefore, more electrons are needed for Se to charge balance the 2D-

In_2Se_3 system, and electrons are drawn from In cations. Hence, the electron density of In in 2D-In_2Se_3 is lower than that in Bulk-In_2Se_3; the electron density of Se in 2D-In_2Se_3 is higher than that in Bulk-In_2Se_3 due to the presence of Se vacancies. Thus, the XPS results are in good agreement with the EPR results.

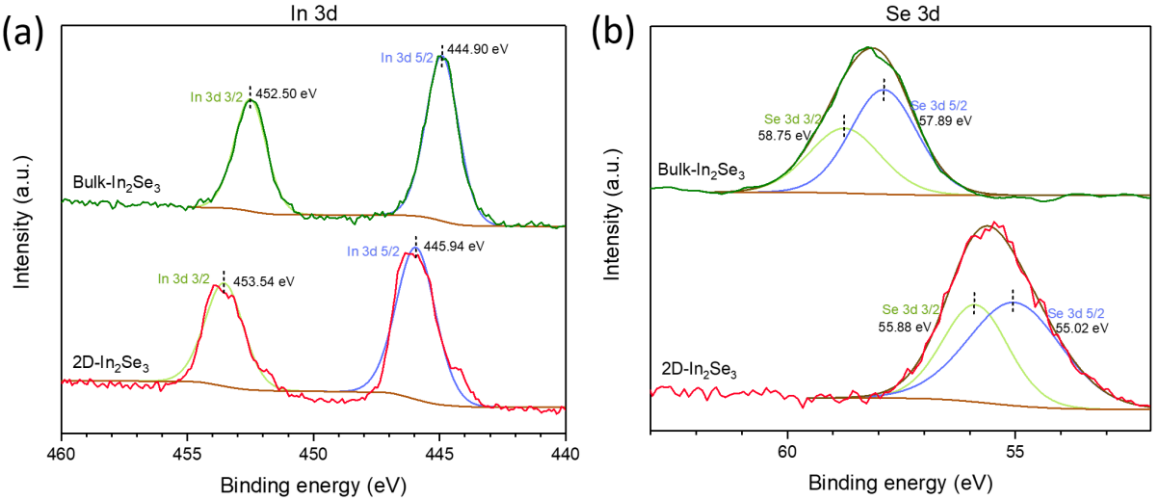

Fig. 4.12. High-resolution XPS spectra of (a) In 3d and (b) Se 3d of Bulk-In_2Se_3 and 2D-In_2Se_3. The XPS measurements were performed by Dr Shaoliang Guan from HarwellXPS facilities, United Kingdom. The data analysis was performed by the author. A special acknowledgement is given to Dr Jianwei Zheng for the XPS result discussions.

4.1.2. Photocatalytic performance testing

After exfoliation, 2D-In_2Se_3 shows a nearly doubled hydrogen evolution rate photocatalytic water splitting performance compared to Bulk-In_2Se_3 as seen from Fig. 4.13 (a). It is consistent with the previous assumption that with the increased surface area and active sites after exfoliation, more water molecules are accessible to the reaction sites. It increases the possibility for water splitting and hence the hydrogen production amount. In addition, 2D-In_2Se_3 has a shorter migration distance (as it is thinner) for the photogenerated electrons and holes compared to Bulk-In_2Se_3, which facilitates rapid electron-hole migration to the surface

of the catalysts and lowers the recombination probability of the photogenerated carrier[15]. On the same figure, the H_2/O_2 gas evolution rate of 2D-In_2Se_3 with no sacrificial reagent shows a nearly 2:1 stoichiometric ratio. It suggested that the reaction is an overall water splitting reaction. In Fig. 4.13 (b), the photocatalytic activities of three batches of 2D-In_2Se_3 samples, which were synthesised under identical conditions, were tested. The activities of the three samples are nearly the same, with only 5% error of activity reproducibility. It shows that the lithium intercalation method for synthesising 2D-In_2Se_3 is reproducible.

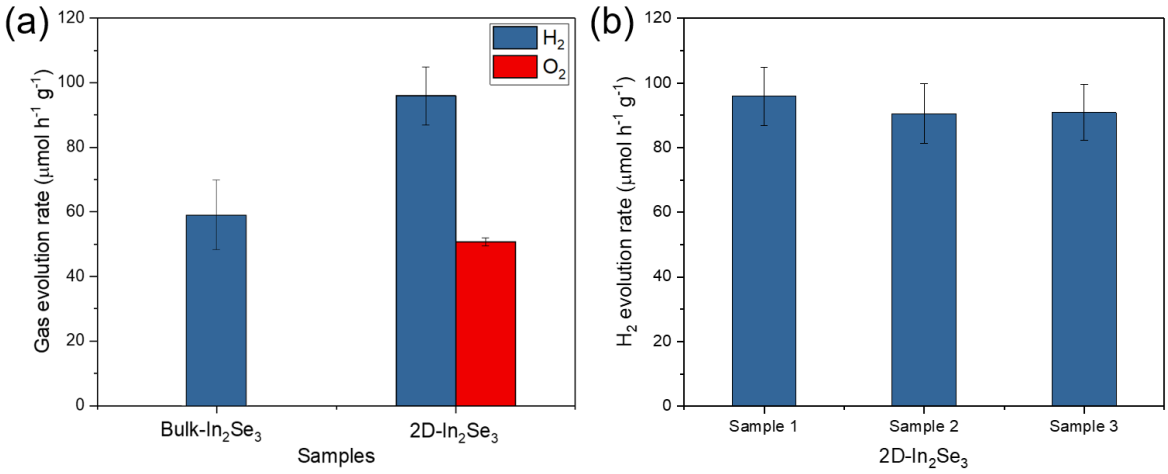

Fig. 4.13. (a) Photocatalytic water splitting reaction activity tests of Bulk-In_2Se_3 and 2D-In_2Se_3 under 300 W Xenon UV-Vis lamp irradiation at 543 K for 2 hours in Ar. The amount of hydrogen and oxygen produced were quantified by a GC equipped with TCD. Error bars indicate the standard deviation of the GC measurements. (b) Photocatalytic water splitting reaction activity tests of three 2D-In_2Se_3 samples synthesised by lithium interaction method under identical conditions. The activity tests were performed and analysed by the author.

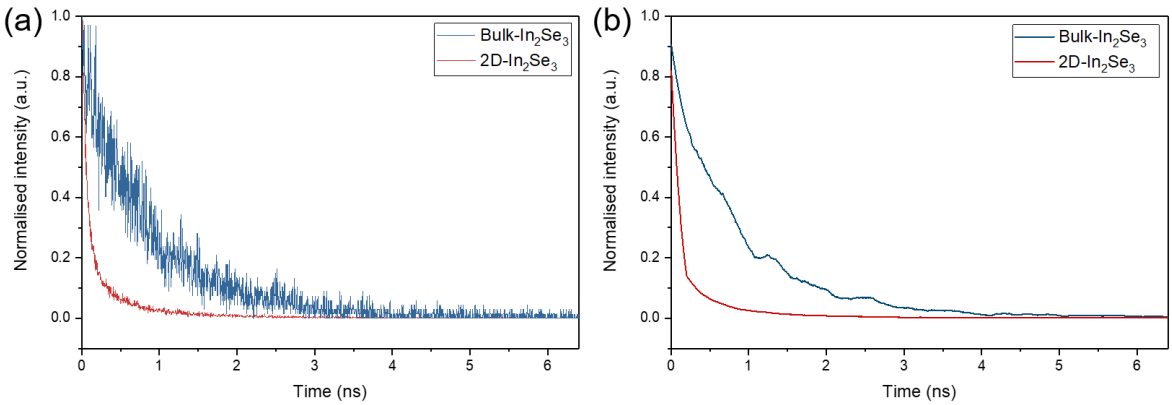

Fig. 4.14. TRPL spectra of Bulk-In_2Se_3 (blue) and 2D-In_2Se_3 (red) measured in air at ambient temperature. (a) corresponds to the raw TRPL measurements and (b) corresponds to the data that is smoothened by the Savitzky-Golay method with 100 points of window. The TRPL measurements were performed by Mr Yiyang Li from Tsang group at Prof Robert A. Taylor's laboratory at the Department of Physics, University of Oxford. A special acknowledgement was given to Prof Robert A. Taylor for permitting access to his laboratory and the TRPL instruments. The data work-up and analysis were performed by the author.

Table 4.3. The fitting parameters of the mono-exponential decay function and bi-exponential decay function for the TRPL of Bulk-In_2Se_3 and 2D-In_2Se_3, respectively. The TRPL fitting was performed by Mr Yiyang Li from Tsang group.

	A_1	**t_1 / ns**	**A_2**	**t_2 / ns**	**t average / ns**
Bulk-In_2Se_3	0.0480	0.758	/	/	0.758
2D-In_2Se_3	0.0434	0.888	0.0558	0.239	0.721

The shorter migration distance of 2D-In_2Se_3 can be proved by the TRPL spectra in Fig. 4.14 (a) and (b). The fitted exciton lifetime, t average, of Bulk-In_2Se_3 and 2D-In_2Se_3 is 0.758 ns and 0.721 ns, respectively. The fitting parameters in Table 4.3 are obtained by fitting the spectra into mono- or bi- exponential decay function, which are previously explained in

section *3.4*; the t averages are calculated according to Eq. 3.3. In Fig. 4.14 (b), it may seem that the two exciton lifetimes of 2D-In_2Se_3 and Bulk-In_2Se_3 would exhibit a larger difference. However, it should be noted that the obtained exciton lifetimes are expressed as average values. In the fitting for 2D-In_2Se_3, there exist a short time parameter, 0.230 ns, and a much longer time parameter, 0.888, while the coefficients, A_1 and A_2, are more or less similar. It explains the reason of 2D-In_2Se_3 t average being quite similar to the one of Bulk-In_2Se_3. It should also be aware that a spectrum that is fitted by a bi-exponential decay function refers to two decay processes (hence, two components in the function) might be happening. It might imply that 2D-In_2Se_3 might undergo a more complex TRPL exciton recombination process compared to Bulk-In_2Se_3.

The shorter lifetime of 2D-In_2Se_3 suggested that the more rapid migration of excitons, further implying the shorter migration distance for the charge carriers in 2D-In_2Se_3 compared to Bulk-In_2Se_3. Note that longer exciton lifetimes are always preferred and promote photocatalytic activity, but 2D-In_2Se_3 with a shorter exciton lifetime has a nearly two-fold activity compared to Bulk-In_2Se_3. It implies that the charge recombination process is not a limiting factor hindering the activities of 2D-In_2Se_3. The increased activity of 2D-In_2Se_3 compared to Bulk-In_2Se_3 might be due to other contributions such as increased surface area and active sites, as well as the intrinsic electric field in 2D materials.

Furthermore, Se vacancies might also contribute a role in enhancing photocatalytic activity. The surface Se anion vacancies can act as electron trapping sites to inhibit electron-hole recombination[16, 17]. It is also reported that anion vacancies can adjust the energy band structure by forming a higher density of state (DOS) at the VBM and a new donor level near CBM. They give the material a higher charge carrier concentration at the band edge position and a narrower bandgap, hence facilitating the carrier separation and light absorption

efficiency[18]. These potential effects are certainly just possibilities of what Se vacancies can achieve in 2D-In_2Se_3; they are needed to be further confirmed by the experimental or theoretical model.

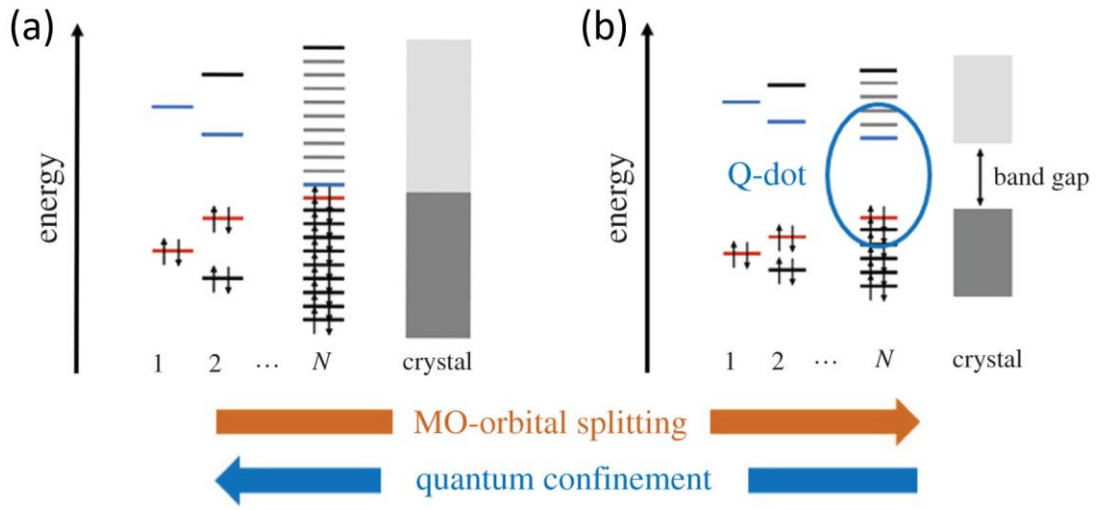

Fig. 4.15. Schematic image of the quantum confinement effect in (a) a metal and (b) a semiconductor. Reproduced with the open access figure with permission of The Royal Society from reference [19].

Moreover, it is documented that the bandgap energy of In_2Se_3 based materials is thickness dependent[20]. In general, thinner In_2Se_3 has larger bandgap energy compared to the thicker In_2Se_3. Altering the dimensions of nanomaterials would be able to tune the electronic states in nanostructured systems[19]. This trend can be attributed to the quantum confinement effect (Fig. 4.15). Specifically, this phenomenon is observed when electrons and holes being crammed into a dimension that approaches a critical quantum measurement – Bohr radius, a_B. The bandgap energy of Bulk-In_2Se_3 to 2D-In_2Se_3 is experimentally investigated by Tauc Plot. The data for plotting Tauc plots was obtained by the UV-Vis measurements. In Fig. 4.16, the bandgap energy of Bulk-In_2Se_3 and 2D-In_2Se_3 are 1.35 eV and 1.71 eV respectively. It agrees with the quantum confinement effect where the bandgap energy increases with the decreasing thickness of In_2Se_3.

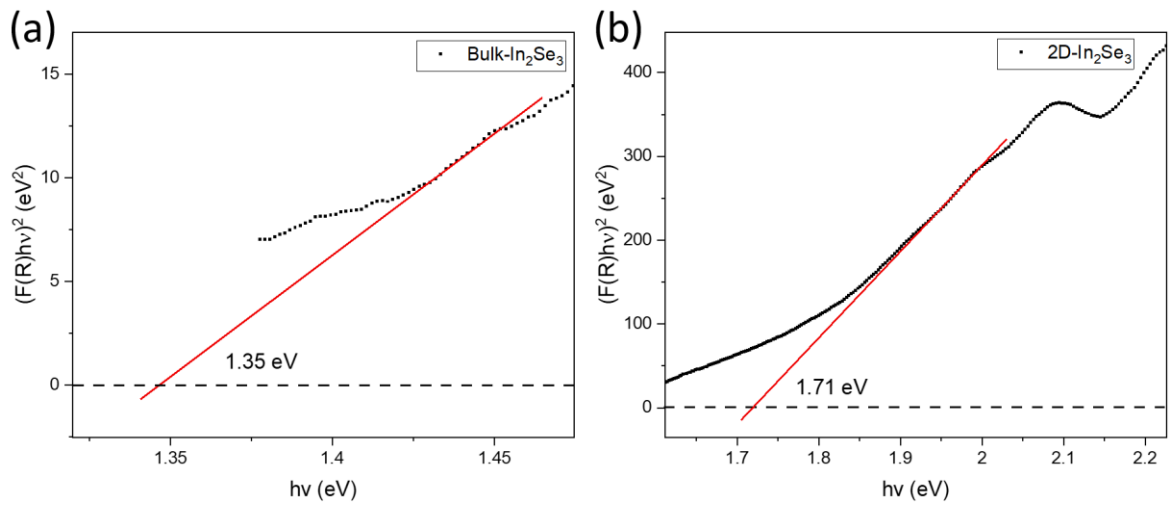

Fig. 4.16. Tauc plots for (a) Bulk-In_2Se_3 and (b) 2D-In_2Se_3 using $(F(R)hv)^2$ (Kubelka–Munk parameter) as a function versus the photon energy. The electron transitions of the two materials are assumed to be a direct allowed transition, supported by Procopio *et al.* and Lyu *et al.*[21, 22]. The UV-Vis measurements were performed by the author and Mr Wentian Niu from Tsang group at the Department of Chemistry, University of Oxford. The data work-up and analysis were performed by the author.

4.2. Metal doped In_2Se_3

As mentioned in *1.4.2.1*, the photocatalytic effect of metal-doped 2D-In_2Se_3 was explored. Doping metal as cocatalysts on the surface of photocatalysts is expected to impact the photocatalytic activity by trapping electrons or/and holes. Electron or hole trapping is a process that can promote charge separation, therefore metal doping could in turn diminish the excitons-pair recombination rate and enhance the photocatalytic activity. A range of metals was doped to 2D-In_2Se_3 by hydrothermal and sonochemical methods described in *3.2.3* and their activities were scanned.

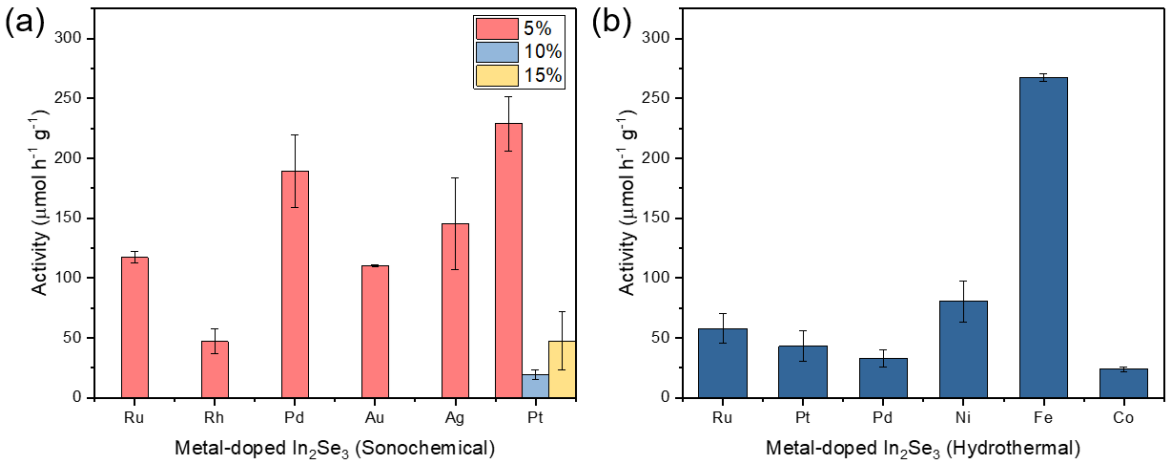

Fig. 4.17. Photocatalytic water splitting reaction activity tests of different metal-doped In_2Se_3 with (a) sonochemical and (b) hydrothermal as synthesis methods. The testing was all carried out under UV-Vis light irradiation at 543 K for 2 hours in Ar. The amount of hydrogen produced was quantified by a GC equipped with a TCD. Error bars indicate the standard deviation of the GC measurements. The activity tests were performed and analysed by the author.

Photocatalytic activities are largely altered after doping some metals as shown in Fig. 4.17. Among the metal-doped 2D-In_2Se_3, Fe-doped (hydrothermal) 2D-In_2Se_3 and 5% Pt-doped (sonochemical) 2D-In_2Se_3 have shown the best hydrogen production rate.

Pt is a well-known noble metal with excellent hydrogen production ability due to its binding of hydrogen atoms with the near-neutral free energy of adsorption ($\Delta G \sim 0$) and low overpotential for hydrogen generation[23-25]. Different concentration (5 wt.%, 10% and 15%) of Pt has been doped to 2D-In_2Se_3. Yet, the dopant concentration does not positively correlate to the photocatalytic activity. It appears that there is an optimum concentration of dopant metals on a photocatalyst. Many previous reports on metal-doped photocatalysts showed the enhancement of photoactivity only happens for a specific amount (or optimal amount) of metals doping concentration, otherwise detrimental effects occur[26-28].

The existence of an optimal metal dopant concentration can be explained by the balance of dopant metals to be a trapping centre for charge carriers or a recombination centre. At lower doping concentrations (below the optimal value), the photocatalytic activity increases with a dopant concentration as there are few trapping sites available. Increasing the trapping sites would decrease the probability of charge carriers' recombination. However, at dopant concentrations above the optical value, the probability of recombination through tunnelling between charge carriers in trapped sites increases exponentially[29]. It is because the average distance between trap sites decreases with an increasing number of dopants within a surface; the recombination rate is depending on Eq. 4.1 [30]. Also, the formation of metal clusters with excessive metal doping content will lead to an enhanced rate of charge recombination[31, 32].

$$k_{recomb} \propto \exp\left(-2R/a_0\right) \qquad (4.1)$$

where R is the distance separating the electron-hole pairs and a_0 is the radius of the hydrogenic wave function of the trapped charge carrier.

However, interestingly, doping some metals decrease the photocatalytic activities. For example, Co-doped 2D-In_2Se_3 showed lower photocatalytic activity than the undoped 2D-In_2Se_3. It might be due to the high stability of Co^{3+}, assuming that the cobalt is doped as a low-spin Co^{3+} ion on 2D-In_2Se_3. It is known that a complex with a low-spin configuration (t_{2g}^6 in an octahedral field) will contribute to a partly closed electronic configuration[33]. A partially closed electronic shell is quite stable, which makes electron or hole trapping unfavourable[34]. This explanation can still provide insights into why some metals gave lower activity than expected.

The photocatalytic activity of the series of metal-doped 2D-In_2Se_3 appears to be a complex function including the dopant concentration, the energy level of dopants within the lattice, their d electronic configuration, distribution of dopants and electron donor concentration.

The metal doping screening here is done empirically; the photocatalytic effect of doping metals on 2D-In_2Se_3 is still unclear. Theoretical and experimental work needs to be done to explore this further.

Surprisingly, the Fe-doped 2D-In_2Se_3 also gives excellent water splitting photocatalytic activity. There have been lots of publications about TiO_2, one of the most well-studied semiconductors, doped with Fe for decomposing organic substances[35-37]. However, there have been relatively fewer reports about semiconductors doped with Fe as low-cost 3d transition metals for hydrogen production by water splitting. Therefore, considering Fe has the more interesting science compared to Pt-In_2Se_3 and the attractiveness of being economical, the following study will focus on Fe-doped 2D-In_2Se_3 (Fe-In_2Se_3).

4.2.1. Characterisations of Fe-In_2Se_3

Fig. 4.18 shows the XRD patterns of 2D-In_2Se_3, Bulk-In_2Se_3 and Fe-In_2Se_3. No significant peak appears after Fe-doping as seen from the XRD pattern of Fe-In_2Se_3. It suggested that the thin-sheet-like 2D morphology has remained after the doping; there is no significant change in the 2D-In_2Se_3 structure after the Fe-doping. This also points out the high dispersion of Fe species and there is no bulky form of Fe nanoparticle or metal cluster is formed during the doping. The Fe-In_2Se_3 XRD pattern also does not show any similar pattern characteristic to ultrasmall iron oxide nanoparticles or iron oxide phase from the literature[38, 39]. There are still some very small peaks that remain for the XRD patterns of 2D-In_2Se_3 and Fe-In_2Se_3, but they are insignificant and are mainly caused by the noise during XRD measurements. This suggested that elemental Fe did not exist as an individual phase after the hydrothermal treatment. The Fe ions might possibly be inserted into the structure of 2D-In_2Se_3 (*i.e.* the surface of the 2D-material) or substitute part of the In^{3+} cation[40].

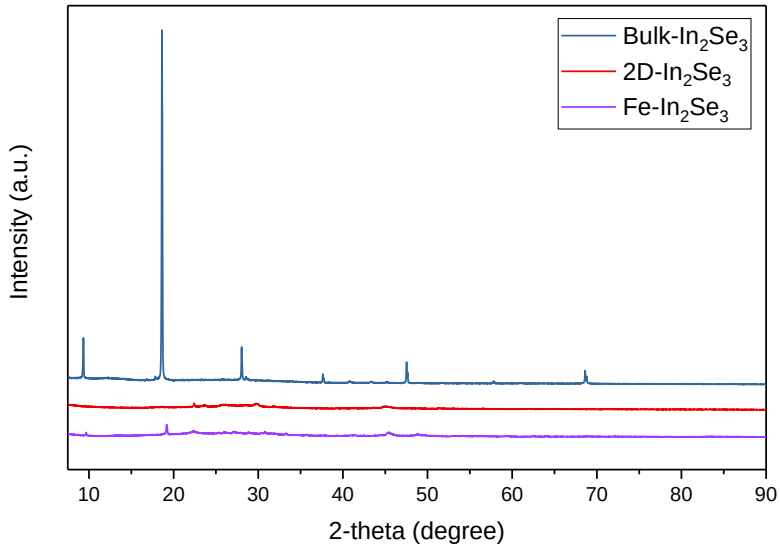

Fig. 4.18. The XRD patterns of Bulk-In_2Se_3, 2D-In_2Se_3 and Fe-In_2Se_3. The XRD was performed at room temperature with ground powder samples. The XRD measurements were performed and analysed by the author at the Department of Chemistry, University of Oxford.

In the In 3d (Fig. 4.19 (a)) spectra and Se 3d (Fig. 4.19 (b)) spectra, both the binding energy of In 3d and Se 3d of Fe-In_2Se_3 downshifted compared to 2D-In_2Se_3. This implies that the electron density of In and Se increases after the Fe doping; the two elements are more electron-rich. This can be justified by the electronegativity difference between the atoms. The electronegativity of Se and Fe is 2.55 and 1.83, respectively[8] Fe is likely to dope on the surface of Se (will be further justified in the Fe 2p XPS spectrum as follows), therefore, electrons will likely be drawn from Fe to Se. The Se atoms will then be too electron-rich after drawing electrons from Fe, hence, the electron density is believed to be further transferred downward from Se to In, to charge balance the system. As a result, In and Se is more electron-dense after the Fe doping, which leads to the shift in lower binding energy.

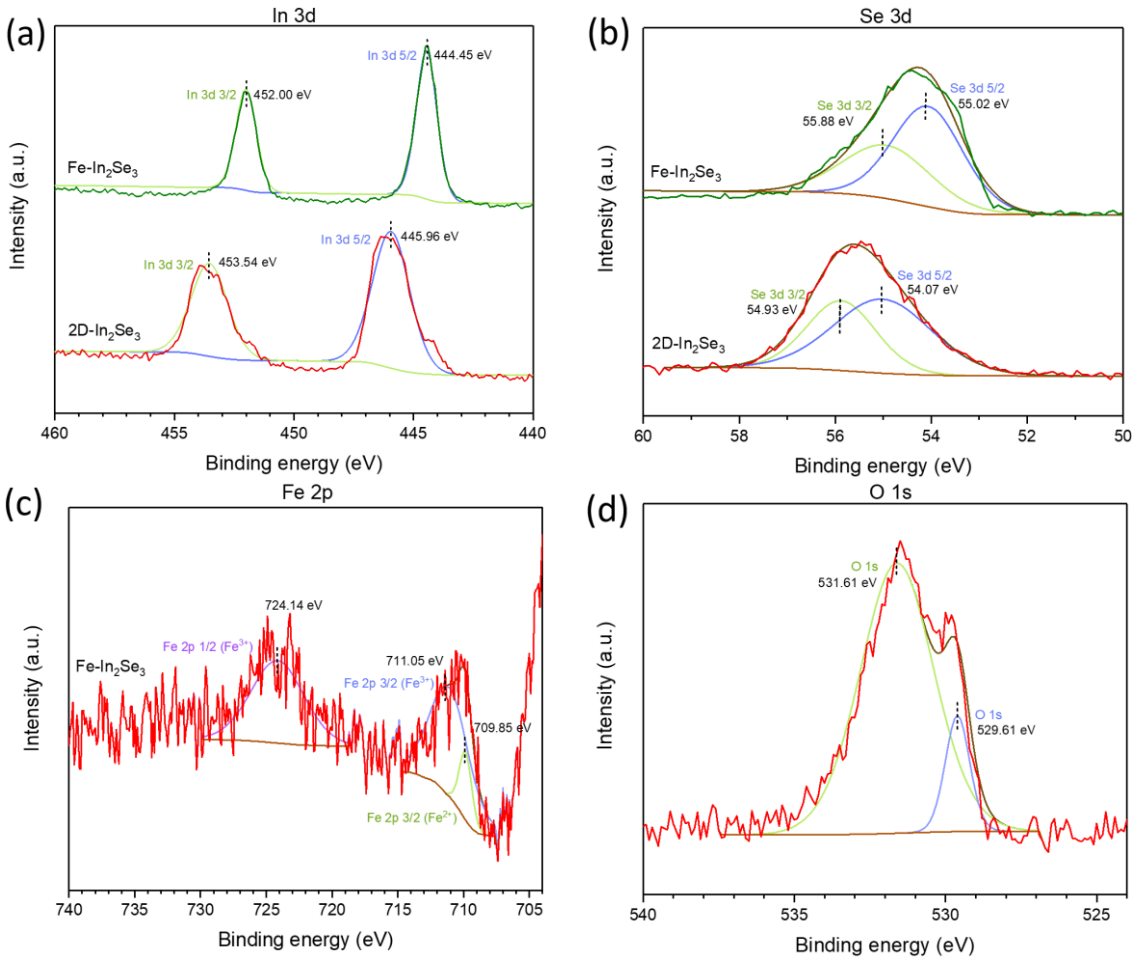

Fig. 4.19. High-resolution XPS spectra of (a) In 3d and (b) Se 3d of 2D-In_2Se_3 and Fe-In_2Se_3. High-resolution XPS spectra of (c) Fe 2p and (d) O 1s of Fe-In_2Se_3. The XPS measurements were performed by Dr Shaoliang Guan from HarwellXPS facilities, United Kingdom. The data analysis was performed by the author.

In the Fe 2p spectrum (Fig. 4.19 (c)), it is reported that Fe^{3+} and Fe^{2+} $2p_{3/2}$ are at 711.05 and 709.85 eV, respectively, while Fe^{3+} $2p_{1/2}$ peak is located at 724.14 eV [40]. This confirmed that the Fe^{3+} ions were doped successfully into the 2D-In_2Se_3. As XPS is a surface technique, the presence of the peaks in the Fe 2p spectrum indicates that Fe ions are enriched on the surface of 2D-In_2Se_3 after the hydrothermal doping treatment, therefore, believed to be bonded with Se on the surface layer. Furthermore, the coexistence of the two chemical states of Fe (Fe^{3+} and Fe^{2+}) is a consequence of the partial reduction of Fe^{3+} by generated electrons due to the

incident light (X-ray) excitation on Fe-In_2Se_3[41]. The transformation of electrons between Fe^{3+} and Fe^{2+} is shown by Eq. 4.2 below. The mean peak in the XPS spectra is at 711.05 eV (and 724.14 eV) which attribute to Fe^{3+} as the major Fe species.

The O 1s spectrum (Fig. 4.19 (d)) can be deconvoluted into two components: the one located at 529.61 eV can be assigned to Fe-O (O^{2-}), while the second peak at 531.61 eV is attributed to Fe-OH (O^-)[40, 42-44]. This implies that iron oxide and iron hydroxide might not be completely reduced during the treatment with hydrogen gas in the furnace. Future work could consider prolonging the hydrogen treatment or changing the reaction conditions to ensure complete reduction.

From the TEM images in Fig. 4.20 (a) and (b), the thin-sheet-like morphology has remained after metal doping. It appeared that no big nanoparticle or atomic cluster is forming on the surface of Fe-In_2Se_3, in agreement with the XRD pattern in Fig. 4.18. It could be assumed that Fe ions have been successfully doped on the surface of 2D-In_2Se_3. Fig. 4.20 (c) shows the electron diffraction pattern of Fe-In_2Se_3, which shows a principal axis of hexagonal symmetry. The electron diffraction simulations of α-In_2Se_3, as the most probable phases of the sample, have been done to confirm its identity. The diffraction pattern in Fig. 4.20 (d) is simulated along zone axis (001) with the index of the crystallographic plane. This simulation demonstrates hexagonal symmetry. By comparing the simulation and experimental pattern, it is revealed that the sample remained as α-In_2Se_3 after Fe doping. The Fe doping cannot be revealed by the diffraction here, further confirming the absence of bulky Fe clusters.

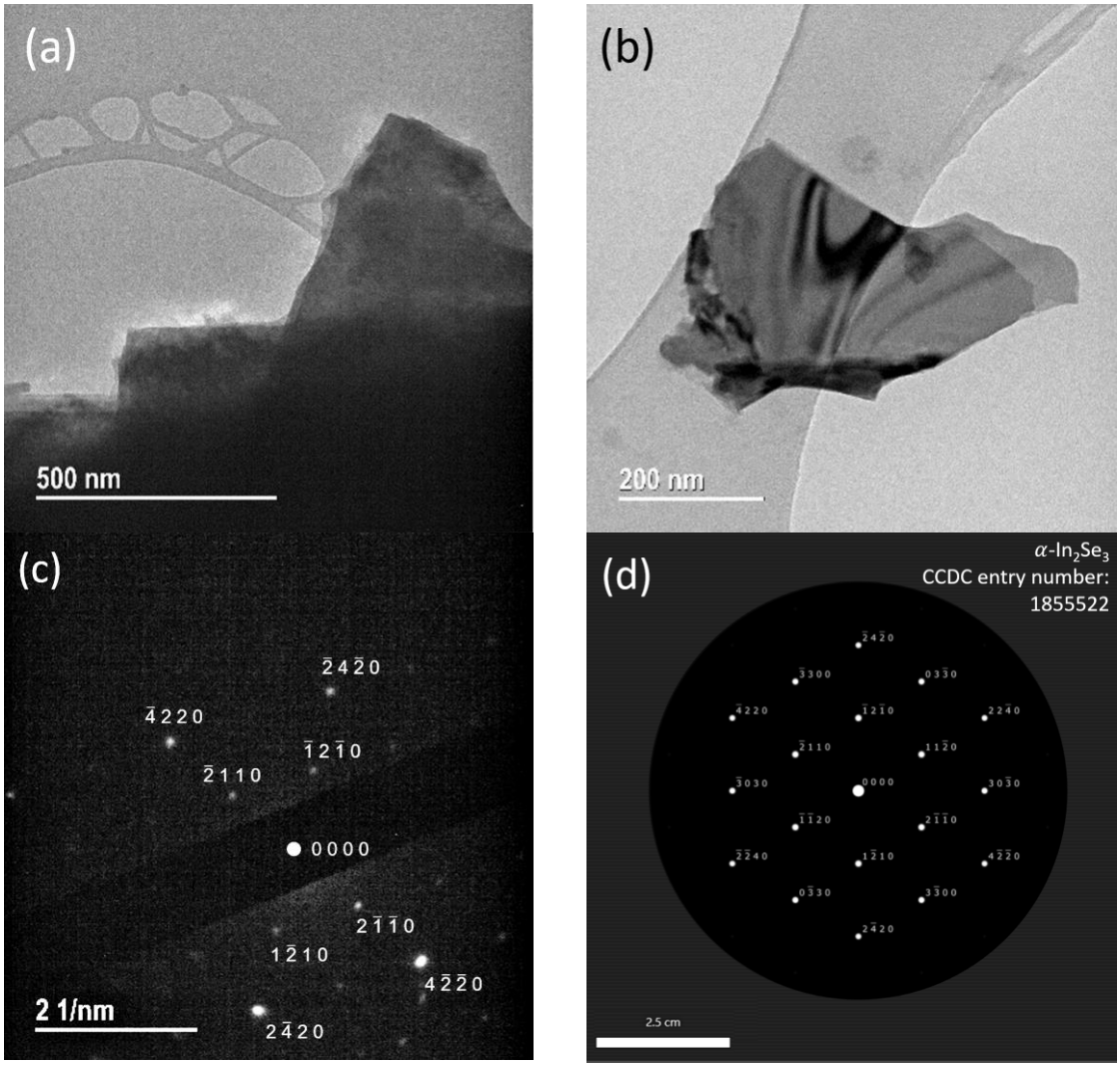

Fig. 4.20. (a-b) Conventional TEM images and (c) electron diffractions of Fe-In_2Se_3. (d) Electron diffraction pattern simulation of α-In_2Se_3 (CCDC entry number: 1855522)[2]. The imaging and electron diffraction pattern simulation were performed by Mr Ping-Luen (Baron) Ho from Tsang group in the David Cockayne Centre for Electron Microscopy and related facilities at the Department of Materials, University of Oxford. The selection and analysis of the images were performed by the author.

4.2.2. Photocatalytic performance testing

The Fe-doping of 2D-In_2Se_3 has resulted in a nearly three-fold enhancement of photocatalytic activities as shown in Fig. 4.21. In Fig. 4.22 (a) and (b) and Table 4.4, the exciton lifetimes were prolonged from 0.721 ns to 0.850 ns after Fe is doped to 2D-In_2Se_3. It is believed that Fe-doping causes a charge separation and retarded carrier recombination, which is in good agreement with the TRPL results.

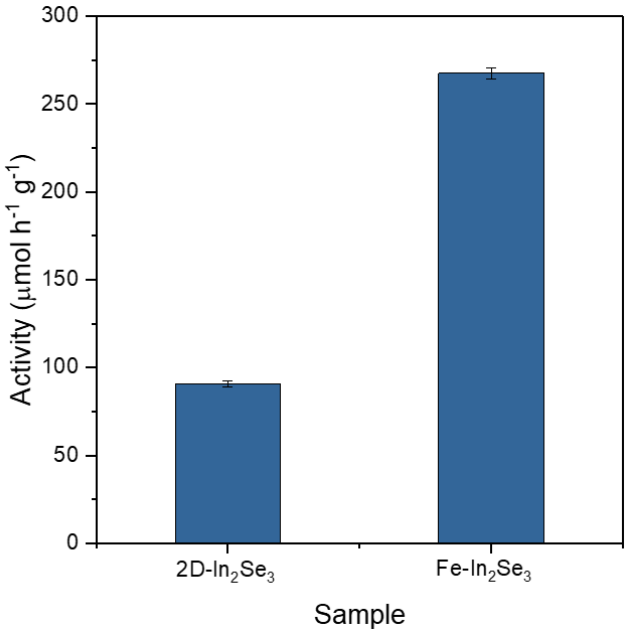

Fig. 4.21. (a) Photocatalytic water splitting reaction activity tests of 2D-In_2Se_3 and Fe-In_2Se_3 under 300 W Xenon UV-Vis lamp irradiation at 543 K for 2 hours in Ar. The amount of hydrogen produced was quantified by a GC equipped with a TCD. Error bars indicate the standard deviation of the GC measurements. (b) TRPL of 2D-In_2Se_3 (red) and Fe-In_2Se_3 (purple) were measured in air at ambient temperature. The data is smoothened by the Savitzky-Golay method with 100 points of window. The activity tests were performed and analysed by the author.

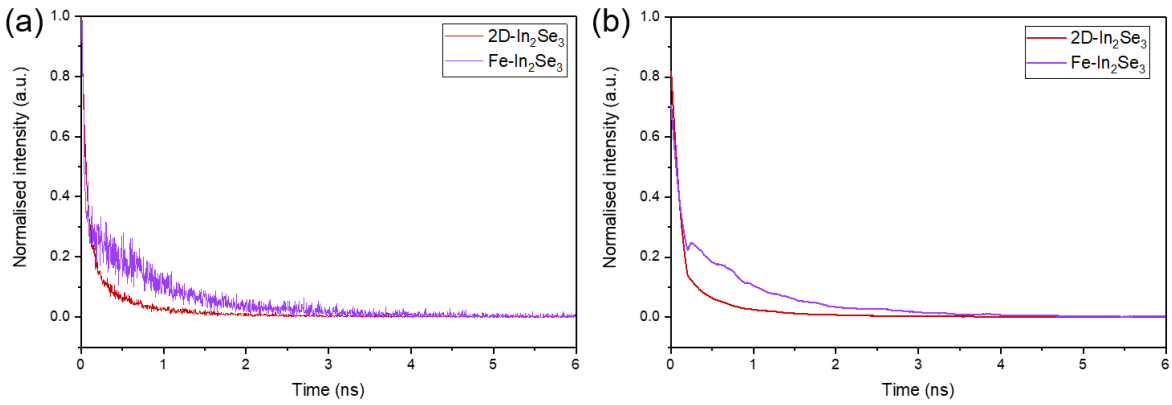

Fig. 4.22. TRPL spectra of 2D-In_2Se_3 (red) and Fe-In_2Se_3 (purple) were measured in air at ambient temperature. (a) corresponds to the raw TRPL measurements and (b) corresponds to the data that is smoothened by the Savitzky-Golay method with 100 points of window. The TRPL measurements were performed by Mr Yiyang Li from Tsang group at Prof Robert A. Taylor's laboratory at the Department of Physics, University of Oxford. The data work-up and analysis were performed by the author.

Table 4.4. The fitting parameters of the bi-exponential decay function and mono-exponential decay function for the TRPL of 2D-In_2Se_3 and Fe-In_2Se_3, respectively. The TRPL fitting was performed by Mr Yiyang Li from Tsang group.

	A_1	**t_1**	**A_2**	**t_2**	**t average**
2D-In_2Se_3	0.0434	0.888	0.0558	0.239	0.721
Fe-In_2Se_3	0.0500	0.850	/	/	0.850

It is believed that there are two types of configuration energy level after doping Fe^{3+} ions in the semiconductor system, that is the oxidation level of Fe^{4+}/Fe^{3+} which lie above the VBM and the reduction level of Fe^{3+}/Fe^{2+} which is below the CBM of 2D-In_2Se_3[45, 46]. Fe^{2+} can be formed when a photogenerated electron migrates from 2D-In_2Se_3 to Fe^{3+} (Eq. 4.2). Fe^{2+} will eventually return to Fe^{3+} and release electrons. The back formation is due to Fe^{2+} is relatively

less stable than Fe^{3+} as the loss of the d^5 electronic configuration (Eq. 4.3). At the same time, Fe^{3+} could act as a hole trap by picking up the photogenerated hole from the VB to form Fe^{4+} briefly (Eq. 4.4). This reaction is believed to drive by the higher energy level of Fe^{3+}/Fe^{4+} than VBM of 2D-In_2Se_3. Fe^{3+} will be restored again due to the preferred stable electronic configuration from the viewpoint of crystal field theory (Eq. 4.5)[42, 45, 46].

$$Fe^{3+} + e^- \rightarrow Fe^{2+} \qquad (4.2)$$

$$Fe^{2+} \rightarrow Fe^{3+} + e^- \qquad (4.3)$$

$$Fe^{3+} + h^+ \rightarrow Fe^{4+} \qquad (4.4)$$

$$Fe^{4+} \rightarrow Fe^{3+} + h^+ \qquad (4.5)$$

In other words, the charge carriers can transport to different energy levels of Fe^{3+} ions and the Fe electronic levels act as a medium that the excited charged species will be retained for a short time before further migration and be consumed by water splitting or undergoing charge recombination[42, 47]. Therefore, this minimises the possibility of charge recombination before being transferred to the catalyst-water interface to initiate the water splitting redox reaction. As a result, Fe-doping improves the photocatalytic activity of 2D-In_2Se_3.

It should be noted that, when the iron concentration is too high, Fe^{3+} may act as recombination centres by Eq. 4.6 to Eq. 4.7 [48]. Therefore, as competition exists among these redox processes, there exist a certain amount of Fe (III) ion dopants that can work with the best efficiency. As a result, the resulting photo-activity of the doped catalysts derived from a balance of the above factors, which some of them play a contrasting role.

$$Fe^{3+} + e^- \rightarrow Fe^{2+} \qquad (4.6)$$

$$Fe^{2+} + h^+ \rightarrow Fe^{3+} \qquad (4.7)$$

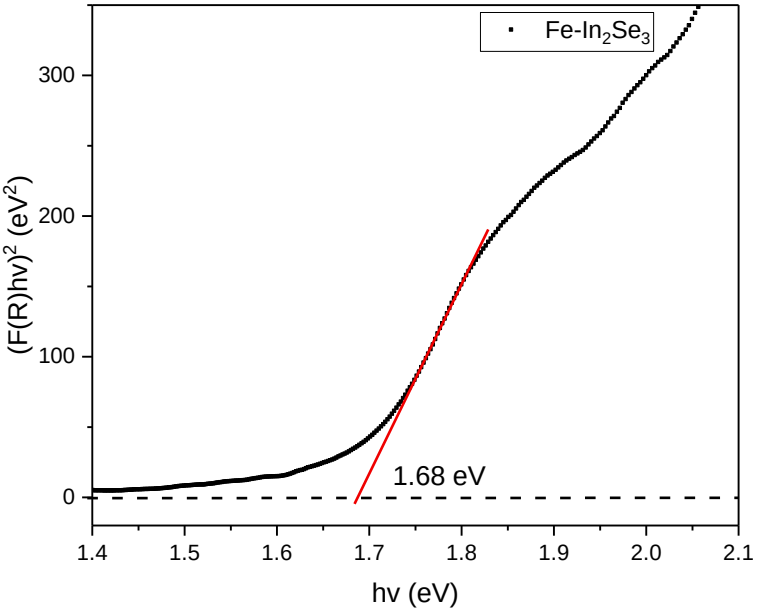

Fig. 4.23. Tauc plots for Fe-In_2Se_3 using $(F(R)hv)^2$ (Kubelka–Munk parameter) as a function versus the photon energy. The electron transitions of the two materials are assumed to be a direct allowed transition. The UV-Vis measurements were performed by the author and Mr Wentian Niu from Tsang group at the Department of Chemistry, University of Oxford. The data work-up and analysis were performed by the author.

It is also possible that the metal doping extends the photo-response of In_2Se_3 into the visible spectrum or a larger light absorption range. This is investigated by the Tauc plot in Fig. 4.23. The introduction of Fe^{3+} dopant on the 2D-In_2Se_3 structure decreases the bandgap energy from 1.71 eV (Fig. 4.16 (b)) to 1.68 eV (Fig. 4.23). The redshift implies that the Fe doping extends the light absorption to a longer wavelength with lower energy. The increased of the intrinsic absorption edge of the Fe-doped In_2Se_3 can be further interpreted either by the introduction of additional electronic states (Fe^{4+}/Fe^{3+} and Fe^{3+}/Fe^{2+}) levels that span across the bandgap of 2D-In_2Se_3[42], which decrease the energy bandgap of 2D-In_2Se_3[46, 49]. The bandgap energy change after Fe-doping is not very significant but is expected to partly contribute to the improved activity of Fe-In_2Se_3.

The proposed mechanisms above are needed to further investigate with theoretical calculation models of Fe-In_2Se_3 electronic states. There is an appreciable number of results contradicting the positive effect of iron on water splitting photocatalytic performance in literature; some observed minimal or even negative effects of iron as a dopant[45, 50-52]. However, the nature of Fe-doped In_2Se_3 is still complex and the mechanism of this trapping to recombination transformation is still unclear and under debate[29]. Metal doping effects are strongly dependent on the condition of the doping, including the doping method, the concentration of iron and the iron precursor itself. Considering that different methods may accommodate the iron ions in different positions of the semiconductor, it is hard to compare the 'best' metal cocatalyst between literature. It is concluded that among the screened metal-doped 2D-In_2Se_3 in this research, the Fe-In_2Se_3 synthesised by hydrothermal method showed the highest water splitting activity, and Fe doping successfully enhanced the undecorated 2D-In_2Se_3 by nearly three-fold.

4.3. MoS_2/In_2Se_3 heterojunction

Heterojunction formation will be explored as the second strategy to further enhance the photocatalytic water splitting performance of 2D-In_2Se_3. To reiterate, it is proposed that the heterojunction will form a 2D/2D heterojunction to enhance the photocatalytic activity by charge separation. The concept has already been explained in detail in *1.4.2.2*. A series of heterojunction structures were fabricated with 2D-In_2Se_3 and 2D-MoS_2 by electrostatic self-assembly approach as described in *3.2.4*.

4.3.1. Characterisations of MoS_2/In_2Se_3

Numerous characterisations are done to prove the heterojunction is successfully assembled. As an initial characterisation, XRD was done to confirm the heterojunction assembly process did not cause restacking or recrystallisation of the two respected components. From the XRD

pattern of 1:1 MoS_2/In_2Se_3 in Fig. 4.24, no significant peak was observed that can be attributed to a certain In_2Se_3 or MoS_2 crystalline structure; only background noise could be detected. This proves that the heterojunction structure remains in the 2D structure.

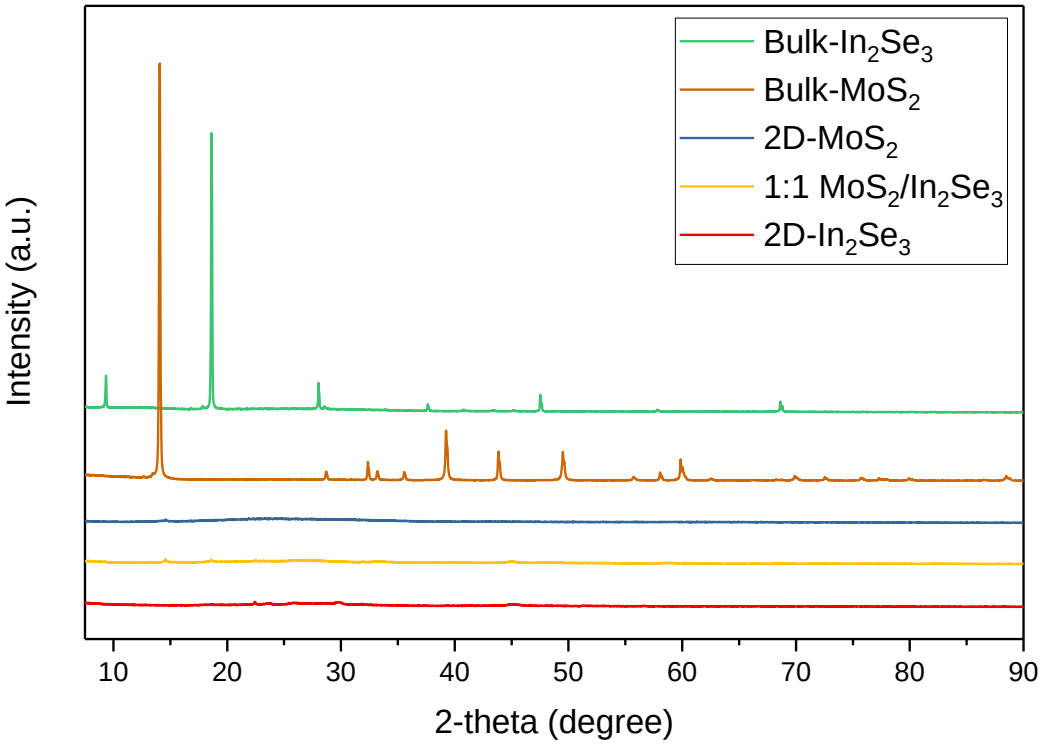

Fig. 4.24. The XRD patterns of 2D-In_2Se_3, Bulk-In_2Se_3, 2D-MoS_2, Bulk-MoS_2, and 1:1 MoS_2/In_2Se_3. The XRD was performed at room temperature with ground powder samples. The XRD measurements were performed and analysed by the author at the Department of Chemistry, University of Oxford.

Zeta potential measurements (Fig. 4.25 and Table 4.5) show that the surface of 2D-In_2Se_3 is positively charged but both 2D-MoS_2 and acidified 2D-MoS_2 are negatively charged in deionised water. All the measured zeta potentials are nearly outside the range of -30 mV to +30 mV, indicating that the colloids are having sufficient repulsive force to attain good stability in solution[53].

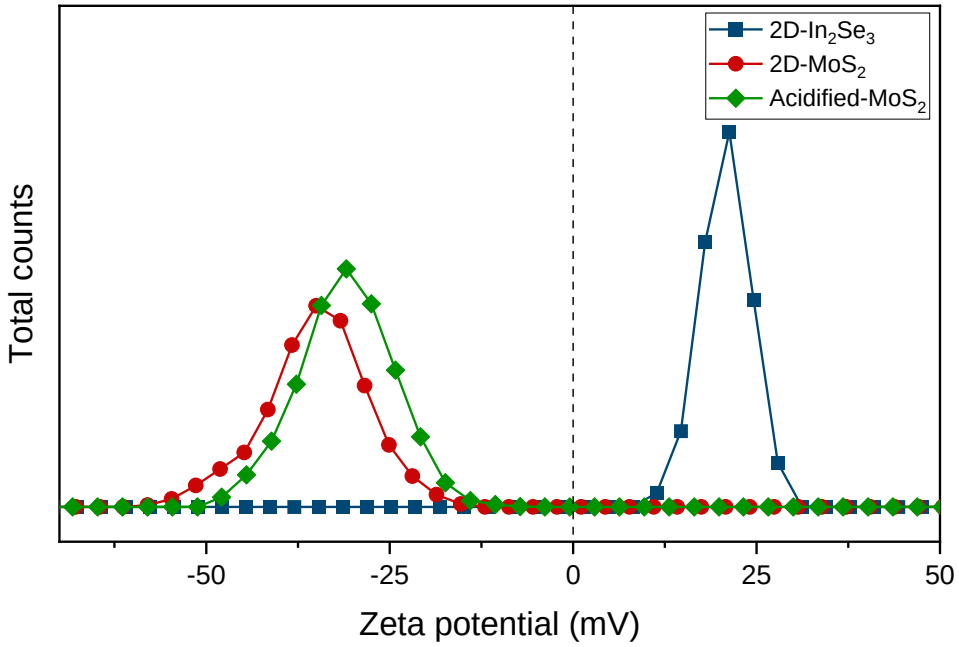

Fig. 4.25. Zeta potential of 2D-In_2Se_3 (blue), 2D-MoS_2 (red) and acidified 2D-In_2Se_3 (green) dispersed in deionised water at pH 7. The zeta potential measurements were performed by Dr Colin Johnston and Dr Kerstin Jurkschat at the Department of Materials, University of Oxford. The data analysis was performed by the author.

Table 4.5. The zeta potentials with their standard deviation of 2D-In_2Se_3, 2D-MoS_2 and acidified 2D-In_2Se_3 dispersed in deionised water at pH 7.

Sample	Zeta potential (mV)
2D-In_2Se_3	+ 27.6 $\pm$ 3.88
2D-MoS_2	- 34.4 $\pm$ 7.79
Acidified 2D-MoS_2	- 35.4 $\pm$ 5.69

2D-MoS_2 is expected to have a negative surface charge. It is reported that the S-rich surface remains stable under 1300 K. At 1300 K, the Mo-rich surface starts to dominate as the high-temperature environment has sufficient energy to remove rows of S atoms[54]. The zeta

potential measurements in this research were done in ambient conditions (room temperature and pressure), therefore, the surface structure remains mostly perfect with S as the surface atoms from the surface of lamellar MoS_2.

Interestingly, acidified MoS_2 has nearly identical zeta potential values compared to 2D-MoS_2. It is expected that protons would attach to the negatively charged surface. However, the change of surface charge is not significant, suggesting that there might only be a limited number of protons attached to the negatively charged S atoms after the acidifying step and do not have a major effect. Possible explanations might be the time, or the acid concentration of the protonation step is not sufficient to protonate the whole 2D-MoS_2 surface, or the protons are easily detached from the surface when acidified 2D-MoS_2 is dispersed into water.

It is also surprising that 2D-In_2Se_3 has a positive zeta potential considering Se on the surface is more electronegative than In in the middle layers. It might be due to cation surface reconstruction in some areas near the (00*l*) surfaces plane – planes of positively charged In atoms are exposed locally while the surface Se atoms are extracted from the surface. Possible surface rearrangements such as hopping events of the entire columns of atoms might be triggered by harsh chemical conditions such as reactions with n-Butyllithium. Further examinations of the nanoparticles by advanced electron microscope (*e.g.* high resolution transmission electron microscopy, HRTEM) are needed to study the positive zeta potential of 2D-In_2Se_3; simulations might also help rationalise the mobility of ions on the surface of 2D-In_2Se_3[55].

Even though the reasons for the 2D-In_2Se_3 surface being positively charged and the protonation step of 2D-MoS_2 did not alter its surface charge remain unclear at this stage, it could be expected that the spontaneous self-assembly of the 2D/2D heterojunction structure. The assembly is due to the electrostatic interaction of the positively charged 2D-In_2Se_3 and

negatively charged acidified 2D-MoS_2. As evidence, TEM was done to prove the successful self-assembled structure.

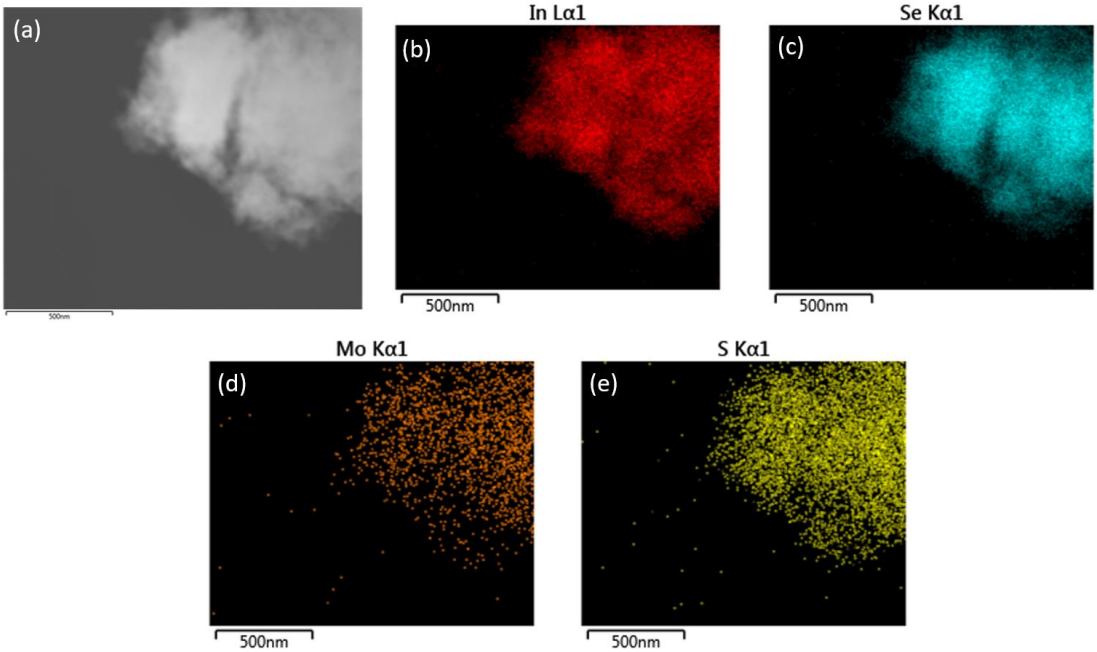

Fig. 4.26. (a) TEM images of a MoS_2/In_2Se_3 flake. (b-e) EDX mapping of In, Se, Mo and S acquired from (a). The TEM imaging and EDX mapping were performed by Mr Ping-Luen (Baron) Ho from Tsang group in the David Cockayne Centre for Electron Microscopy and related facilities at the Department of Materials, University of Oxford. The selection and analysis of the images were performed by the author.

In Fig. 4.26 (a), the TEM image shows the heterojunction structure remains in a layered structure. However, it is not clear whether there are stacked nanosheets composed of two compositions. Hence, elemental mapping is done to identify the composition of the heterojunction structure. In Fig. 4.26 (b-e), In, Se, Mo and S are emerging on the same nanoflake that is shown on the TEM image, implying that the heterojunction structure is successfully formed. The distribution of the atoms is mixed homogeneously. However, the signals for In and Se are more intense than Mo and S. Therefore, it is reasonable to conclude that MoS_2 is sitting on top of In_2Se_3. By convention, the heterojunction structure will be

denoted as MoS_2/In_2Se_3. It is noted that more direct evidence for the heterojunction structure might be drawn from imaging the material from the side. However, this piece of information is yet to be provided due to technical difficulties; more advanced microscopic techniques such as SuperEDX could be used in future analysis.

4.3.2. Photocatalytic performance testing

From the red columns in Fig. 4.27, there is an obvious volcano-like photocatalytic activity trend for the series of MoS_2/In_2Se_3 with different composition ratios. The experimental hydrogen evolution activity of 2D-In_2Se_3 and 2D-MoS_2 is 90.8 μmol h^{-1} g^{-1} and 198.9 μmol h^{-1} g^{-1}. The blue columns in Fig. 4.27 show the weighted average value of the photocatalytic activity of MoS_2/In_2Se_3 heterojunctions. As an example, the weighted average activity of 1:3 MoS_2/In_2Se_3 is calculated as:

$$\frac{198.9\ \mu\text{mol h}^{-1}\text{g}^{-1} \times 1 + 90.8\ \mu\text{mol h}^{-1}\text{g}^{-1} \times 3}{1+3} = 117.8\ \mu\text{mol h}^{-1}\text{g}^{-1}$$

The activity trend does not follow the calculated weight average values. It appears that the activity of the heterojunction structures has a relationship other than the composition ratios of their constituent components. Some interface interactions might be involved in the assembled process, leading to the values diverging from the theoretical values.

Excitingly, only 1:1 MoS_2/In_2Se_3 has a higher photocatalytic activity than the calculated average activity. It might be due to the optimal probability for the two 2D components to well-mix in the dispersion and form the desired heterojunction structures. This shows the 1:1 MoS_2/In_2Se_3 is the experimental optimal ratio for forming the heterojunction interface. Deviations from the optimal ratio might result in a charge imbalance in the material, leading to unstable heterojunctions which further causes the restacking of the two composites. This

could explain the reason of these heterojunction activities are worse than the calculated average values instead of nearly identical.

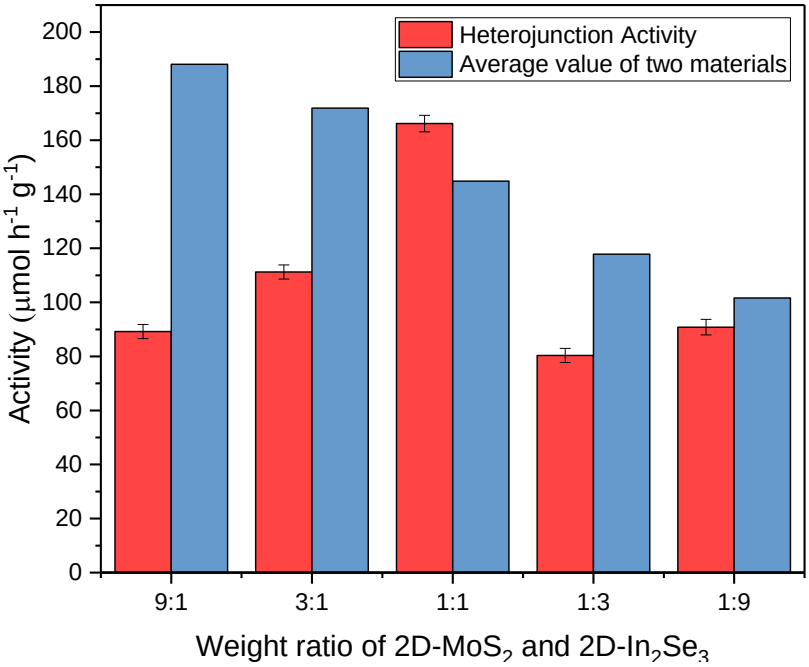

Fig. 4.27. (Red) Photocatalytic water splitting reaction activity tests of MoS_2/In_2Se_3 heterojunction structures with different weight ratios of compositions under 300 W Xenon UV-Vis lamp irradiation at 543 K for 2 hours in Ar. The amount of hydrogen produced was quantified by a GC equipped with a TCD. Error bars indicate the standard deviation of the GC measurements. (Blue) The weighted average activity of the heterojunction structures according to their corresponding 2D-In_2Se_3 and 2D-MoS_2 compositions. The activity tests were performed and analysed by the author.

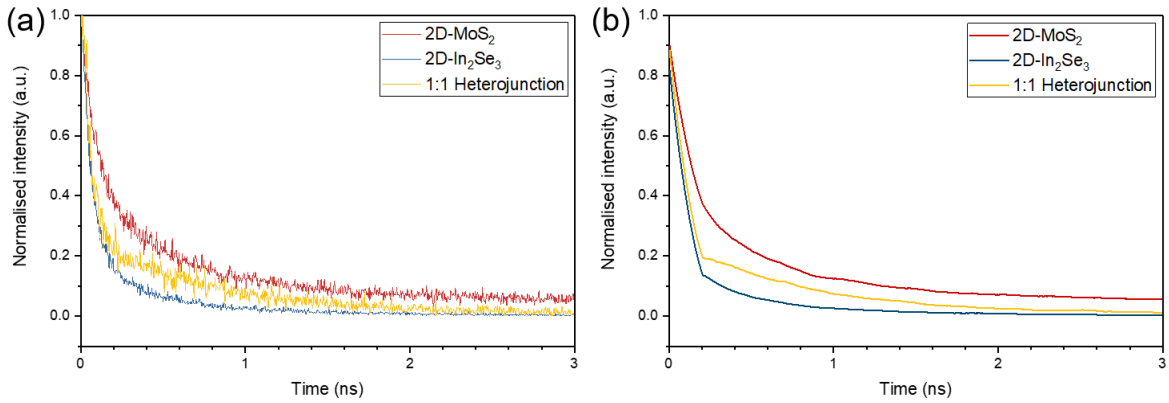

Fig. 4.28. TRPL spectra of 2D-MoS_2 (red), 2D-MoS_2 (blue) and 1:1 heterojunction structure (yellow) measured in air at ambient temperature. (a) corresponds to the raw TRPL measurements and (b) corresponds to the data that is smoothened by the Savitzky-Golay method with 100 points of window. The TRPL measurements were performed by Mr Yiyang Li from Tsang group at Prof Robert A. Taylor's laboratory at the Department of Physics, University of Oxford. The data work-up and analysis were performed by the author.

Table 4.6. The fitting parameters of the two bi-exponential decay functions and mono-exponential decay function for the TRPL of 2D-MoS_2, 2D-In_2Se_3, and 1:1 MoS_2/In_2Se_3. The TRPL fitting was performed by Mr Yiyang Li from Tsang group.

	A_1	**t_1**	**A_2**	**t_2**	**t average**
2D-MoS_2	0.0582	0.855	0.038	0.518	0.759
2D-In_2Se_3	0.0434	0.888	0.0558	0.239	0.721
1:1 MoS_2/In_2Se_3	0.0431	0.809	/	/	0.809

TRPL (Fig. 4.28 (a) and (b)) was employed to investigate the change in exciton lifetimes resulting from the photoexcited charge separation process by employing the MoS_2/In_2Se_3 heterojunction. On Table 4.6, The exciton lifetimes of 2D-MoS_2, 2D-In_2Se_3 and 1:1 MoS_2/In_2Se_3 are 0.759 ns, 0.721 ns and 0.809 ns, respectively. The heterojunction structure

shows a slight enhancement of exciton lifetimes, which might be due to the charge separation by the band alignment of the two 2D composites and this will be further explored below. In turn, the recombination process is suppressed. As a result, the photocatalytic activity of the 1:1 MoS_2/In_2Se_3 is higher than its corresponding weighted average activity. However, the difference between the two values is not significant. This might be attributed to the non-optimised conditions of the heterojunction assembly process. Possible parameters for optimisation include the assembly time, the stirring power and the preparation process of acidified 2D-MoS_2.

To further investigate the interface charge separation behaviour between the heterojunction, the band structure alignment of MoS_2/In_2Se_3 is characterised. To characterise the band structure alignment, the VBM positions of 2D-MoS_2 and 2D-In_2Se_3 are firstly analysed by UPS spectra.

2D-MoS_2:

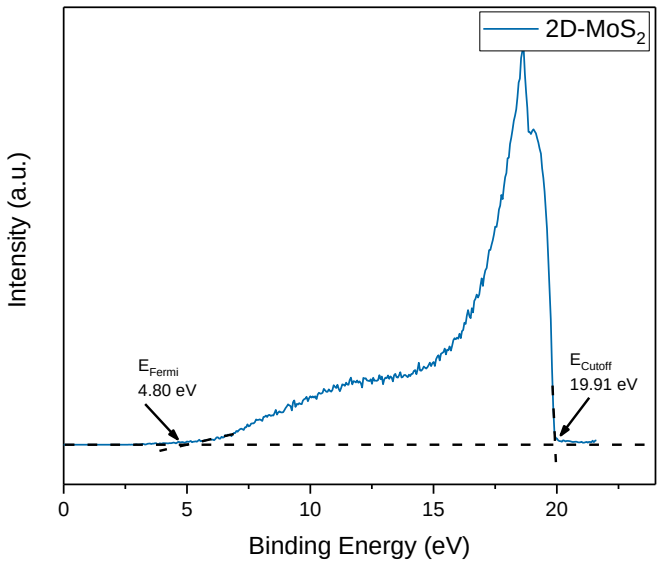

Fig. 4.29. UPS spectrum of 2D-MoS_2. It is used to determine the VBM of 2D-MoS_2. The UPS measurements were performed by Dr Shaoliang Guan from HarwellXPS facilities, United Kingdom. The data work-up and analysis were performed by the author.

UPS was used to determine the ionisation potential, which is equivalent to the valence band energy (*i.e.* VBM). Valence band energy relative to the vacuum, $E_{VB(vacuum)}$ is obtained by Eq. 4.8.

$$-E_{VB(vacuum)} = h\nu + E_{Fermi} - E_{Cutoff} \qquad (4.8)$$

where $h\nu$ = 21.22 eV which is the excitation energy of the He I Source Gun, E_{Fermi} and E_{Cutoff} can be obtained by the linear intersection method from the UPS spectrum (Fig. 4.29) of 2D-MoS_2. The $E_{VB(vacuum)}$ is calculated as follows.

$$E_{VB(vacuum)} = -21.22\ eV - 4.80\ eV + 19.91\ eV = -6.11\ eV$$

Then, valence band energy relative to the NHE potential ($E_{VB(NHE)}$), is obtained by its relationship with $E_{VB(vacuum)}$ by Eq. 4.9. The VBM of 2D-MoS_2 is then calculated as follows.

$$E_{VB(vacuum)} = -E_{VB(NHE)} - 4.44 \qquad (4.9)$$

$$E_{VB(NHE)} = -(-6.11\ eV + 4.44\ eV) = 1.67\ eV$$

2D-In_2Se_3:

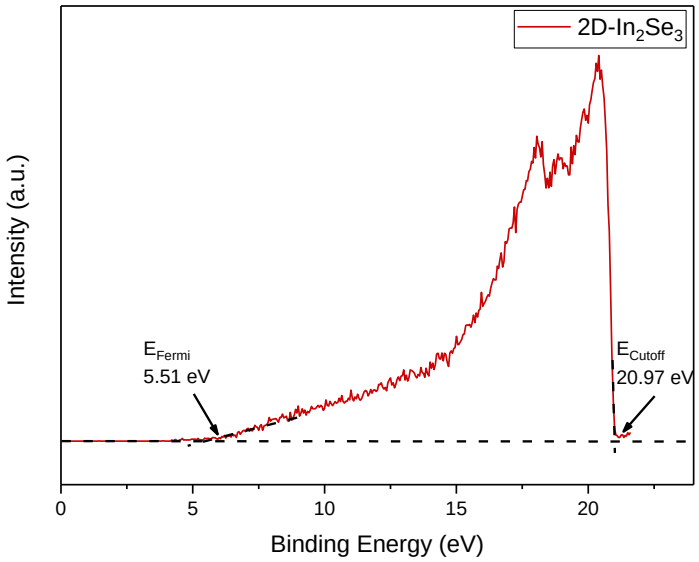

Fig. 4.30. UPS spectrum of 2D-In_2Se_3. It is used to determine the VBM of 2D-In_2Se_3. The UPS measurements were performed by Dr Shaoliang Guan from HarwellXPS facilities, United Kingdom. The data work-up and analysis were performed by the author.

The same calculations are done for 2D-In_2Se_3 as below by Fig. 4.30.

$$E_{VB(vacuum)} = -21.22\ eV - 5.51\ eV + 20.97\ eV = 5.76\ eV$$

$$E_{VB(NHE)} = -(-5.76\ eV + 4.44\ eV) = 1.32\ eV$$

After obtaining the VBM of 2D-MoS_2 and 2D-In_2Se_3, the bandgap energy is scrutinised by the Tauc plot; the bandgap energy for 2D-In_2Se_3 is from Fig. 4.16 (b).

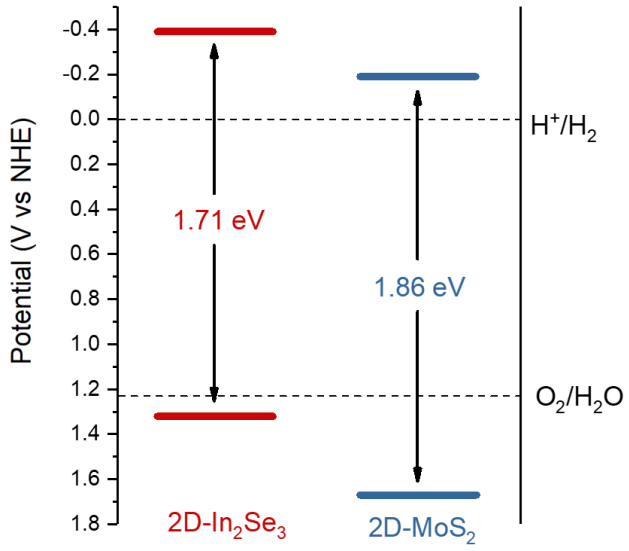

Fig. 4.31. Band structure alignments for 2D-In_2Se_3 and 2D-MoS_2. The bandgap energy of 2D-MoS_2[**] is obtained from Ryon et al[56].

In this band structure alignment, we assumed that the electron transition in 2D-In_2Se_3 is a direct allowed transition. This is supported by the experimental studies by Lyu *et al.* stating that few-layer α-In_2Se_3 (10 nm in thickness which is similar to the 2D-In_2Se_3 of this research) has a direct transition. Furthermore, we assumed that there is little band bending during the contact of the heterojunction interface. From the work of Jiang *et al.*, the conduction band potential of 2D-In_2Se_3 as an n-type semiconductor in the heterojunction interface is only 0.1-0.2 V more negative than its flat band potential; the small gap can be neglected for the sake of simplicity[57]. A similar assumption is made for the 2D-MoS_2, as the p-type semiconductor in this heterojunction structure.

[**] The UV-Vis DRS measurement of 2D-MoS_2 has encountered some technical difficulties; a significant amount of sample is needed for the measurement while the yield for 2D-MoS_2 exfoliation is only around 2%. As a result, there was not enough sample for the UV-Vis DRS measurement. Therefore, the bandgap energy of 2D-MoS_2 is taken from the literature from Ryon *et al.*. In this work, they employed the potassium intercalation method to synthesise quasi-2D MoS_2 from Bulk-MoS_2. They have obtained a direct bandgap of 1.86 eV at the *K* valley by using angle-resolved photo-emission spectroscopy (ARPES). The experimental and the product of this work are very similar to the exfoliation method and 2D-MoS_2 in this research, respectively. Therefore, this bandgap energy of 2D-MoS_2 is reliable for the band structure alignment.

As seen from Fig. 4.31, both CBM of 2D-MoS_2 and 2D-In_2Se_3 are negative enough for efficient H_2 evolution, whereas both the VBM of the two compartments are positive enough to drive the OER theoretically. Moreover, given the staggered band alignment formed between 2D-MoS_2 and 2D-In_2Se_3, the self-assembled type-II heterojunction is expected to cause photocatalytic water splitting[58]. The bandgap 1.71 eV and 1.86 eV correspond to a photon with 725 nm and 667 nm, respectively, which both fall into the visible light region and are included in the solar spectrum emitted by the lamp. Additionally, under the irradiation, electron-hole pairs will be generated in both In_2Se_3 and MoS_2. It is well established that charge carriers tend to transfer to a lower energy state. Hence, in MoS_2/In_2Se_3, the photoexcited electrons in 2D-In_2Se_3 will transfer from its CBM to that of 2D-MoS_2; holes will transfer from the VBM of MoS_2 to that of 2D-In_2Se_3. As a result, the recombination of exciton pairs will be suppressed as photogenerated electrons and holes are in two different materials, leading to a longer exciton lifetime. This is supported by the TPRP measurements. Together, they explain the enhanced photocatalytic activity.

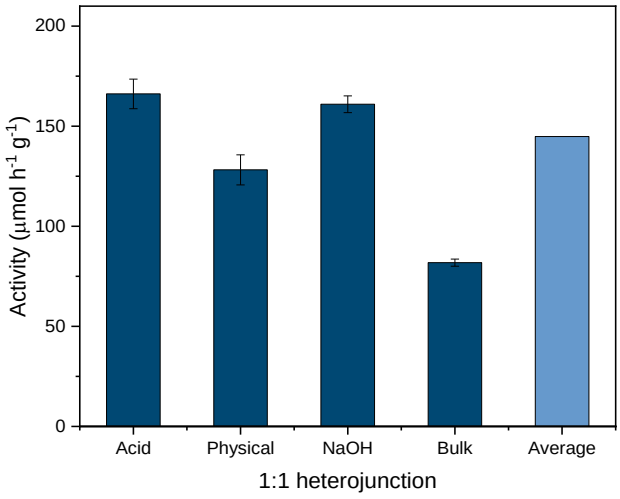

Fig. 4.32. Photocatalytic water splitting reaction activity tests of 1:1 MoS_2/In_2Se_3 heterojunction structure with various methods of MoS_2 pre-treatments (navy) and the calculated weighted average activity of 1:1 MoS_2/In_2Se_3 (light blue). The tests were carried

out under 300 W Xenon UV-Vis lamp irradiation at 543 K for 2 hours in Ar. The amount of hydrogen produced was quantified by a GC equipped with a TCD. Error bars indicate the standard deviation of the GC measurements. The activity tests were performed and analysed by the author.

As discussed, acidifying 2D-MoS_2 is not an effective way of assembling the heterojunction structure. Hence, basified-MoS_2 is synthesised by stirring 2D-MoS_2 with sodium hydroxide (NaOH) to investigate if there is a significant effect on the activity of MoS_2/In_2Se_3. A controlled experiment was done by mixing the required amount of 2D-In_2Se_3 and 2D-MoS_2 physically without any pre-treatment and was reacted in the autoclave under the same photocatalytic conditions, denoted as 'Physical' in Fig. 4.32. As seen from Fig. 4.32, as long as the components are 2D materials (*i.e.* 2D-MoS_2 and 2D-In_2Se_3), the photocatalytic activities of 1:1 MoS_2/In_2Se_3 synthesised by various assemble methods differ slightly; all the activities are all in the same order. No conclusive result can be drawn to conclude which MoS_2 pre-treatment method or assemble method is most promising in assembling the heterojunction structure. It is possible that the acid or alkaline did not alter the surface charge of 2D-MoS_2 under the protonation or deprotonation step, potentially due to the unoptimised reaction conditions or weak bonding between the protons (or hydroxides) and 2D-MoS_2. Therefore, regardless of the pre-treatment of 2D-MoS_2, 2D-MoS_2 have a negative surface charge; self-assembly would happen between the positively charged 2D-In_2Se_3 and negatively charged 2D-MoS_2. The self-assembly can happen even under the activity testing in the autoclave.

Acidified Bulk-MoS_2 and Bulk-In_2Se_3 were also used to form a heterojunction structure (Bulk) and its photocatalytic is also tested under the same photocatalytic conditions as another control experiment. For bulk heterojunction structure shows to have only a half

activity compared to the corresponding 2D materials assembly. The activity difference can be attributed to dipole cancellation which is usually observed in their bulk equivalent materials[59]. It is also a reason for using 2D layered materials as stacking materials to form heterojunction structures.

4.4. References

1. Mohapatra, P. K.; Ranganathan, K.; Dezanashvili, L.; Houben, L.; Ismach, A., Epitaxial growth of In2Se3 on monolayer transition metal dichalcogenide single crystals for high performance photodetectors. *Applied Materials Today* **2020,** *20*, 100734.
2. Küpers, M.; Konze, P. M.; Meledin, A.; Mayer, J.; Englert, U.; Wuttig, M.; Dronskowski, R., Controlled Crystal Growth of Indium Selenide, In2Se3, and the Crystal Structures of α-In2Se3. *Inorganic Chemistry* **2018,** *57* (18), 11775-11781.
3. Ossila, Indium (III) Selenide (In2Se3) Powder and Crystal, https://www.ossila.com/products/indium-iii-selenide, (last assessed on 22 Jun 2021).
4. Joseph, B.; Iadecola, A.; Simonelli, L.; Mizuguchi, Y.; Takano, Y.; Mizokawa, T.; Saini, N. L., A study of the electronic structure of FeSe1 −xTexchalcogenides by Fe and Se K-edge x-ray absorption near edge structure measurements. *Journal of Physics: Condensed Matter* **2010,** *22* (48), 485702.
5. Hummer, A. A.; Rompel, A., Chapter Eight - X-Ray Absorption Spectroscopy: A Tool to Investigate the Local Structure of Metal-Based Anticancer Compounds In Vivo. In *Advances in Protein Chemistry and Structural Biology*, Christov, C. Z., Ed. Academic Press: 2013; Vol. 93, pp 257-305.
6. Vrettos, J. S.; Brudvig, G. W., 8.20 - Oxygen Evolution. In *Comprehensive Coordination Chemistry II*, McCleverty, J. A.; Meyer, T. J., Eds. Pergamon: Oxford, 2003; pp 507-547.
7. Kohary, K.; Burlakov, V. M.; Pettifor, D. G.; Nguyen-Manh, D., Modeling $\mathrm{In}\ensuremath{-}\mathrm{Se}$ amorphous alloys. *Physical Review B* **2005,** *71* (18), 184203.
8. Greenwood, N. N.; Earnshaw, A., *Chemistry of the Elements*. Elsevier: 2012.
9. Marsillac, S.; Combot-Marie, A. M.; Bernède, J. C.; Conan, A., Experimental evidence of the low-temperature formation of γ-In2Se3 thin films obtained by a solid-state reaction. *Thin Solid Films* **1996,** *288* (1), 14-20.
10. Balakrishnan, N.; Steer, E. D.; Smith, E. F.; Kudrynskyi, Z. R.; Kovalyuk, Z. D.; Eaves, L.; Patanè, A.; Beton, P. H., Epitaxial growth of γ -InSe and α , β , and γ -In 2 Se 3 on ε -GaSe. *2D Materials* **2018,** *5* (3), 035026.
11. Lewandowska, R.; Bacewicz, R.; Filipowicz, J.; Paszkowicz, W., Raman scattering in α-In2Se3 crystals. *Materials Research Bulletin* **2001,** *36* (15), 2577-2583.
12. Yang, H.; Pan, L.; Xiao, M.; Fang, J.; Cui, Y.; Wei, Z., Iron-doping induced multiferroic in two-dimensional In2Se3. *Science China Materials* **2020,** *63* (3), 421-428.
13. Setzler, S. D.; Moldovan, M.; Yu, Z.; Myers, T. H.; Giles, N. C.; Halliburton, L. E., Observation of singly ionized selenium vacancies in ZnSe grown by molecular beam epitaxy. *Applied Physics Letters* **1997,** *70* (17), 2274-2276.
14. Kennedy, T. A.; Glaser, E. R.; Murdin, B. N.; Pidgeon, C. R.; Prior, K. A.; Cavenett, B. C., Identification of VSe-impurity pairs in ZnSe:N. *Applied Physics Letters* **1994,** *65* (9), 1112-1114.
15. Wang, J.; Zhang, M.; Meng, J.; Li, Q.; Yang, J., Single- and few-layer BiOI as promising photocatalysts for solar water splitting. *RSC Advances* **2017,** *7* (39), 24446-24452.
16. Ai, M.; Zhang, J.-W.; Wu, Y.-W.; Pan, L.; Shi, C.; Zou, J.-J., Role of Vacancies in Photocatalysis: A Review of Recent Progress. *Chemistry – An Asian Journal* **2020,** *15* (22), 3599-3619.
17. Hou, L.; Guan, Z.; Zhang, M.; He, C.; Li, Q.; Yang, J., Adjusting the ratio of bulk single-electron-trapped oxygen vacancies/surface oxygen vacancies in TiO2 for efficient photocatalytic hydrogen evolution. *Catalysis Science & Technology* **2018,** *8* (11), 2809-2817.
18. Liu, J.; Wei, Z.; Shangguan, W., Defects Engineering in Photocatalytic Water Splitting Materials. *ChemCatChem* **2019,** *11* (24), 6177-6189.
19. Edvinsson, T., Optical quantum confinement and photocatalytic properties in two-, one- and zero-dimensional nanostructures. *Royal Society Open Science* **2018,** *5* (9), 180387.

20. Quereda, J.; Biele, R.; Rubio-Bollinger, G.; Agraït, N.; D'Agosta, R.; Castellanos-Gomez, A., Strong Quantum Confinement Effect in the Optical Properties of Ultrathin α-In2Se3. *Advanced Optical Materials* **2016,** *4* (12), 1939-1943.
21. Procopio, E. F.; Pedrosa, R. N.; L. de Souza, F. A.; Paz, W. S.; Scopel, W. L., Tuning the photocatalytic water-splitting capability of two-dimensional α-In2Se3 by strain-driven band gap engineering. *Physical Chemistry Chemical Physics* **2020,** *22* (6), 3520-3526.
22. Lyu, F.; Sun, Y.; Yang, Q.; Tang, B.; Li, M.; Li, Z.; Sun, M.; Gao, P.; Ye, L.-H.; Chen, Q., Thickness-dependent band gap of α-In2Se3: from electron energy loss spectroscopy to density functional theory calculations. *Nanotechnology* **2020,** *31* (31), 315711.
23. Zhang, X.; Peng, T.; Song, S., Recent advances in dye-sensitized semiconductor systems for photocatalytic hydrogen production. *Journal of Materials Chemistry A* **2016,** *4* (7), 2365-2402.
24. Santos, E.; Hindelang, P.; Quaino, P.; Schulz, E. N.; Soldano, G.; Schmickler, W., Hydrogen electrocatalysis on single crystals and on nanostructured electrodes. *ChemPhysChem* **2011,** *12* (12), 2274.
25. Parsons, R., The rate of electrolytic hydrogen evolution and the heat of adsorption of hydrogen. *Transactions of the Faraday Society* **1958,** *54*, 1053-1063.
26. Dholam, R.; Patel, N.; Adami, M.; Miotello, A., Hydrogen production by photocatalytic water-splitting using Cr- or Fe-doped TiO2 composite thin films photocatalyst. *International Journal of Hydrogen Energy* **2009,** *34* (13), 5337-5346.
27. Zhang, W.; Li, Y.; Zhu, S.; Wang, F., Surface modification of TiO2 film by iron doping using reactive magnetron sputtering. *Chemical Physics Letters* **2003,** *373* (3), 333-337.
28. Zhu, J.; Deng, Z.; Chen, F.; Zhang, J.; Chen, H.; Anpo, M.; Huang, J.; Zhang, L., Hydrothermal doping method for preparation of Cr3+-TiO2 photocatalysts with concentration gradient distribution of Cr3+. *Applied Catalysis B: Environmental* **2006,** *62* (3), 329-335.
29. Wen, L.; Liu, B.; Zhao, X.; Nakata, K.; Murakami, T.; Fujishima, A., Synthesis, Characterization, and Photocatalysis of Fe-Doped : A Combined Experimental and Theoretical Study. *International Journal of Photoenergy* **2012,** *2012*, 368750.
30. Gratzel, M., *Heterogenous photochemical electron transfer*. CRC press: 2018.
31. Popugaeva, D.; Tian, T.; Ray, A. K., Hydrogen production from aqueous triethanolamine solution using Eosin Y-sensitized ZnO photocatalyst doped with platinum. *International Journal of Hydrogen Energy* **2020,** *45* (19), 11097-11107.
32. Escobedo Salas, S.; Serrano Rosales, B.; de Lasa, H., Quantum yield with platinum modified TiO2 photocatalyst for hydrogen production. *Applied Catalysis B: Environmental* **2013,** *140-141*, 523-536.
33. Cox, P. A., *Transition metal oxides: an introduction to their electronic structure and properties*. Oxford university press: 2010; Vol. 27.
34. Choi, W.; Termin, A.; Hoffmann, M. R., The Role of Metal Ion Dopants in Quantum-Sized TiO2: Correlation between Photoreactivity and Charge Carrier Recombination Dynamics. *The Journal of Physical Chemistry* **1994,** *98* (51), 13669-13679.
35. Cong, Y.; Zhang, J.; Chen, F.; Anpo, M.; He, D., Preparation, photocatalytic activity, and mechanism of nano-TiO2 co-doped with nitrogen and iron (III). *The Journal of Physical Chemistry C* **2007,** *111* (28), 10618-10623.
36. Liu, L.; Chen, F.; Yang, F.; Chen, Y.; Crittenden, J., Photocatalytic degradation of 2,4-dichlorophenol using nanoscale Fe/TiO 2. *Chemical Engineering Journal* **2012,** *181-182*, 189-195.
37. Naik, B.; Parida, K., Solar Light Active Photodegradation of Phenol over a Fe x Ti1− x O2− y N y Nanophotocatalyst. *Industrial & engineering chemistry research* **2010,** *49* (18), 8339-8346.
38. Qu, B.; Sun, Y.; Liu, L.; Li, C.; Yu, C.; Zhang, X.; Chen, Y., Ultrasmall Fe2O3 nanoparticles/MoS2 nanosheets composite as high-performance anode material for lithium ion batteries. *Scientific Reports* **2017,** *7* (1), 42772.
39. Dai, L.; Du, X.; Jiang, D.; Chen, W.; Zhu, M.; Wang, K., Ultrafine α-Fe2O3 nanocrystals anchored on N-doped graphene: a nanomaterial with long hole diffusion length and efficient

visible light-excited charge separation for use in photoelectrochemical sensing. *Microchimica Acta* **2017,** *184* (1), 137-145.
40. Wang, F.; Shen, T.; Fu, Z.; Lu, Y.; Chen, C., Enhanced photocatalytic water-splitting performance using Fe-doped hierarchical TiO2ball-flowers. *Nanotechnology* **2017,** *29* (3), 035702.
41. Yen, C.-C.; Wang, D.-Y.; Chang, L.-S.; Shih, H. C., Characterization and photocatalytic activity of Fe- and N-co-deposited TiO2 and first-principles study for electronic structure. *Journal of Solid State Chemistry* **2011,** *184* (8), 2053-2060.
42. Valero-Romero, M. J.; Santaclara, J. G.; Oar-Arteta, L.; van Koppen, L.; Osadchii, D. Y.; Gascon, J.; Kapteijn, F., Photocatalytic properties of TiO2 and Fe-doped TiO2 prepared by metal organic framework-mediated synthesis. *Chemical Engineering Journal* **2019,** *360*, 75-88.
43. McIntyre, N. S.; Zetaruk, D. G., X-ray photoelectron spectroscopic studies of iron oxides. *Analytical Chemistry* **1977,** *49* (11), 1521-1529.
44. Haber, J.; Stoch, J.; Ungier, L., X-ray photoelectron spectra of oxygen in oxides of Co, Ni, Fe and Zn. *Journal of Electron Spectroscopy and Related Phenomena* **1976,** *9* (5), 459-467.
45. Ambrus, Z.; Balázs, N.; Alapi, T.; Wittmann, G.; Sipos, P.; Dombi, A.; Mogyorósi, K., Synthesis, structure and photocatalytic properties of Fe(III)-doped TiO2 prepared from TiCl3. *Applied Catalysis B: Environmental* **2008,** *81* (1), 27-37.
46. Ali, T.; Tripathi, P.; Azam, A.; Raza, W.; Ahmed, A. S.; Ahmed, A.; Muneer, M., Photocatalytic performance of Fe-doped TiO2nanoparticles under visible-light irradiation. *Materials Research Express* **2017,** *4* (1), 015022.
47. Sun, T.; Liu, E.; Fan, J.; Hu, X.; Wu, F.; Hou, W.; Yang, Y.; Kang, L., High photocatalytic activity of hydrogen production from water over Fe doped and Ag deposited anatase TiO2 catalyst synthesized by solvothermal method. *Chemical engineering journal* **2013,** *228*, 896-906.
48. Zhu, J.; Zheng, W.; He, B.; Zhang, J.; Anpo, M., Characterization of Fe–TiO2 photocatalysts synthesized by hydrothermal method and their photocatalytic reactivity for photodegradation of XRG dye diluted in water. *Journal of Molecular Catalysis A: Chemical* **2004,** *216* (1), 35-43.
49. Peng, Y.-H.; Huang, G.-F.; Huang, W.-Q., Visible-light absorption and photocatalytic activity of Cr-doped TiO2 nanocrystal films. *Advanced Powder Technology* **2012,** *23* (1), 8-12.
50. Litter, M. I.; Navío, J. A., Photocatalytic properties of iron-doped titania semiconductors. *Journal of Photochemistry and Photobiology A: Chemistry* **1996,** *98* (3), 171-181.
51. Colmenares, J. C.; Aramendía, M. A.; Marinas, A.; Marinas, J. M.; Urbano, F. J., Synthesis, characterization and photocatalytic activity of different metal-doped titania systems. *Applied Catalysis A: General* **2006,** *306*, 120-127.
52. Piera, E.; Tejedor-Tejedor, M. I.; Zorn, M. E.; Anderson, M. A., Relationship concerning the nature and concentration of Fe(III) species on the surface of TiO2 particles and photocatalytic activity of the catalyst. *Applied Catalysis B: Environmental* **2003,** *46* (4), 671-685.
53. Joseph, E.; Singhvi, G., Chapter 4 - Multifunctional nanocrystals for cancer therapy: a potential nanocarrier. In *Nanomaterials for Drug Delivery and Therapy*, Grumezescu, A. M., Ed. William Andrew Publishing: 2019; pp 91-116.
54. Tiwari, R. K.; Yang, J.; Saeys, M.; Joachim, C., Surface reconstruction of MoS2 to Mo2S3. *Surface Science* **2008,** *602* (15), 2628-2633.
55. Bhatta, U. M.; Ross, I. M.; Sayle, T. X. T.; Sayle, D. C.; Parker, S. C.; Reid, D.; Seal, S.; Kumar, A.; Möbus, G., Cationic Surface Reconstructions on Cerium Oxide Nanocrystals: An Aberration-Corrected HRTEM Study. *ACS Nano* **2012,** *6* (1), 421-430.
56. Ryou, J.; Kim, Y.-S.; Kc, S.; Cho, K., Monolayer MoS2 Bandgap Modulation by Dielectric Environments and Tunable Bandgap Transistors. *Scientific Reports* **2016,** *6* (1), 29184.
57. Jiang, Y.; Wang, Q.; Han, L.; Zhang, X.; Jiang, L.; Wu, Z.; Lai, Y.; Wang, D.; Liu, F., Construction of In2Se3/MoS2 heterojunction as photoanode toward efficient photoelectrochemical water splitting. *Chemical Engineering Journal* **2019,** *358*, 752-758.

58. Fang, H.; Battaglia, C.; Carraro, C.; Nemsak, S.; Ozdol, B.; Kang, J. S.; Bechtel, H. A.; Desai, S. B.; Kronast, F.; Unal, A. A., Strong interlayer coupling in van der Waals heterostructures built from single-layer chalcogenides. *Proceedings of the National Academy of Sciences* **2014,** *111* (17), 6198-6202.
59. Peng, R.; Ma, Y.; Zhang, S.; Huang, B.; Kou, L.; Dai, Y., Self-doped p–n junctions in two-dimensional In2X3 van der Waals materials. *Materials Horizons* **2020,** *7* (2), 504-510.

Chapter 5: Conclusions and future perspectives

5.1. Conclusions

Two-dimensional materials and In_2Se_3 have a promising potential as emerging frontiers in photocatalytic water splitting. This thesis thus demonstrates the photocatalytic activity of 2D-In_2Se_3 and its related decorated forms with the support of state-of-the-art analytical techniques to relate its structure-activity relationship.

2D-In_2Se_3 was successfully exfoliated by the lithium intercalation method and was investigated by comprehensive characterisations. The photocatalytic water splitting activity nearly doubled after the exfoliation. This is attributed to the creation of Se vacancies as supported by EPR and XPS. TRPL also demonstrated 2D-In_2Se_3 has a shorter exciton lifetime compared to its bulk counterpart due to the thinner 2D layer formed. Hence, the photogenerated charge carriers can travel to the surface-active sites in a quicker manner to undergo the surface reactions.

Two other strategies, doping metal cocatalysts and heterojunction formation between 2D-In_2Se_3 and 2D-MoS_2, were used to further enhance the photocatalytic activity of 2D-In_2Se_3. Among the doped metal, 5 wt.% Fe-doping by hydrothermal method showed the highest enhancement in photocatalytic water splitting activity – the activity nearly tripled compared to that of 2D-In_2Se_3. This could be explained by the improved charge separation by the inclusion of Fe^{3+} in the material. The MoS_2/In_2Se_3 heterojunction was successfully constructed by the spontaneous self-assembly approach. The 1:1 MoS_2/In_2Se_3 exhibited an improved activity compared to its calculated value. It is believed that this is due to the formation of a type-II heterojunction as proven by the experimental band structure alignment, leading to prolonged exciton lifetime.

Overall, the first part of the thesis provides the experimental structure-activity evidence of the improved photocatalytic water splitting activity of 2D-In_2Se_3. The second part of the

thesis demonstrated metal doping and heterojunction formation are effective strategies in further enhancing photocatalytic performance. It is hoped that this research would guide the future development of In_2Se_3, as a novel material, and in a broader sense, two-dimensional materials to facilitate the research in discovering promising hydrogen evolution photocatalysts, which could reform the current fossil-based energy society.

5.2. Future perspectives

This thesis has provided some insights into the structural characterisations of 2D-In_2Se_3 and related decorated materials and determined their photocatalytic activities. Future work is needed to optimise the photocatalytic systems of 2D-In_2Se_3 and further understand the structure of the materials.

For 2D-In_2Se_3, the synthesis method can be further optimised including the stirring time with n-butyllithium, the sonication time and the reaction temperature at different stages of the reaction. This might lead to more uniform exfoliation and thinner 2D-In_2Se_3 with a potential to achieve a higher activity. Furthermore, hydrogen evolution rate (μmol g^{-1} h^{-1}) is used in this research to determine the photocatalytic activity. However, this is usually not comparable between photocatalytic systems due to their different reaction conditions. After the system is optimised, QE and STH could be determined to compare its activities between the literature. QE determination should be done by illuminating the photocatalytic system with monochromatic photons at different wavelengths to scrutinise the UV-Vis light harvesting efficiency profile of 2D-In_2Se_3. This could provide further information to understand the optical properties of 2D-In_2Se_3. The formulae of QE and STH can be found in *Appendix*.

A series of Fe-In_2Se_3 with different doping concentrations could be synthesised. Characterisations and activity testing could be done on the series of materials to find out the

role of Fe dopants. Beyond Fe-In_2Se_3, other metal dopants and doping methods (other than hydrothermal and sonochemical methods) are yet to be investigated. For example, different doping methods might accommodate metal ions in a distinctive position in the 2D-In_2Se_3 structure that gives different photocatalytic activities[1]. Sol-gel[2], solvothermal techniques[3] and microwave hydrothermal methods[4] are all possible doping methods that can be further explored. It should be noted that a very wide range of optimum metal content can be found in the literature, for instance, it is 0.05-20 wt.% for iron dopants[5]. Its optimal value might depend on a variety of parameters, such as the synthesis method and conditions, and on the substrate itself.

Future work could also be done to further explore the heterojunction of 2D-In_2Se_3. First, it seemed that the acidification method provided limited assistance in the formation of MoS_2/In_2Se_3 heterojunction structures. The synthetic method could be optimised to improve the quality of heterojunction structure in the future. Furthermore, the charge transfer behaviour in MoS_2/In_2Se_3 heterojunction structure needs to be further investigated. In this research, it is assumed that there is no band bending in the band alignment model. Yet, this is only a rough estimation for the band structure. To further investigate this, the direction of electron transfer between the heterojunction could be investigated by the position of the Fermi energy. This is because when the semiconductors are in contact, band bending will occur until the Fermi energy of the semiconductors reaches a balance. The band bending might lead to a difference in the direction of electron flow due to the space-charge region built at the heterojunction interface. This could be a more direct evidence of whether the photogenerated electron-hole pairs are separated due to the heterojunction formation.

Post reaction analysis could be performed to examine the stability of photocatalysts after the reaction. For example, repeated testing cycles could be carried out to investigate its

photocatalytic stability. The used photocatalysts could also be characterised to understand whether structural change occurs during the reaction. Moreover, a wide variety of materials could be incorporated into the structure of 2D-In_2Se_3 as future work. This research only investigated metal doping and heterojunction formation with MoS_2 for 2D-In_2Se_3 as preliminary strategies for enhancing photocatalytic activities. There are many more strategies for improving a photocatalytic water splitting system apart from the explored methods. Some popular strategies include the decoration of plasmonic metal nanoparticles[6, 7] and the introduction of a local electric field (LEF) by incorporating polar-faceted materials as support[8, 9].

Finally, the charge transfer mechanism and kinetics of water splitting are still a rather complex physical process and they vary between materials, making it difficult to draw unifying conclusions from the reaction. Activity testing coupled with advanced in-situ analytical techniques could be incorporated to investigate the real-time reaction. It is hoped that more fundamental studies, experimental or theoretical, could be carried out to investigate the water splitting process to better understand the whole reaction pathway to overcome the longstanding challenges in the field. For this, novel catalysts are encouraged to be developed continuously in laboratories to investigate their fundamental reaction mechanisms, as well as to bridge the gap between functional lab-scale catalysts and commercial ones in industry.

5.3. References

1. Valero-Romero, M. J.; Santaclara, J. G.; Oar-Arteta, L.; van Koppen, L.; Osadchii, D. Y.; Gascon, J.; Kapteijn, F., Photocatalytic properties of TiO2 and Fe-doped TiO2 prepared by metal organic framework-mediated synthesis. *Chemical Engineering Journal* **2019,** *360*, 75-88.
2. Crișan, M.; Răileanu, M.; Drăgan, N.; Crișan, D.; Ianculescu, A.; Niţoi, I.; Oancea, P.; Şomăcescu, S.; Stănică, N.; Vasile, B., Sol–gel iron-doped TiO2 nanopowders with photocatalytic activity. *Applied Catalysis A: General* **2015,** *504*, 130-142.
3. Sun, T.; Liu, E.; Fan, J.; Hu, X.; Wu, F.; Hou, W.; Yang, Y.; Kang, L., High photocatalytic activity of hydrogen production from water over Fe doped and Ag deposited anatase TiO2 catalyst synthesized by solvothermal method. *Chemical engineering journal* **2013,** *228*, 896-906.
4. Zhao, W.; Li, Y.; Zhang, M.; Chen, J.; Xie, L.; Shi, Q.; Zhu, X., Direct microwave–hydrothermal synthesis of Fe-doped titania with extended visible-light response and enhanced H2-production performance. *Chemical Engineering Journal* **2016,** *283*, 105-113.
5. Ambrus, Z.; Balázs, N.; Alapi, T.; Wittmann, G.; Sipos, P.; Dombi, A.; Mogyorósi, K., Synthesis, structure and photocatalytic properties of Fe(III)-doped TiO2 prepared from TiCl3. *Applied Catalysis B: Environmental* **2008,** *81* (1), 27-37.
6. Abouelela, M. M.; Kawamura, G.; Matsuda, A., A review on plasmonic nanoparticle-semiconductor photocatalysts for water splitting. *Journal of Cleaner Production* **2021,** *294*, 126200.
7. Clavero, C., Plasmon-induced hot-electron generation at nanoparticle/metal-oxide interfaces for photovoltaic and photocatalytic devices. *Nature Photonics* **2014,** *8* (2), 95-103.
8. Noguera, C.; Goniakowski, J., Polarity in Oxide Nano-objects. *Chemical Reviews* **2013,** *113* (6), 4073-4105.
9. Noguera, C., Polar oxide surfaces. *Journal of Physics: Condensed Matter* **2000,** *12* (31), R367-R410.

Appendix

GC Calibration for H_2 and O_2

He and N_2 were used as carrier (reference) gas in the gas chromatography-thermal conductivity detector (GC-TCD) to analyse the amount of oxygen and hydrogen evolved in the activity tests, respectively.

Calibrations of H_2 and O_2 have been done for relating the integrated peak area in GC-TCD measurements and the content of gas.

The calibration curve of H_2 is:

$$\%\, H_2 = Area \times 0.0016$$

The calibration curve of O_2 is:

$$\%\, O_2 = \frac{Area + 7.083}{1954.74}$$

Calculation of H_2 evolution rate

Here, 2D-In_2Se_3 is used as an example to show the calculation of the H_2 evolution rate.

The three measurements obtained from GC-TCD were 11.9, 11.4 and 11.4. The average for the three data is 11.6.

The calibration curve relating the area of the GC-TCD measurement and the percentage of H_2 is:

$$\%\, H_2 = Area \times 0.0016$$

Therefore,

$$\%\, H_2(2D\text{-}In_2Se_3) = 11.6 \times 0.0016 = 0.019\%$$

The autoclave is filled with 6 bars of gas in every activity test. By measuring the volume of the autoclave and by relating the ideal gas law, the moles of gas in the autoclave can be calculated. Then, the atmospheric pressure is substituted into the ideal gas law, the volume of gas (under atmospheric pressure) filled in the autoclave in each test is calculated as 240 cm^3. This is calculated based on the assumption that the moles of the resulted gas (gases produced and the carrier gas) in the reactor is estimated to be the moles of the carrier gas, as this is much larger than the moles of the hydrogen produced in the reaction.

The volume of H_2 in the autoclave can be related by:

$$V = \frac{240\ cm^3 \times \%\ H_2 \times 1L}{1000\ cm^3 \times 100\%}$$

Therefore,

$$V(2D\text{-}In_2Se_3) = \frac{240\ cm^3 \times 0.019\% \times 1L}{1000\ cm^3 \times 100\%} = 4.6 \times 10^{-5}\ L$$

The moles of H_2 produced can be obtained by ideal gas law:

$$pV = nRT$$

$$n(H_2) = \frac{pV}{RT}$$

by taking p = 101.325 kPa; R = 8.314 J K^{-1} mol^{-1} and T = 298 K.

Therefore,

$$n(H_2\ of\ 2D\text{-}In_2Se_3) = \frac{101.325\ \text{kPa} \times 4.6 \times 10^{-5}\ L}{8.314\ \text{J K}^{-1}\text{mol}^{-1} \times 298\ K} = 1.8 \times 10^{-6}\ mol$$

The reaction used 10 mg of 2D-In_2Se_3 as the catalyst and reacted for 2 hours after reaching 543 K. The H_2 evolution rate (μmol h^{-1} g^{-1}) of 2D-In_2Se_3 can be obtained by:

$$H_2\ evolution\ rate = \frac{n(H_2)}{2\ h \times (10 \times 10^{-3})g}$$

Therefore,

$$H_2\ evolution\ rate\ (2D\text{-}In_2Se_3) = \frac{(1.8 \times 10^{-6}) \times 10^6\ \mu mol}{2\ h \times (10 \times 10^{-3})g} = 91\ \mu mol\ h^{-1}g^{-1}$$

Quantum efficiency (QE)

Quantum efficiency is defined according to Eq. A.1.

$$QE\ (\%) = 2 \times \frac{N(H_2)}{N(photons)} \times 100\% \quad \text{(A.1)}$$

where $N(H_2)$ and $N(photons)$ is denoted as the number of hydrogen molecules produced and the number of photons reaching the surface of the reaction solution, respectively. For determining QE, monochromatic light is usually used by passing the light generated to a bandpass filter with central wavelengths. In such a way, the number of incident photons can be calculated by Eq. A.2.

$$N(photons) = \frac{E\lambda}{hc} \quad \text{(A.2)}$$

where E is the energy given from the source of irradiation; λ is the wavelength of the monochromatic light; h is the Plank constant and c is the speed of light[1].

QE measurement was not done in this research as the dependence of QE on the irradiance wavelength is not the focus of the project. Low QE is often due to energy loss related to rapid recombination of photoinduced hole-electron pairs and low mobility of charge carrier to the photocatalyst's surface to undergo the water splitting reaction.

Solar to hydrogen (STH) conversion efficiency

The solar to hydrogen (STH) efficiency is determined according to Eq. A.3.

$$STH(\%) = \frac{E_{H_2}}{E_{solar}} = \frac{r_{H_2} \times \Delta G_{H_2O}}{I \times S} \qquad \text{(A.3)}$$

where E_{H_2} is the energy of generated hydrogen; E_{solar} is the solar energy (energy of the solar simulator lamp) irradiating the reactant solution; r_{H_2} is the hydrogen evolution rate; ΔG_{H_2O} is the Gibbs energy of water splitting (*i.e.* 237 kJ mol^{-1}); I is the light energy flux and S is the irradiation area.

STH is different from QE: STH deals with the efficiency considering the overall power of the irradiation source (including all wavelengths presented in the irradiation spectrum), while QE only considered a specific wavelength in the irradiation source. Therefore, a high QE does not equate to a high STH. A particular photocatalyst can exhibit a nearly 100% QE at a particular wavelength but the STH is usually significantly less. A good example is demonstrated by the work published by Takata *et al.* (2020). The modified aluminium-doped strontium titanate ($SrTiO_3$:Al) photocatalyst has achieved 96% of QE between 350-360 nm, but the STH efficiency under simulated sunlight illumination was only 0.65%[2].

STH in practical devices is often significantly lower than the theoretical maximum conversion efficiency due to the energy losses under operational conditions[3]. In photocatalytic water splitting, the main energy losses for STH mainly come from the limited light concentration and the incapability of absorbing photon energies due to the mismatch of bandgap energy[4].

References

1. Liu, J.; Liu, Y.; Liu, N.; Han, Y.; Zhang, X.; Huang, H.; Lifshitz, Y.; Lee, S.-T.; Zhong, J.; Kang, Z., Metal-free efficient photocatalyst for stable visible water splitting via a two-electron pathway. *Science* **2015,** *347* (6225), 970-974.
2. Takata, T.; Jiang, J.; Sakata, Y.; Nakabayashi, M.; Shibata, N.; Nandal, V.; Seki, K.; Hisatomi, T.; Domen, K., Photocatalytic water splitting with a quantum efficiency of almost unity. *Nature* **2020,** *581* (7809), 411-414.
3. Wijayatha, K. G. U., 5 - Photoelectrochemical cells for hydrogen generation. In *Functional Materials for Sustainable Energy Applications*, Kilner, J. A.; Skinner, S. J.; Irvine, S. J. C.; Edwards, P. P., Eds. Woodhead Publishing: 2012; pp 91-146e.
4. Arunachalam, P.; Al Mayouf, A. M., Chapter 28 - Photoelectrochemical Water Splitting. In *Noble Metal-Metal Oxide Hybrid Nanoparticles*, Mohapatra, S.; Nguyen, T. A.; Nguyen-Tri, P., Eds. Woodhead Publishing: 2019; pp 585-606.